UNIVERSITY OF
Southampton

Faculty of Engineering, Science and Mathematics
School of Physics and Astronomy

# Simulations of ferromagnetic nano-structures

by **Giuliano Bordignon**

Thesis submitted in partial satisfaction
of the requirements for the degree of

DOCTOR OF PHILOSOPHY

Supervisors: Dr. Hans Fangohr, Prof. Peter A.J. de Groot

November 2008

UNIVERSITY OF SOUTHAMPTON

ABSTRACT

FACULTY OF ENGINEERING, SCIENCE AND MATHEMATICS
SCHOOL OF PHYSICS AND ASTRONOMY

Doctor of Philosophy

# Simulations of ferromagnetic nano structures

by Giuliano Bordignon

The magnetic properties of nanometre-scale structures are of fundamental scientific interest and have the potential to play a major role in future data storage technologies. In particular, arrays of small magnetic elements, also called bit-patterned media, are one of the most promising candidates for the future generation of data storage devices.

In this thesis we study potential bit patterned element geometries which are below 1 micrometre in size. Their magnetic behaviour is hard to predict using analytical methods and computer simulations are the principal tool for in-depth analysis. The relevant micromagnetic equations are solved using the combined Finite Element/Boundary Element method, and finite differences.

Patterned media are (quasi) periodic arrangements of identical objects, with each object typically representing one bit. While one or some of these objects can be simulated with today's simulation capabilities, the investigation of arrays with hundreds of objects requires novel simulation methods.

To deal with such large arrays we introduce and evaluate the new "macro geometry" approach. In most real samples this is superior to using conventional periodic boundary conditions as it takes account of the macroscopic shape of the sample.

The micromagnetic simulation package Nmag developed at Southampton has been extended to provide the macro geometry capabilities, and subsequently used to study demagnetising effects between the elements of triangular ring arrays. We find that in a square array of 50-nm size triangular elements these effects are governed by the first and second nearest neighbours and can be considered negligible when the spacing between the rings is larger than 30 nm.

We also study the transport properties via the Anisotropic Magneto Resistance (AMR) signal of connected rings arrays using the multi-physics features of Nmag. The simulations use a self-consistent approach to determine the AMR values, a technique able to explain experimental AMR measurements of real structures. We also show how the spatially varying current distribution affects the computation of the AMR values and found that the uniform current model, sometimes used in the study of AMR effects, is a very inaccurate approximation and can easily lead to qualitatively wrong results.

# Contents

# List of Figures

## Declaration of Authorship

I, Giuliano Bordignon, declare that the thesis entitled "Simulations of ferromagnetic nanostructures" and the work presented in the thesis are both my own, and have been generated by me as the result of my own original research. I confirm that:

- this work was done wholly or mainly while in candidature for a research degree at this University;
- where any part of this thesis has previously been submitted for a degree or any other qualification at this University or any other institution, this has been clearly stated;
- where I have consulted the published work of others, this is always clearly attributed;
- where I have quoted from the work of others, the source is always given. With the exception of such quotations, this thesis is entirely my own work;
- I have acknowledged all main sources of help;
- where the thesis is based on work done by myself jointly with others, I have made clear exactly what was done by others and what I have contributed myself;
- my contribution to the Nmesh algorithm described in Chapter 4 has been limited to the tuning and extension of the first draft of the algorithm written by Dr. Thomas Fishbacher;
- Dr. Hans Fangohr has been the main contributor to the writing of the mesh manual, of which some sections are reported in Appendix B;
- parts of this work have been published as:
  - ▷ G. Bordignon, T. Fischbacher, M. Franchin, A. Knittel, P. A. J. de Groot and H. Fangohr. **A new approach to (quasi) periodic boundary conditions: the macro geometry**. *J. Appl. Phys.*, submitted;
  - ▷ G. Bordignon, T. Fischbacher , M. Franchin, J. P. Zimmermann , P. A. J. de Groot and H. Fangohr. **Numerical studies of demagnetizing effects in triangular ring arrays**. *J. Appl. Phys.* 103, 07D932.1-3, Apr 2008;
  - ▷ G. Bordignon, T. Fischbacher, M. Franchin, J. P. Zimmermann, A. A. Zhukov, V. V. Metlushko, P. A. J. de Groot and H. Fangohr. **Analysis of magnetoresistance in arrays of connected nano-rings**. *IEEE Trans. Magn.*, vol. 43, nr. 6, 2881-2883, Jun 2007;

▷ A. V. Goncharov, A. A. Zhukov, V. V. Metlushko, G. Bordignon, H. Fangohr, C. H. de Groot, J. Unguris, C. Uhlig, G. Karapetrov, B. Ilic and P. A. J. de Groot. **Anisotropy of magnetization reversal and magnetoresistance in square arrays of permalloy nano-rings**. *IEEE Trans. Magn.*, vol. 42, nr. 10, 2948-2950, Oct 2006.

**Signed:** .....

**Date:** .....

## Acknowledgements

First and foremost I would like to acknoweldge the University of Southampton for having given me the privilege to be supervised by great people, who offered me their trust, knowledge and assistance during these PhD studies.

Dr. Hans Fangohr has been an excellent supervisor and I really appreciated his support during all the period of the PhD. He kept up my motivation and enjoyment of conducting this PhD project with his "let's do it!" style, the commitment to high standards of work quality and his sense of humour, and without him the completion of this thesis would have probably required one or two more summers.

A similar acknowledge goes to my other supervisor, Prof. Peter de Groot, for his patience to prepare and present weekly lectures on magnetism, the valuable proof-reading of the various papers, reports and especially this thesis, and for having introduced me to the wonders of magnetism with one of the most memorable lectures I ever attended.

A special thank goes to Dr. Alexander "Sasha" Zhukov for the stimulating discussions about the experimental details of my the research during the first half of the PhD.

Besides them, I would like to thank my office-mates at Building 25, with whom I spent days and nights of my PhD. Richard, Jürgen, Steven, Ignacio, Ernesto, Dario, Jun, Raúl, Thomas, Andreas and especially Matteo have been a wonderful company to work with.

A special acknowledgement must go also to my flatmates Gino, Federico, Tannaze and Anna for having been as close as a second family during these years, and to Yvonne, a purple rose among all those little things that make life beautiful.

I gratefully acknowledge the funding sources that made my PhD work: the School of Physics and Astronomy, the School of Computer Sciences, the Computational Physics Group and Magnetism Group of the Institute of Physics and the American Physical Society.

Above all I would like to thank my family, without whom I wouldn't be here today.

# Nomenclature

| | |
|---|---|
| $\alpha$ | Phenomenological damping parameter, see Eq. (2.64) |
| $\alpha_{a,b,c}$ | Directional cosine of the magnetisation-to-axis angle, see Eq. (2.28) |
| $\alpha_{i,j}$ | Angle between the magnetisation moments $\mathbf{m}_i$ and $\mathbf{m}_j$ |
| $\bar{F}$ | Volume contribution to the force vector of the matrix equation for the solution of the scalar potential associated to the demagnetising field in the Finite Element Method, see Eq. (3.46) |
| $\chi$ | Susceptibility |
| $\gamma_w$ | Energy per unit area of a Bloch wall, see Eq. (2.53) |
| $\gamma$ | Gyromagnetic ratio, see Eq. (2.64) |
| $\lambda_{\text{ex}}$ | Exchange length, see Eq. (2.52) |
| $\mathcal{E}_{\text{cub}}$ | Cubic anisotropy energy density |
| $\mathcal{E}_{\text{dem}}$ | Demagnetising energy density |
| $\mathcal{E}_{\text{exch}}$ | Exchange energy density |
| $\mathcal{E}_{\text{uni}}$ | Uniaxial anisotropy energy density |
| $\mathcal{E}_{\text{Zee}}$ | Zeeman energy density |
| $\mu_0$ | Permeability of free space |
| $\mu_{\text{B}}$ | Bohr magneton |
| $\nabla$ | Derivative operator |
| $\nabla\cdot$ | Divergence operator |
| $\nabla^2$ | Laplacian operator |

$\Omega^e$ Domain of the element $e$ in the solution of a Partial Derivative Equation using the Finite Element Method, see Eq. (3.20)

$\rho$ Resistivity, see Eq. (7.2)

$\rho_0$ Resistivity of a material at zero applied field, see Eq. (7.2)

$\mathbf{E}$ Electric field, see Eq. (7.4)

$\mathbf{H}_{\text{ext}}$ External magnetic field

$\mathbf{J}$ Atomic total angular momentum

$\mathbf{J}$ Current density, see Eq. (7.4)

$\mathbf{K}$ Stiffness matrix used for the solution of the scalar potential associated to the demagnetising field in the Finite Element Method, see Eq. (3.46)

$\mathbf{L}$ Atomic orbital angular momentum

$\mathbf{M}$ Magnetisation vector, total atomic moment per unit volume

$\mathbf{m}$ Magnetic moment

$\mathbf{m}_\xi^e$ Magnetisation in the node $\xi$ of the element $e$ using the Finite Element Method, see Eq. (3.33)

$\mathbf{N}$ Demagnetising tensor

$\mathbf{r}_{j,i}$ Lattice vector $|\mathbf{r}_j - \mathbf{r}_i|$

$\mathbf{S}$ Atomic spin angular momentum

$\mathbf{s}$ Atomic spin

$\mathbf{u}_i$ Direction of the magnetisation moment $\mathbf{m}_i$, see Eq. (2.37)

$\sigma$ Magnetic charges density, see Eq. (2.17)

$\tau$ Expected time of a magnetisation reversal in a magnetic grain due to thermal effect, see Eq. (2.67)

$\tau_0$ Inverse of attempt frequency, see Eq. (2.67)

$\theta$ Direction of the magnetisation with respect to the easy axis in the Stoner-Wohlfarth model, see Eq. (2.57)

$\theta_{\mathrm{h}}$ Direction of the applied field with respect to the easy axis in the Stoner-Wohlfarth model, see Eq. (2.57)

$\varphi$ Angle on the plane orthogonal to the axis of a Bloch wall, see Eq. (2.53)

$\widetilde{F}$ Surface contribution to the force vector of the matrix equation for the solution of the scalar potential associated to the demagnetising field in the Finite Element Method, see Eq. (3.46)

$B$ Boundary Element Matrix, see Eq. (3.93)

$E_{\mathrm{b}}$ Thermal energy barrier

$E_{\mathrm{exch}}$ Exchange energy

$E_{\mathrm{cub}}$ Cubic anisotropy energy

$E_{\mathrm{dem}}$ Demagnetising energy

$E_{\mathrm{exch}}$ Exchange energy

$E_{\mathrm{sha}}$ Shape anisotropy energy

$E_{\mathrm{uni}}$ Uniaxial anisotropy energy

$f^e(\mathbf{r})$ Trial solution of a Partial Derivative Equation using the Finite Element Method, see Eq. (3.20)

$F_{\mathrm{L\text{-}J}}$ Lennard-Jones potential used to relax the nodes of a mesh, see Eq. (4.5)

$F_{\mathrm{lin}}$ Linear force used to relax the nodes of a mesh, see Eq. (4.5)

$g_J$ Generalised Landé factor

$H_{\mathrm{c}}$ Coercive field

$H_{\mathrm{eff}}$ Effective magnetic field

$I_{\mathrm{e}}$ Exchange integral of atomic wave functions

$k^e_{i,j}$ Entry of the stiffness matrix associated to the integral over the element $e$ of the derivatives of the local coordinates $L^e_i$ and $L^e_j$, see Eq. (3.45)

$K_{\mathrm{m}}$ Stray field energy constant, see Eq. (2.51)

$L_i$ $i$-th component of the local coordinate system used in the Finite Element Method, see Eq. (3.7)

$M_{\mathrm{r}}$ Remanent magnetisation

$M_{\mathrm{s}}$ Saturation magnetisation

$N_{\mathrm{x,y,z}}$ Demagnetising factors, see Eq. (2.31)

$p_i$ coefficients of the polynomial used to express the approximated global solution of a Partial Derivative Equation using the Finite Element Method over an element of the mesh, see Eq. (3.3)

$R(L_\xi^e)$ Residual at the node $\xi$ of the element $e$ used in the Galerkin method, see Eq. (3.22)

$r$ Distance between two neighbour nodes of a mesh, (also called rod lenght), see Eq. (4.1)

$r_0$ Ideal rod length in the midpoint between two neighbour nodes of a mesh, see Eq. (4.3)

$r_{\mathrm{AMR}}$ Anisotropic Magneto-Resistance ratio, see Eq. (7.9)

$U(\mathbf{r})$ Global solution of a Partial Derivative Equation using the Finite Element Method, see Eq. (3.2)

$u^e(\mathbf{r})$ Approximation of the global solution of a Partial Derivative Equation using the Finite Element Method over an element $e$ of the mesh, see Eq. (3.2)

$u_\xi^e$ Value of the approximated global solution of a Partial Derivative Equation using the Finite Element Method on the node $\xi$ of an element $e$ of the mesh, see Eq. (3.5)

$U_1(\mathbf{r})$ Solution of the scalar potential associated to the demagnetising field internal to the magnetic objects using the Boundary Element Method, see Eq. (3.88)

$U_2(\mathbf{r})$ Solution of the scalar potential associated to the demagnetising field external to the magnetic objects using the Boundary Element Method, see Eq. (3.88)

$U_{\mathrm{dem}}$ Scalar magnetic potential associated to the demagnetising field

$U_{\mathrm{dem}}^i$ Scalar magnetic potential associated to the demagnetising field inside a magnetic body

$U_{\mathrm{dem}}^o$ Scalar magnetic potential associated to the demagnetising field outside a magnetic body

$w$ Normalised distance between two neighbour nodes of a mesh, see Eq. (4.1)

| | |
|---|---|
| $w_{\mathrm{B}}$ | Domain wall width of a Bloch wall, see Eq. (2.55) |
| $w_{\mathrm{N}}$ | Domain wall width of a Néel wall, see Eq. (2.56) |
| $z$ | Cell site number; $z = 1$, 2 or 4 for simple cubic, body-centred cubic and face-centred cubic, respectively; see Eq. (2.48) |
| A | Exchange stiffness constant, see Eq. (2.47) |
| a | Edge length of cristallographic unit cell, see Eq. (2.44) |
| K | Anisotropy energy factor, see Eq. (2.29) and (2.30) |

# Chapter 1

# Introduction

Magnetic materials are at the base of many activities in everyday life. They can be found in radio speakers, credit cards, electric engines or sensors, and the development in recent years of manufacturing, experimental and computational techniques able to design and study magnetic materials at sub-micron length scale have been crucial for a technology at the base of the information society: data storage devices.

The vast majority of magnetic data storage devices are represented by hard disk drives where a bit of information is physically represented by the average magnetisation of a few tenths of magnetic grain arranged in a so called bit cell. As the density of information is the critical parameter in data storage devices, the approach used so far to increase the number of bits per square inch has been to reduce the number as well the size of the grain in each bit cell.

However at the current pace such downscaling trend will soon reach a point where the thermal energy of the environment is sufficient to spontaneously re-orient the magnetisation in the grains. Since the information is stored using the direction of the magnetisation, the consequence is the random cancellation of the stored information.

This point of thermal activation is called the superparamagnetic limit (SPL) and the associated energy barrier, which prevents the random switching of the magnetisation, is proportional to the size of the magnetic particle. In current media, where a bit of information is spread over several magnetic grains, such barrier is related to the size of the grains, and a further reduction of their size without incurring in the SPL problem represents a major challenge for hard drives manufacturers.

A solution is to shift the SPL problem from the size of the grains to the physical size of the bits, with new designs being an active research field both in academia and in industry.

One of the most promising designs for this goal are bit-patterned media. Patterned media are made of regular arrays of magnetic element where each element stores a bit of information. Such elements are manufactured to be virtually grain-free (so that the

SPL applies to the volume of the entire element), and by acting on their geometry new magnetic properties can be exploited or induced in the material.

Possible applications of patterned media are Hard Disk Drives (HDDs) and Magnetic Random Access Memories (MRAMs). In HDDs the use of nanostructured media is motivated by the large recording density achievable with such technology, while in MRAMs the main advantage is in the non-volatile retention of data. At present these applications differ on the way data are read and written on the medium, through magnetic fields in the HDD case and by electric currents in MRAMs, but the development of a common technology for both storage and random access memories would bring a number of advantages in the computer market (faster read/write, lack of mechanical parts, lower energy consumption, single memory for different needs).

As the best design is still an open issue for real patterned media, this thesis presents the magnetic characteristics for some promising candidates of patterned elements. The analysed elements are characterised by magnetic structures with size of the order of few hundreds of nanometres and show switching processes with a time scale of few picoseconds. Measurements at these space and time scales are very difficult [1] but micromagnetic simulations can reproduce with high accuracy the dynamics of the processes and the computational approach allows high flexibility on the design of the elements and the tune of their parameters.

For these reasons the quantitative analysis presented in this thesis is mainly done using numerical methods. Where possible the results are compared to experimental measures of magnetisation and transport properties on real samples. These samples are patterned at micron and sub-micron length scales, and the differences between experiments and simulations are discussed in terms of the possible approximations made in the numerical models.

The outline of the thesis is as follows: Chapter 2 gives a brief introduction to the properties of magnetic materials and ferromagnets in particular. Their magnetic behaviour is described in the context of the micromagnetic theory and a large part of the chapter is dedicated to the definition of the energies involved. This chapter gives also an overview of current recording media, and shows how their limitations can be overcome with the use of patterned media. Chapter 3 introduces the computational approach we used to investigate promising elements for patterned media. After the description of the micromagnetic modelling in its variants (finite differences, finite elements, boundary element) the focus is narrowed towards the Finite Element Method/Boundary Element Method (FEM/BEM). This is the basis of the main software used in the simulations, Nmag [2], a micromagnetic package developed at University of Southampton where my main contribution has been in the development of the mesh module.

Chapter 4 presents the features of this module, while Chapter 5 is dedicated to one of the exclusive features of Nmag: the macro geometry concept. The following chapter shows its application to the study of arrays of triangular ring elements, while Chapter 7 highlights another unique feature of Nmag: the possibility to do multi-physics simulations of micromagnetic systems, and the analysis of transport properties of a connected ring array is presented.

# Chapter 2

# Micromagnetics

## 2.1 Discovery of magnetism

The discovery of magnetism dates back to ancient Greece, where, according to Pliny [3], special stones able to attract pieces of iron were discovered by a shepherd called Magnés on the slopes of Mount Ida. Besides the attractive property, the stones were remarkable for two other characteristics: 1) depending on the relative orientation, two stones attracted or repelled each other when placed nearby and 2) they aligned along the North-South axis of the Earth when freely suspended.

Over the centuries this unique behaviour brought the stones, today known as lodestones, to find applications in medicine, for medical and psychological treatments [4], and in navigation, where their use as mariner's compass is believed to be invented by Chinese and introduced in Europe by 1200 AD [5].

To put some light on their attractive properties an accurate investigation was carried out by Gilbert in the late 1500, which led to the publication in 1600 of his famous treatise 'De Magnete'. In the book, regarded as the first treatise on the science of electricity and magnetism, Gilbert pointed out two revolutionary ideas: 1) the alignment of magnetic stones with the North-South axis of the Earth is due to the magnetic properties of the Earth itself, which can be viewed as a giant magnet; 2) there are other attractive properties of matter which are non-magnetic in origin: this is the case of amber, whose attractive properties were named "electric", *i.e.* "from amber".

What Gilbert tried to separate was brought back together at the beginning of the 19th century by the studies on the voltaic cell and the discovery of Hans Christian Ørsted in 1820. During one of his experiments, he noted that an electric current flowing in a wire caused the deflection of a magnetic needle placed nearby. That was sufficient to start a series of experiments in the scientific community which led to the first mathematical treatment of the electromagnetic phenomena by André-Marie Ampère in the same year

and the discovery of the electromagnetic induction by Joseph Henry and Michael Faraday in 1830. These discoveries confirmed that magnetic and electric fields are two aspects of the same entity, the electromagnetic field, and its properties started to be exploited in the telegraph and for the construction of motors and dynamos; at the same time, however, permanent magnetic materials were still an unexplained phenomenon of nature and their description was mainly experimental rather than theoretical.

Following the path opened by Ampère the complete theory linking magnetism and electricity was completed by 1873 with Maxwell's equations, but it took until 1907 and the ideas of Pierre Weiss to explain the origins of magnetism in permanent magnets. He postulated that the atoms in these materials had a permanent magnetic moment, and the moments associated to neighbour atoms tended to behave cooperatively over microscopic regions, leading to the formation of so called domains. He justified this behaviour with the presence of a molecular field, a correct though not very convincing hyphotesis at the time of Rutherford and Bohr atomic models [4].

New arguments in support of the molecular field theory came in the late 1920s with the development of quantum mechanics. This new theory postulated that the atom's constitutive elements, protons, neutrons and electrons, bring an intrinsic magnetic moment, the so called spin. The new spin properties, verified in 1923 by the famous experiment of Otto Stern and Walther Gerlach, brought a wealth of theoretical developments concerning the microscopic structure of matter, and one of the most important results was that protons, neutrons and electrons can be described as having half-integer values of spin, thus obeying to the so called Fermi-Dirac statistics.

The consequence of this result is that two electrons cannot have the same set of quantum numbers within the same system, the so called Pauli exclusion principle, and Dirac showed that such condition implies the presence of a spin-spin interaction between localised electrons of neighbour atoms, an effective force comparable to that postulated by Weiss in his molecular field theory. The final confirmation to Weiss' theory came in 1932 with the observation of magnetic domains by Bitter [6] (see Figure 2.1) and as a late recognition to his work, Weiss' concept of mean field approximation is at the base of today's numerical models of magnetic materials at sub-micron length scale.

## 2.2 Atomic moments

Quantum mechanics has been extensively tested in the last 70 years and today we know that magnetic properties in matter are due to atomic dipoles whose origin is in the spin and angular momenta of the atoms. Calling $\mathbf{S}$ the spin contribution and $\mathbf{L}$ the orbital contribution to the total angular momentum $\mathbf{J} = \mathbf{L} + \mathbf{S}$ of an atom, the expression of the

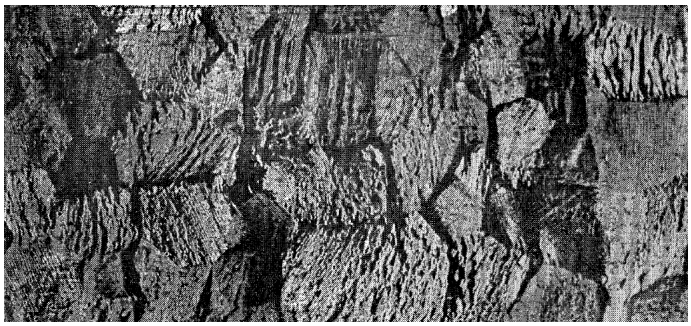

Figure 2.1: Bitter technique of magnetic powder used to show domain boundaries (reproduction from [6]).

atomic magnetic dipole is given by

$$\mathbf{m} = -g_J \, \mu_{\mathrm{B}} \, \mathbf{J} \tag{2.1}$$

In this expression $\mu_B$ is the Bohr magneton and $g_J$ the so called spectroscopic splitting factor, or Landé factor. The Bohr magneton can be interpreted as the spin magnetic moment of a free electron and is expressed as

$$\mu_{\mathrm{B}} = \frac{e\hbar}{2m_e} \tag{2.2}$$

with $e$ the electron charge, $m_e$ its mass and $\hbar$ the Planck's constant, while the Landé factor is an index of the proportion between the spin and orbital contributions to the total magnetic moment

$$g_J = 1 + \frac{J(J+1) + S(S+1) - L(L+1)}{2J(J+1)} \tag{2.3}$$

Magnetic moments of nuclei are typically much smaller than the magnetic moment of the electron [7], and their contributions to the **J** factor in Eq. (2.1) can be usually neglected. Therefore the only significant contribution to **J** comes from electrons magnetic moment and for most 3d transition metals, including cobalt, iron and nickel, the orbital component of this contribution is negligible. The reason of the minor contribution from the orbital component is two-fold: 1) the presence of a crystal field, an inhomogeneous electric field created by neighbouring atoms which is large enough to quench the orbital component of the angular momentum; 2) the small contribution of the spin-orbit coupling to the energy of the system, which introduces a negligible contribution to the orbital component of the total magnetic moment despite the large contribution of the spin component.

Hence atomic magnetism comes almost exclusively from the spin of electrons, and the magnetic properties of different elements depend on the way spins sum up in the atomic shells.

The shells, sub-shells and orbitals are filled according to the 'Aufbau' principle: the lowest energy orbitals are filled first and, as a consequence of the Pauli exclusion principle, each orbital may contain at most two electrons of opposite spin. Orbitals with the same energy are occupied according to Hund's first and second rules [7]:

- maximise the value of the total spin S allowed by the exclusion principle;
- maximise the value of the orbital angular momentum L consistent with this value of S

When the shells are completely filled, there is no contribution from the electrons in those shells to the magnetic moment of the atom, while when the shell are partially filled, the only contribution comes from the spins of unpaired electrons. Strong magnetic properties are associated to atoms with many unpaired electrons in the orbitals responsible for magnetism, which are the 3d orbitals for the elements of the transition metals and the 4f orbitals for the elements of the rare earths.

## 2.3 Types of magnetism

Based on the type of interaction between the atomic moments and with an external field, magnetic elements can be mostly classified in three main categories [8]: diamagnetic, paramagnetic and ferromagnetic.

Diamagnetism is a form of magnetism induced in any material by the presence of an external field. In an atom the reaction to such a field is a change in the electrons orbital motion, which creates a magnetic field opposing the external one. As the orbital contribution to the total magnetism is very minor, the effect of diamagnetism on the atomic moments is very weak and diamagnetism is easily overcome by the other two forms of magnetism.

The second form of magnetism is paramagnetism. This is the case of strong atomic moments which are weakly coupled. Without an external applied field the atomic moments are randomly oriented, thus averaging their magnetisation to zero, but in presence of an applied field they tend to align along the field direction, resulting in a magnetisation of the material. The consequence is that, contrarily to the diamagnetic case, a paramagnetic material experiences a weak attraction when placed in an external field, and most magnetic materials exhibit this type of magnetism [9].

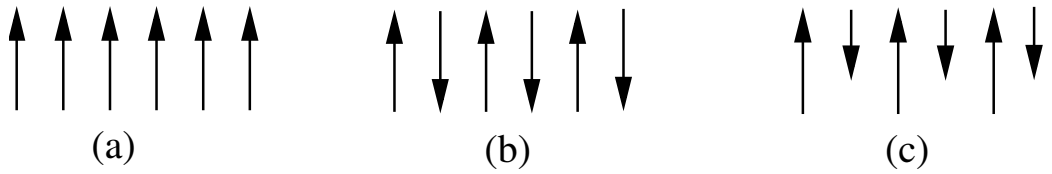


Figure 2.2: Possible configurations in materials with magnetic ordering: (a) ferromagnetism, (b) antiferromagnetism and (c) ferrimagnetism (from [7]).

The third form of magnetism occurs in some paramagnetic materials when they are brought below a characteristic temperature $T_c$. At this temperature, called Curie temperature, these materials experience a transition from a disordered to an ordered state characterised by an alignment of neighbour magnetic moments, a state retained also in the absence of an applied field.

Depending on the type of alignment and the structure of the crystal lattice, there are three possible ordering configurations, as shown in Figure 2.2: we have a ferromagnet if neighbour atomic moments are parallel aligned, an antiferromagnet when neighbour moments are aligned in some sort of anti-parallel pairing, and a ferrimagnet when the material presents two different sub-lattices with different net moments, which are anti-parallel aligned.

For their weak magnetic properties, diamagnetic, paramagnetic, antiferromagnetic and ferrimagnetic materials are often considered non magnetic, while ferromagnetic materials are the most used as permanent or temporary magnets.

## 2.4 Characteristic energies

As we have seen in Sec. 2.2, the theory of ferromagnetism in its atomistic formulation assumes that every atom is a magnetic dipole. When placed in a magnetic field, a dipole aligns with the field in order to reach a configuration of minimal energy, a principle valid also in multi-atom systems, although short and long range interactions must be taken into account. These interactions, characteristic of magnetic systems, are associated to four energies: Zeeman energy, exchange energy, demagnetising energy and anisotropy energy.

### 2.4.1 Zeeman energy

The Zeeman energy is introduced in a magnetic system whenever an external field is applied to the sample. Calling $\mu_0$ the permeability of free space, the form of this energy

is that of the classical energy of a magnetic moment $\mathbf{m}$ in an external field $\mathbf{H}_{\text{ext}}$

$$\mathcal{E}_{\text{Zee}} = -\mu_0 \mathbf{H}_{\text{ext}} \cdot \mathbf{m} \tag{2.4}$$

and its effect is to align the magnetisation in the sample along the direction of the applied field.

### 2.4.2 Exchange energy

As introduced in Sec. 2.3, ferromagnets are characterised by an ordered state of the atomic spins, a configuration that Weiss could explain only with the presence of an internal field (molecular field) strong enough to overcome the randomising effect of the temperature. In Sec. 2.1 we have also seen that a similar field was justified by Dirac on the basis of the Pauli exclusion principle. Dirac showed that such field was due to quantum effects related to overlapping wave functions of neighbour atoms, and he modelled this interaction as an exchange energy of the form

$$\mathcal{E}_{\text{exch}} = -I_{\text{e}}\, \mathbf{s}_1 \cdot \mathbf{s}_2 \tag{2.5}$$

where $\mathbf{s}_1$ and $\mathbf{s}_2$ are atomic spins and $I_{\text{e}}$ is the exchange integral of the atomic wave functions. Using the approximation $\mathbf{m}_i = -g\,\mu_{\text{B}}\,\mathbf{s}_i$ obtained from Eq. 2.1 considering only the spin contribution to the total magnetic moment, and assuming that all the atoms have the same atomic moment $\mathbf{m}$, the exchange energy for a system of $N$ atoms can be written as

$$E_{\text{exch}} = -\sum_{i=1}^{N} \sum_{j=1|_{j\neq i}}^{N} J_{i,j}\, \mathbf{m}_i \cdot \mathbf{m}_j \tag{2.6}$$

where $\mathbf{m}_i$ and $\mathbf{m}_j$ are the magnetic moments on the lattice sites and the variable $J_{i,j}$, which depends on the atoms $i$ and $j$, is defined as $J_{i,j} = I_{\text{e}_{i,j}}/g^2\mu_{\text{B}}^2$.

With the assumption of an homogeneous material, that is with a constant $J_{i,j} = J$ throughout the solid, Eq. (2.6) can be rewritten as

$$E_{\text{exch}} = -\sum_{i=1}^{N} J\, m_i \sum_{j=1|_{j\neq i}}^{N} m_j \cos\alpha_{i,j} \tag{2.7}$$

where $m_i$ and $m_j$ are the magnitudes of the magnetic moments $\mathbf{m}_i$ and $\mathbf{m}_j$ and $\alpha_{i,j}$ is the angle between their directions.

The exponential decay of the integral $I_{\text{e}}$ allows to restrict the sum over $j$ in Eq. (2.6) and (2.7) to the nearest neighbours of each atom $i$ and the sign of $J$ is responsible for the

parallel alignment of the atomic moments in the case of ferromagnets (where $J > 0$) and the anti-parallel alignment in the case of antiferromagnets (where $J < 0$).

Rewriting the sum over $j$ in Eq. (2.7) using only the contribution of the $z$ nearest neighbours we have

$$E_{\text{exch}} = -\sum_{i=1}^{N} J\, m_i \sum_{j=1}^{z} m_j \tag{2.8}$$

where the cosine of the angles $\alpha_{i,j}$ is assumed to be 1 for all the angles $\alpha_{i,j}$, a configuration equivalent to a perfect alignment of neighbour moments. Comparing Eq. (2.8) to the energy of a system of $N$ magnetic moments in an effective field $H_{\text{eff}}$ we obtain

$$H_{\text{eff}} = \frac{J}{\mu_0} \sum_{j=1}^{z} m_j \tag{2.9}$$

If now we define the magnetisation $\mathbf{M}$ as the total atomic moment per unit volume and $N_v$ the number of atomic moments per unit volume, we can write

$$M = N_v m \tag{2.10}$$

and Eq. (2.9) can be rewritten as

$$H_{\text{eff}} = \frac{Jz}{\mu_0 N_v} M \tag{2.11}$$

Comparing this result with Weiss' original theory of molecular field, where the magnitude of the effective field acting on each atom was given by

$$H_{\text{eff}} = \lambda M \tag{2.12}$$

and $\lambda$ was of the order of 2000 [8], gives us an estimation of the term $I_{\text{e}} \simeq 0.02$ eV/atom in Eq. (2.5). This estimation gives the right order of magnitude for the exchange energy (typically of the order of 0.05 eV/atom) and justifies the treatment of the spin-orbit interaction (with energies of the order of $10^{-4}$ eV/atom) as a perturbation to the energy of the system.

### 2.4.3 Demagnetising energy

As Kittel introduces in his *Physical theory of ferromagnetic domains* [10], despite the strong exchange interaction (of the order of $10^7$ Oersteds according to Weiss molecular theory) which keeps the magnetic moments aligned in a ferromagnetic material, "It is possible to change the over-all magnetisation of a suitably prepared ferromagnetic speci-

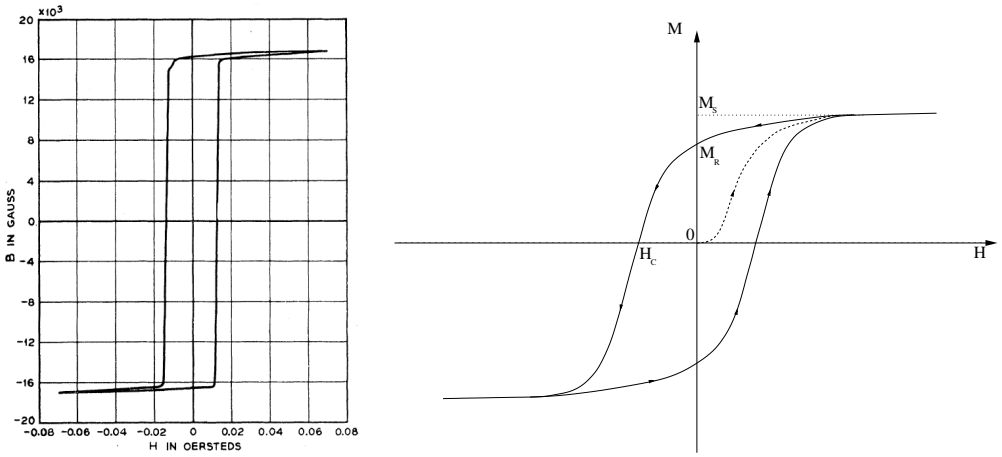


(**a**) (**b**)

Figure 2.3: (a) "Magnetisation curve of single crystal of silicon iron. The B scale is only approximate. (Williams and Shockley, 1949)" (from [10]); (b) Hysteresis loop with characterisation parameters.

men from an initial value of zero (in the absence of an applied field) to a saturation value of the order of 1000 Gauss, by the application of a field whose strength may be of the order of 0.01 Oersteds". The curve showing the spatially averaged sample magnetisation in the direction of the applied field that Kittel refers to is reported in Figure 2.3(a). This curve, called hysteresis loop, is typical of magnetic materials and is characterised by three parameters (shown in Figure 2.3(b)): the saturation magnetisation $M_\mathrm{s}$, the coercive field $H_\mathrm{c}$ and the remanent magnetisation $M_\mathrm{r}$.

Starting from a demagnetised state where $M = 0$ (represented by the origin of the graph) in absence of an applied field, increasing the field the initial curve of a ferromagnet is represented by the dotted curve, also called virgin curve. When all the atomic moments of the material are fully aligned the material reaches its saturation magnetisation, here represented by the coordinate $M_\mathrm{s}$ on the $M$ axis. From this configuration, decreasing the applied field the system follows the plain curve. The first characteristic value encountered on this path is the remanent magnetisation $M_\mathrm{r}$, which expresses the residual magnetisation of the ferromagnet once the field is removed, *i.e.* $H = 0$. With a further decrease of the applied field the second parameter is the coercive field $H_\mathrm{c}$. On the graph it is represented by the point where the curve crosses the $H$ axis and it is the magnitude of the field necessary to remove the residual magnetisation.

To explain the initial demagnetised state in absence of an applied field, an additional energy able to prevail on the ordering effect of exchange energy must be introduced. This energy is the so called demagnetising energy and for convenience of notation its origin will be discussed using the magnetisation vector $\mathbf{M}$, defined as the magnetic dipole $\mathbf{m}$ per

unit volume of material. The expression of the demagnetising energy for a system with magnetisation $\mathbf{M}$ can be written as

$$E_{\text{dem}} = -\frac{\mu_0}{2} \int \mathbf{M}(\mathbf{r}) \cdot \mathbf{H}_{\text{dem}}(\mathbf{r}) \, \mathrm{d}V \tag{2.13}$$

where $\mathbf{H}_{\text{dem}}$ is the so called demagnetising field. The demagnetising field is the part of the dipolar field which passes through the interior of the magnetic body, where the expression of the dipolar field for a magnetic dipole $\mathbf{m}$ at a generic position $\mathbf{r}$ in space is given by

$$\mathbf{h}_{\,\text{dem}}(\mathbf{r}) = \frac{1}{4\pi} \frac{3\mathbf{r}\,(\mathbf{r} \cdot \mathbf{m}) - \mathbf{m}\; r^2}{r^3} \tag{2.14}$$

In the bulk of a magnetic material the demagnetising field is eliminated by the regular head-to-tail configuration assumed by the atomic dipoles, which makes the vector sum of their atomic moments nearly zero, while the presence of a macroscopic demagnetising field is associated to inhomogeneities in the magnetisation or certain conditions at the interfaces of the object.

This is the case of a uniformly magnetised body when the magnetisation has a component along the normal to the surface; at this surface the bulk head-to-tail alignment of the atomic dipoles breaks up and uncompensated "magnetic poles" are created. The demagnetising field associated to this magnetic distribution can be expressed as

$$\mathbf{H}_{\text{dem}} = -\mathbf{N} \cdot \mathbf{M} \tag{2.15}$$

where $\mathbf{N}$ is the so called demagnetising tensor, a second rank symmetric tensor with unit trace. The entries of this tensor depend on the geometric characteristics of the magnetic body and on the susceptibility $\chi$ of the material, where the latter, calling $B$ the intensity of the macroscopic magnetic field $\mathbf{B} = \mu_0 \, ( \, \mathbf{H}_{\text{dem}} + \mathbf{M} \, )$, is defined as

$$\chi = \frac{\mu_0 M}{B} \tag{2.16}$$

and is generally used to express the paramagnetic ($\chi > 0$) or diamagnetic ($\chi < 0$) properties of a material.

In the general case the expression of the demagnetising tensor $\mathbf{N}$ can be only approximated but, for some special geometries where the magnetisation is homogeneous in the sample, it can be calculated exactly. In those cases (ellipsoids, prisms and infinite rods), $\mathbf{N}$ becomes a diagonal tensor and the three entries expressed along the symmetry axes of the body are called demagnetising factors.

The effect of the free magnetic poles on the surface of the magnetic body favours a rearrangement of the magnetisation in order to eliminate the "magnetic surface charges". Calling $\hat{\mathbf{n}}$ the unit normal to the surface, the areal density of these magnetic charges is given by

$$\sigma = \mathbf{M} \cdot \hat{\mathbf{n}} \tag{2.17}$$

and a cancellation is obtained by rotating the magnetisation along the surface of the body. The consequence of this rotation is a non-uniform configuration of the magnetisation, and by discretising the domain Eq. (2.15) can still be used to compute $\mathbf{H}_{\text{dem}}$ (see Sec. 3.2), even if the accuracy of the solution depends on the choice of the discretisation. A more general approach is represented by Maxwell's equations which, for the case of static fields in the absence of macroscopic currents $\mathbf{J}$, can be written as

$$\nabla \times \mathbf{H}_{\text{dem}}(\mathbf{r}) = 0 \qquad ; \qquad \nabla \cdot \mathbf{B}(\mathbf{r}) = 0 \tag{2.18}$$

The left equality in Eq. (2.18) implies that $\mathbf{H}_{\text{dem}}(\mathbf{r})$ can be expressed in terms of a scalar potential $U_{\text{dem}}(\mathbf{r})$ as

$$\mathbf{H}_{\text{dem}}(\mathbf{r}) = -\nabla U_{\text{dem}}(\mathbf{r}) \tag{2.19}$$

while the right one allows to write

$$\nabla \cdot \mathbf{H}_{\text{dem}}(\mathbf{r}) = -\nabla \cdot \mathbf{M}(\mathbf{r}) \tag{2.20}$$

Using Eq. (2.19) and (2.20) together we have

$$\nabla^2 U_{\text{dem}}(\mathbf{r}) = \nabla \cdot \mathbf{M}(\mathbf{r}) \tag{2.21}$$

Inside the magnetic body $\mathbf{M}(\mathbf{r}) \neq 0$ so the solution of Eq. (2.21) can be written as $U_{\text{dem}}(\mathbf{r}) \equiv U^i_{\text{dem}}(\mathbf{r})$. Outside the magnetic body $\mathbf{M}(\mathbf{r}) = 0$ and Eq. (2.21) reduces to

$$\nabla^2 U^o_{\text{dem}}(\mathbf{r}) = 0 \tag{2.22}$$

Moreover, the constraints on the continuity of $\mathbf{H}_{\text{dem}_\parallel}(\mathbf{r})$ and $\mathbf{B}_\perp(\mathbf{r})$ at the interface $S$

lead to the boundary conditions

$$U^i_{\text{dem}}(\mathbf{r}) = U^o_{\text{dem}}(\mathbf{r}) \tag{2.23}$$

$$\frac{\partial U^i_{\text{dem}}(\mathbf{r})}{\partial \hat{\mathbf{n}}} - \frac{\partial U^o_{\text{dem}}(\mathbf{r})}{\partial \hat{\mathbf{n}}} = \mathbf{M}(\mathbf{r}) \cdot \hat{\mathbf{n}} \tag{2.24}$$

where the point $\mathbf{r}$ belongs to the interface $S$ and $\hat{\mathbf{n}}$ is the unit outward normal to the surface of the magnetic body. Finally the condition

$$|U_{\text{dem}}(\mathbf{r} \to \infty)| < K \tag{2.25}$$

with $K$ any positive constant ensures the regularity of the potential $U_{\text{dem}}(\mathbf{r})$ at infinity.

With the definition of boundary conditions the solution of the Eq. (2.21) is completely defined and its analytic expression is given by [8]

$$U_{\text{dem}}(\mathbf{r}) = \frac{1}{4\pi}\left(-\int_{V'} \frac{\nabla' \cdot \mathbf{M}(\mathbf{r}')}{|\mathbf{r}-\mathbf{r}'|}\,\mathrm{d}V' + \int_{S'} \frac{\hat{\mathbf{n}} \cdot \mathbf{M}(\mathbf{r}')}{|\mathbf{r}-\mathbf{r}'|}\,\mathrm{d}S'\right) \tag{2.26}$$

where the first integral is over the magnetic body, the second over its surface. Using Eq. (2.19) the demagnetising field $\mathbf{H}_{\text{dem}}$ in Eq. (2.13) can therefore be written as

$$\mathbf{H}_{\text{dem}}(\mathbf{r}) = \frac{1}{4\pi}\left(-\int_{V'} \frac{(\mathbf{r}-\mathbf{r}')\ \nabla' \cdot \mathbf{M}(\mathbf{r}')}{|\mathbf{r}-\mathbf{r}'|^3}\,\mathrm{d}V' + \int_{S'} \frac{(\mathbf{r}-\mathbf{r}')\ \hat{\mathbf{n}} \cdot \mathbf{M}(\mathbf{r}')}{|\mathbf{r}-\mathbf{r}'|^3}\,\mathrm{d}S'\right) \tag{2.27}$$

From this result it turns out that the demagnetising energy in Eq. (2.13) can only be positive or nil [11]. Therefore the minimum of the demagnetising energy is obtained when the net magnetisation of a body is zero, a configuration obtained by splitting the sample in domains as in Figure 2.4. In this case the overall magnetisation of the sample is cancelled because of the random orientation of the magnetisation in the domains, though the magnetisation in each domain is kept aligned by the exchange energy.

At the boundaries between domains the magnetisation rotates smoothly to avoid a large exchange energy and the transition region is called a domain wall. The hysteresis loops in Figure 2.3 are due to the motion of domain walls and rotation of domains under the effect of the applied field (a simplified representation is shown in Figure 2.5) and the statement at the beginning of the section can now be interpreted as the ease to perform these operations when the magnetisation in the sample is not uniform but divided into domains.

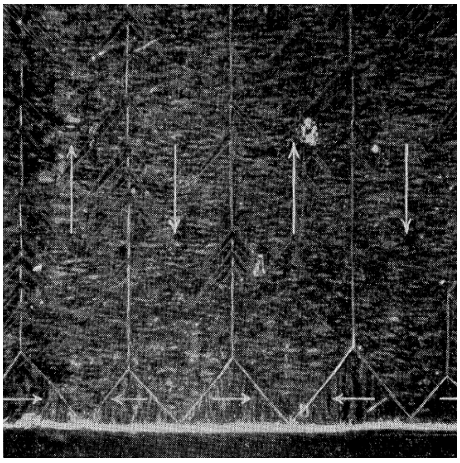

Figure 2.4: "Retouched photograph of domains closure in Si-Fe crystal (Williams)" (from [10]).

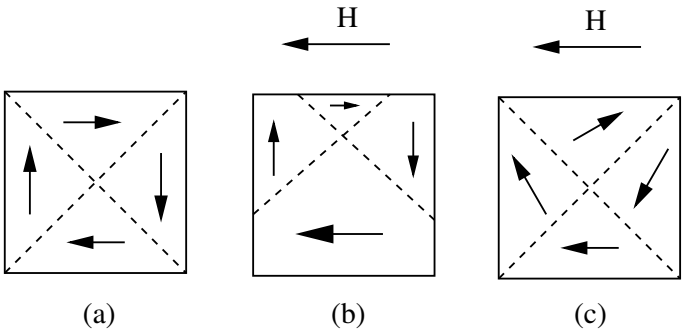


Figure 2.5: Fundamental magnetisation processes. (a) unmagnetised sample (b) sample magnetised by domain growth (boundary displacement) (c) sample magnetised by domain formation (from [10]).

### 2.4.4 Anisotropy energy

Anisotropy indicates the tendency of the magnetisation to lie along certain directions. Magnetic anisotropy can have various origins, but the most important in the study of micromagnetic systems are magnetocrystalline anisotropy and shape anisotropy.

#### Magnetocrystalline anisotropy

Magnetocrystalline anisotropy is the effect of the spin-orbit interaction between the electrons orbitals and the crystal lattice. The coupling occurs as the electron orbits tend to deform along crystallographic axes and spins show this effect, *i.e.* a spin-orbit interaction, favouring directions related to the structure of the material.

These preferential directions are called easy axes, and the anisotropy energy of a material is expressed by an energy density $K$, which may be the sum of multiple contributions, associated to the structure of the material.

Magnetocrystalline anisotropy can be distinguished in uniaxial, cubic or an higher odd order depending on the terms used to describe the energy surface and it is associated to an equivalent number of preferred crystallographic axes for the magnetisation.

Typically only the uniaxial and cubic anisotropies are considered and magnetic materials can show both types. The energies associated with these anisotropies are expressed using the directional cosine $\alpha$ of the magnetisation-to-axis angles

$$\alpha_a = \frac{m_a}{|\mathbf{m}|} = \frac{\mathbf{m}\cdot\mathbf{a}}{|\mathbf{m}|} \qquad \alpha_b = \frac{m_b}{|\mathbf{m}|} = \frac{\mathbf{m}\cdot\mathbf{b}}{|\mathbf{m}|} \qquad \alpha_c = \frac{m_c}{|\mathbf{m}|} = \frac{\mathbf{m}\cdot\mathbf{c}}{|\mathbf{m}|} \tag{2.28}$$

where **a**, **b** and **c**, so called for historical reasons, are the crystallographic axes and **m** is the single atomic moment. The energy surfaces are expressed phenomenologically as series expansions on these angles, and the truncation to the third term is appropriate for most materials [12].

With these conventions, the uniaxial anisotropy energy density, typical for hexagonal crystals, has an energy given by:

$$\mathcal{E}_{\text{uni}} = K_0^{\text{u}} - K_1^{\text{u}}\alpha_c^2 + K_2^{\text{u}}\alpha_c^4 \tag{2.29}$$

while the cubic anisotropy energy density, typical for cubic crystals, has the following expression:

$$\mathcal{E}_{\text{cub}} = K_0^{\text{c}} + K_1^{\text{c}}\left(\alpha_a^2\alpha_b^2 + \alpha_b^2\alpha_c^2 + \alpha_a^2\alpha_c^2\right) + K_2^{\text{c}}\left(\alpha_a^2\alpha_b^2\alpha_c^2\right) \tag{2.30}$$

The values of the various $K$ factors are measured taking the difference in energy between a configuration with the magnetisation aligned with one of these easy axes and a configu-

ration with the magnetisation aligned perpendicularly to it, and their values may depend strongly on the temperature.

**Shape anisotropy**

Shape anisotropy is a direct consequence of the demagnetising field which tends to align the magnetisation locally parallel to the material's surface. Its effect is particularly evident in samples with reduced dimensions and as an example the expression for a thin film is easily obtained.

As the shape anisotropy is a result of the demagnetising field, the derivation will be presented using the same notation adopted for the demagnetising energy, that is using the magnetisation vector $\mathbf{M}$ instead of the atomic moments $\mathbf{m}_i$.

In an ideal case of infinite film on the x-y plane, the demagnetising factors along two axes lying on the plane are 0, while the demagnetising factor along the z-axis, perpendicular to the plane, is 1. If the magnetisation is uniform and directed along an angle $\alpha$ from the plane of the film and $\theta$ from the x-axis on the x-y plane, its shape anisotropy field is given by

$$\begin{aligned} H_{\text{sha}} &= -N_{\text{x}} M_{\text{x}} - N_{\text{y}} M_{\text{y}} - N_{\text{z}} M_{\text{z}} && (2.31) \\ &= -\left(0 \cdot M \cos\alpha \cos\theta + 0 \cdot M \cos\alpha \sin\theta + 1 \cdot M \sin\alpha\right) && (2.32) \end{aligned}$$

where $M$ is the magnitude of the magnetisation and the direction of $\mathbf{H}_{\text{sha}}$ is out of plane. Calling $V$ the volume of the sample, the expression of the shape anisotropy energy is easily written as

$$\begin{aligned} E_{\text{sha}} &= -\frac{\mu_0}{2}\, \mathbf{H}_{\text{sha}} \cdot \mathbf{M}\, V \\ &= -\frac{\mu_0}{2} \left(0 \cdot M^2 \cos^2\alpha \cos^2\theta + 0 \cdot M^2 \cos^2\alpha \sin^2\theta - 1 \cdot M^2 \sin^2\alpha\right) V \\ &= \frac{\mu_0}{2} V M^2 \sin^2\alpha && (2.33) \end{aligned}$$

and the minimum of the energy is obtained when the angle $\alpha$ is a multiple of $\pi$, that is when the magnetisation lies on the plane of the film.

## 2.5 Micromagnetic model

To deal with the complexity of the various energy terms in multi-atom systems, an important concept is represented by the mean field approximation. With this assumption all the atom-atom interactions are expressed in a statistical form and every atomic dipole moves under the influence of a local effective field created by all the other atoms. This approach,

derived by Weiss' idea of the molecular field, has been refined by Brown [13] in a theory that he called *micromagnetics*, and has given a major impulse to the comprehension of magnetic materials.

Neglecting its atomistic origin, this theory assumes the magnetisation to be a continuous and differentiable function and uses the local mean field approximation to describe the metastable configurations of a magnetic system. Taking the material as a continuum, this model implicitly assumes that any characteristic length is large compared to the unit cell dimension and the magnetisation is a smooth function over the domain of the magnetic body. Moreover, the randomisation effect of the temperature on the magnetisation is neglected and therefore the model is only applicable for temperatures well below the Curie temperature of the material.

Despite of these limitations, Brown's theory, together with the work of Landau and Lifshitz on the time evolution of the magnetisation, allows to reproduce experimental magnetic patterns and describe complex magnetic systems with high accuracy [12]. For this reason in the rest of the thesis the micromagnetic theory will be used as the reference model for the numerical investigation of magnetic structures.

### 2.5.1 Energies in the continuous model

In Sec. 2.4 we have introduced the physical origin and the expression for all the relevant energies characterising a micromagnetic system. If now we use the local mean field approximation and substitute the previous atomic magnetic moment $\mathbf{m}$ with a continuous and differentiable magnetisation function $\mathbf{M}(\mathbf{r})$, the previous energies can be rewritten as integrals over the magnetic body. Hence the expression for the Zeeman energy becomes

$$E_{\text{Zee}} = -\mu_0 \int_V \mathbf{H}_{\text{ext}} \cdot \mathbf{M} \, \mathrm{d}V \tag{2.34}$$

where now also the applied field $\mathbf{H}_{\text{ext}}(\mathbf{r})$ is a function of the position $\mathbf{r}$.

The exchange energy integral can be derived assuming a smooth variation of the magnetisation vector over the lattice spacing. This is equivalent to have small $\alpha_{i,j}$ in Eq. (2.7), that is small angles between the generic vectors $\mathbf{m}_i$ and $\mathbf{m}_j$.

In that case $\cos(\alpha_{i,j})$ can be approximated by its expansion $\cos(\alpha_{i,j}) \approx 1 - \frac{\alpha_{i,j}^2}{2}$ and calling $C$ the constant term we can rewrite Eq. (2.7) as

$$E_{\text{exch}} \approx C + \frac{J}{2} \sum_{i=1}^{N} m_i \sum_{j=1|_{j\neq i}}^{N} m_j \, \alpha_{i,j}^2 \tag{2.35}$$

The magnitude of magnetisation is supposed to be constant over all the material, so

the single moments have magnitude $m_i = m_j = m$ and we can split the vector of each moment in its magnitude $m$ and direction $\mathbf{u}_i$ components: $\mathbf{m}_i = m \cdot \mathbf{u}_i$. If the angle $\alpha_{i,j}$, here considered positive, is small we can write:

$$\begin{aligned} m\,\alpha_{i,j} &\approx |\mathbf{m}_j - \mathbf{m}_i| && (2.36)\\ &\approx m\,|\mathbf{u}_j - \mathbf{u}_i| && (2.37) \end{aligned}$$

and

$$\alpha_{i,j} \approx |\mathbf{u}_j - \mathbf{u}_i| \quad (2.38)$$

The expression $|\mathbf{u}_j - \mathbf{u}_i|$ can be computed using a Taylor expansion of the unit vector $\mathbf{u}_j$ on the lattice

$$\begin{aligned} \mathbf{u}_j &\approx \mathbf{u}_i + (\mathbf{r}_{j,i} \cdot \nabla)\mathbf{u}_i && (2.39)\\ |\mathbf{u}_j - \mathbf{u}_i| &\approx |(\mathbf{r}_{j,i} \cdot \nabla)\mathbf{u}_i| && (2.40) \end{aligned}$$

where $\mathbf{r}_{j,i}$ is the lattice vector $|\mathbf{r}_j - \mathbf{r}_i|$. The result of the approximation is therefore

$$\alpha_{i,j} \approx |(\mathbf{r}_{j,i} \cdot \nabla)\mathbf{u}_i| \quad (2.41)$$

Now we can use the symmetry of the crystal to further simplify equations and for simplicity we show here the case of a simple cubic cell. In this case the lattice vector $\mathbf{r}_{j,i}$ has constant magnitude in all the crystallographic directions and if we call the edge of the crystallographic unit cell $a = |\mathbf{r}_{j,i}|$, then Eq. (2.35) becomes

$$\begin{aligned} E_{\text{exch}} &= \frac{Jm^2}{2} \sum_{i=1}^{N} \sum_{j=1|_{j\neq i}}^{N} |(\mathbf{r}_{j,i} \cdot \nabla)\mathbf{u}_i|^2 && (2.42)\\ &= Jm^2 \sum_{i=1}^{N} \sum_{\text{neighbouring } j} |(\mathbf{r}_{j,i} \cdot \nabla)\mathbf{u}_i|^2 && (2.43) \end{aligned}$$

where each interaction is considered once and hence a 2 factor is added. Writing explicitly

the terms in the sum and simplifying all the null terms in the expression we obtain

$$E_{\text{exch}} = 2a^2 Jm^2 \sum_{i=1}^{N} (\nabla \mathbf{u}_i)^2 \tag{2.44}$$

$$= \frac{2Jm^2}{a} \sum_{i=1}^{N} (\nabla \mathbf{u}_i)^2 \, a^3 \tag{2.45}$$

$$= \frac{2Jm^2}{a} \int_V \Big(\nabla \mathbf{u}(\mathbf{r})\Big)^2 \, \mathrm{d}V \tag{2.46}$$

$$= A \int_V \Big(\nabla \mathbf{u}(\mathbf{r})\Big)^2 \, \mathrm{d}V \tag{2.47}$$

where $\mathbf{u}(\mathbf{r})$ is a unit vector pointing in the direction of the magnetisation, the volume of each cell is $a^3$ and $A$ is the exchange stiffness constant. In this case the derivation of $A$ has been done for a cubic cell (thus the factor 2 in Eq. (2.44) coming from the sum over nearest neighbours), but its general expression is given by

$$A = 2Jm^2 \frac{z}{a} \tag{2.48}$$

with the factor $z$ to account for the crystallographic configuration. In particular $z = 1$ for the simple cubic lattice, $z = 2$ for body-centred cubic lattice and $z = 4$ for face-centred cubic lattice.

Concerning the demagnetising energy, the expression used with the continuous model is the same already presented in Eq. (2.13). The same argument holds for the expression of the shape anisotropy given in Eq. (2.31), while for the magnetocrystalline anisotropy the expressions Eq. (2.29) and (2.30) become

$$E_{\text{uni}} = \int_V K_0^{\text{u}} - K_1^{\text{u}} \alpha_c^2 + K_2^{\text{u}} \alpha_c^4 \, \mathrm{d}V \tag{2.49}$$

and

$$E_{\text{cub}} = \int_V K_0^{\text{c}} + K_1^{\text{c}} \big(\alpha_a^2 \alpha_b^2 + \alpha_b^2 \alpha_c^2 + \alpha_a^2 \alpha_c^2\big) + K_2^{\text{c}} \big(\alpha_a^2 \alpha_b^2 \alpha_c^2\big) \, \mathrm{d}V \tag{2.50}$$

## 2.6 Characteristic lengths

Depending on the nature of the phenomena under investigation, magnetic materials exhibit interesting physics at different length scales [14]. Concerning the structures described by the micromagnetic theory, that is those at length scale between few nanometres and some micrometres, the main characteristic lengths are the exchange length and the domain wall

width.

The exchange length can be interpreted as the distance that is defined by a balance of exchange energy and demagnetising energy. If we define the stray field energy constant $K_{\mathrm{m}}$ as

$$K_{\mathrm{m}} = \frac{1}{2}\mu_0 M_{\mathrm{s}}^2 \tag{2.51}$$

then the exchange length is defined as

$$\lambda_{\mathrm{ex}} = \sqrt{\frac{A}{K_{\mathrm{m}}}} = \sqrt{\left(\frac{2A}{\mu_0 M_{\mathrm{s}}^2}\right)} \quad . \tag{2.52}$$

Here $M_{\mathrm{s}}$ is the saturation magnetisation of the material, $\mu_0$ the permeability of free space and $A$ is the exchange stiffness constant given in Eq. (2.48). $A$ has values of the order of $10^{-11}$J/m so that $\lambda_{\mathrm{ex}}$ is of the order of several nanometres for typical ferromagnetic metals.

For particles smaller than the exchange length the magnetisation shows a quasi-uniform configuration, with a deviation from the complete alignment due to the shape of the particle. The reason of the deviation is in the constraints on the magnetisation at the interfaces, and the consequence is that a uniform magnetisation can be achieved only in ellipsoidal particles.

Though such condition on the shape is hard to find in nature, if the size of the particle is small enough the deviation is generally negligible and the magnetic behaviour can be described as that of a uniformly magnetised particle, whose configuration is called single domain, or mono-domain, state.

While in soft magnetic materials (materials with small coercivity) a domain wall can be observed only if the size is larger than the exchange length, for hard magnetic materials (materials with large coercivity) such structures can appear only if the size exceeds the domain wall width.

This is because in hard magnetic materials the anisotropy energy takes the role of the demagnetising energy as the main driving force in the formation of domain walls, and the domain wall width can have two expressions depending on the geometry of the magnetic system.

In systems where the rotation of the magnetisation occurs in a helical fashion, developing a 3D structure like in Figure 2.6(a), the wall is called Bloch wall and the associate domain wall width can be derived expressing the exchange and anisotropy energy of Eq. (2.47) and (2.49) per unit area of the wall in polar coordinates as [15]

$$\gamma_w = \int_{-\infty}^{\infty} \left[A\varphi'^2 + K\cos^2\varphi\right] \mathrm{d}x, \quad \varphi(-\infty) = \frac{\pi}{2}, \;\; \varphi(\infty) = -\frac{\pi}{2} \tag{2.53}$$

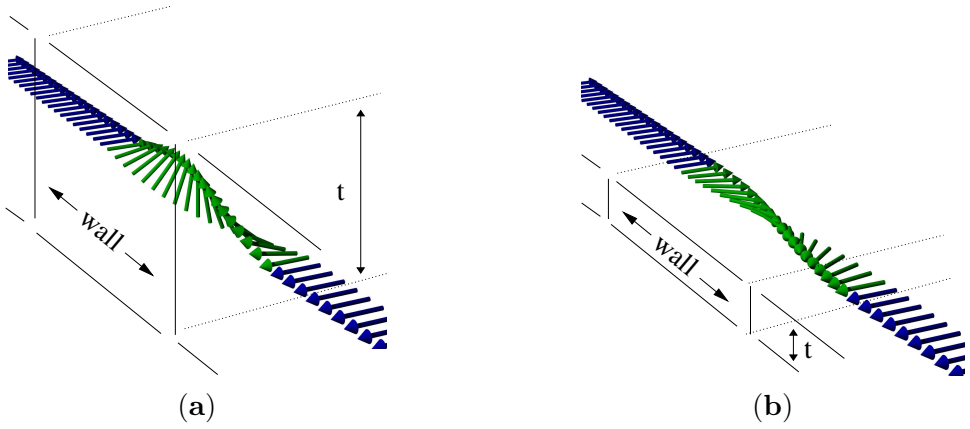


Figure 2.6: (a) Bloch wall: the magnetisation rotates through a 3D structure; (b) Néel wall: the magnetisation rotates on a plane when the thickness $t$ of the sample is smaller than the domain wall width.

where $\varphi$ is the angle on the plane orthogonal to the axis $x$ of the wall (see Figure 2.7(a)).

The function $\varphi(x)$ which minimises $\gamma_w$ under the given boundary conditions can be shown to be [15]

$$\sin\varphi = \tanh\xi \;\; ; \;\; \xi = \frac{x}{\sqrt{A/K}} \tag{2.54}$$

and the profile of the domain wall is shown in Figure 2.8.

The width is obtained from the profile using the tangent to the curve at the centre of the wall and corresponds to

$$w_{\mathrm{B}} = \pi\sqrt{\frac{A}{K}} \tag{2.55}$$

In systems where the thickness $t$ of the sample is smaller than the domain wall width, the Bloch wall induces magnetic charges on the surface of the sample, increasing the shape anisotropy energy. This extra energy can be avoided if the magnetisation in the wall rotates on a plane rather than through an helix structure, like in Figure 2.6(b) and 2.7(b), and in this case the wall is called Néel wall. The width of the Néel wall can be obtained with the same procedure used for the Bloch wall and its expression is [15]

$$w_{\mathrm{N}} \simeq \pi\sqrt{\frac{2A}{K_1}} \tag{2.56}$$

with the 2 factor due to the effect of magnetostatic energy [8].

In ferromagnetic metals the characteristic length for the Bloch wall is of the order of

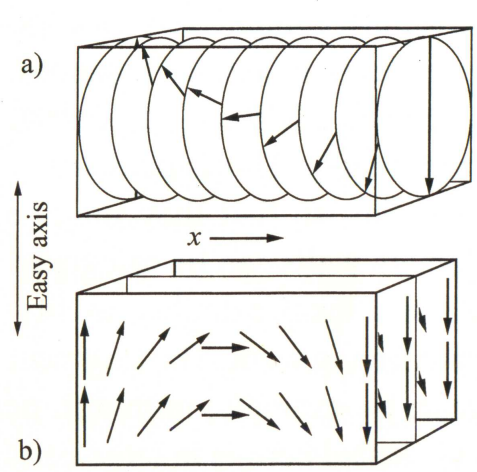


Figure 2.7: Rotation of magnetisation in Bloch (a) and Néel (b) domain walls. (reproduction from [15]).

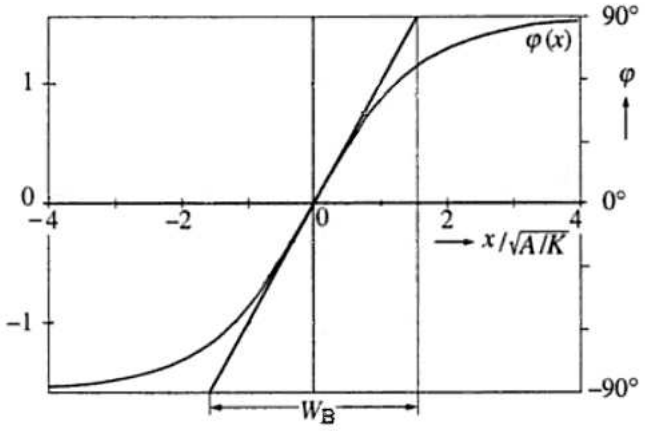


Figure 2.8: Domain wall profile for a Bloch wall: $w_B$ corresponds to the definition of the domain wall width (reproduction from [15]).

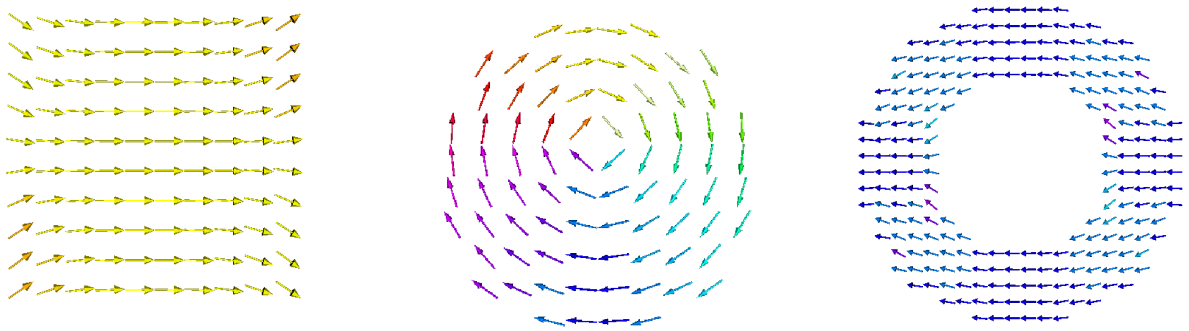

(**a**) (**b**) (**c**)

Figure 2.9: Curled magnetisation patterns. The competing tendency to minimize both the demagnetising energy and the exchange energy results in configurations such as the flower state (a), the vortex state (b) or the onion state in rings (c).

tens of nanometres [16], while the Néel wall can have a characteristic length of more than 1 $\mu$m for a film thickness of few nm [8].

When the size of the specimen is comparable with one of the two aforementioned characteristic lengths, the system may find easier to create curled magnetisation patterns rather than complete domain walls. Some typical patterns are shown in Figure 2.9, where, starting from the left, we have a flower state, a vortex state and an onion state. In a flower state the magnetisation is mostly aligned along the main axis of the specimen, and "opens up" at its edges; the vortex state is characterised by a magnetisation arranged in a close pattern, whose centre is called vortex core, while in the onion state the magnetisation bends along the circumference of holes created in a sample, following their surface. The onion state and vortex state are characteristic of ring-shaped magnetic samples, whose properties will be discussed in Chapters 6 and 7.

## 2.7 Stoner-Wohlfarth model

Although the behaviour of a generic particle is given by the balance between exchange energy, demagnetising field, anisotropy and applied field, in some practical cases a good approximation of the magnetic hysteresis shown in Figure 2.3 can be derived theoretically by simply assuming a uniform magnetisation and using the anisotropy contribution to the energy of the system. The model which describes such a system is called Stoner-Wohlfarth model [17] and, despite the simplicity of the approach, the predictions are generally good for simple magnetic objects with a size comparable to the exchange length of the material [12], or for objects with uniform-like magnetisation evolution.

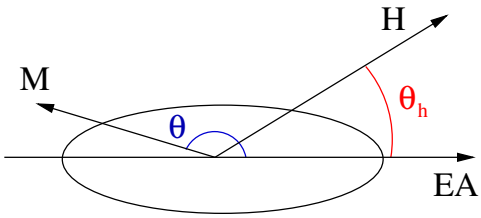


Figure 2.10: Coordinate system for the Stoner-Wohlfarth particle. $H$ is the applied field, $M$ the magnetisation and EA is the easy axis of the anisotropy.

The model assumes the magnetic object to be an ellipsoidal particle in a mono-domain configuration where the magnetisation rotates coherently. The anisotropy is supposed to be uniaxial along the main axis of the particle. Recalling the expression of the anisotropy energy (Eq. (2.29)), the energy density of the system in the presence of an applied field can be written as [8]

$$\varepsilon(\theta) = -K_{\mathrm{u}} \cos^2 \theta - \mu_0 \, H M_{\mathrm{s}} \cos(\theta_{\mathrm{h}} - \theta) \tag{2.57}$$

where $K_{\mathrm{u}}$ is the anisotropy energy density (which may contain also contributions from shape anisotropy), $\theta$ the direction of the magnetisation $\mathbf{M}$ (of constant magnitude $M_{\mathrm{s}}$) with respect to the easy axis and $\theta_{\mathrm{h}}$ the angle between the applied field and the easy axis (see Figure 2.10).

The graphs of $\varepsilon(\theta)$ for different values of the applied field are shown in Figure 2.11. The fields are such that $H_3 > H_2 > H_1 > H_0 = 0$ and the minima of the curves correspond to equilibrium configurations of the magnetisation. The magnetisation at zero applied field (curve with $H = H_0 = 0$) aligns with the easy axis of the particle and without lack of generality we can assume that it points along the negative direction of this axis (so that the equilibrium configuration is with $\theta = 180°$).

Increasing the applied field (curves with $H = H_1 > H_0$ and $H_2 > H_1$) the initial equilibrium configuration becomes a metastable state and the minimum of the energy slowly shifts from $\theta = 180°$ towards lower values of $\theta$.

For an applied field sufficiently large (curve with $H = H_3$) the metastable state becomes an unstable configuration and the system finds a new equilibrium configuration at $\theta \simeq 0°$. This value of the applied field represents the switching field of the magnetisation.

In the Stoner-Wohlfarth model the switching field $H_{\mathrm{c}}$ as well as the angle $\theta$ at witch the switching occurs have an analytical expression and the graph of the coercivity $H_{\mathrm{c}}$ in the whole range $0° - 90°$ as a function of $\theta_{\mathrm{h}}$ is shown in Figure 2.12.

As shown in Figure 2.13 tuning the angle $\theta_{\mathrm{h}}$ the behaviour of the system can go from

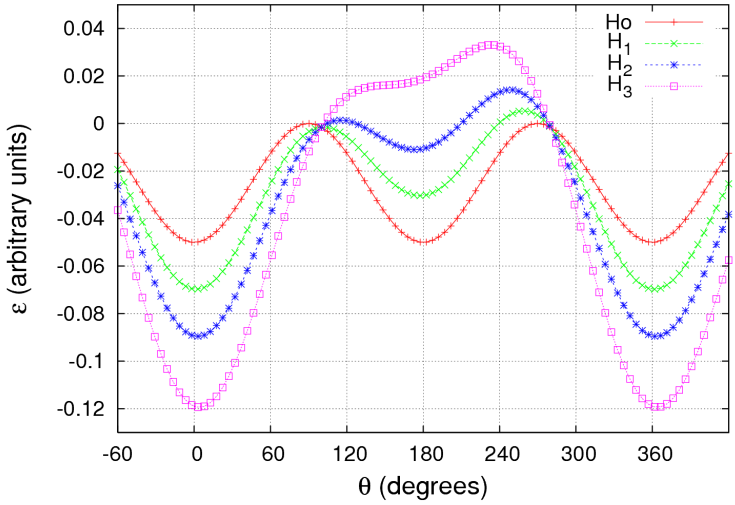


Figure 2.11: Energy density $\varepsilon$ for different magnitudes $H_0, H_1, H_2, H_3$ of the applied field and angles $\theta$. For increasing fields $H_3 > H_2 > H_1 > H_0 = 0$ the metastable state at $\theta = 180$ gradually shifts towards an unstable condition and at $H = H_3$ the magnetisation switches to the new equilibrium configuration with $\theta = 0°$.

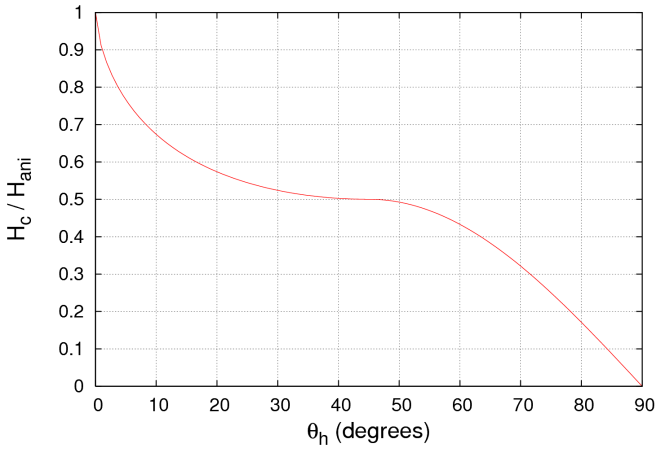


Figure 2.12: Coercive field in the Stoner-Wohlfarth model as a function of the applied field angle.

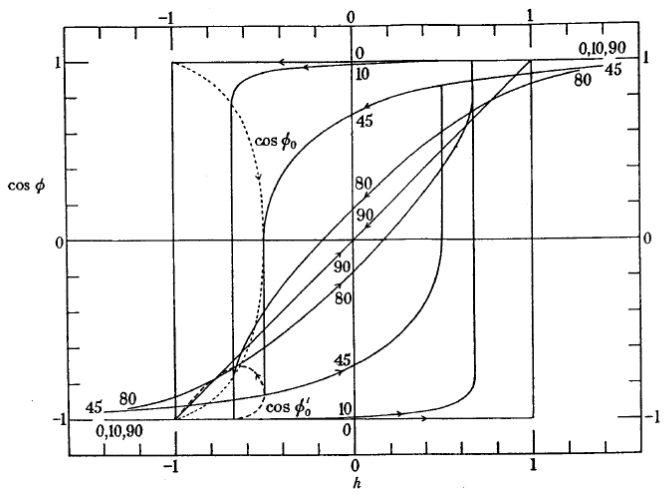


Figure 2.13: Hysteresis loops at various angles of applied field (from original manuscript [17]). The field is expressed in terms of the anisotropy field $h = H/H_{\text{ani}}$ and the angle $\theta_{\text{h}}$ between the easy axis and the direction of the field is shown, in degrees, by the numbers on the curves. The magnetisation in the positive field direction is given by $M_{\text{s}} \cos\phi$, where $M_{\text{s}}$ is the saturation magnetisation and $\phi$ is the angle $\theta$ used in Figure 2.10. The dotted curves give $\cos\theta_0$ and $\cos\theta_0'$ where $\theta_0$ and $\theta_0'$ are the angles made with the positive field direction by the magnetisation vector at the beginning and end of the discontinuous change at the switching value of the field.

a square-like hysteresis loop to a magnetisation reversal without hysteresis, potentially describing a wide range of magnetic systems.

Although the model can be extended to describe particles with cubic anisotropy or systems with random anisotropy distribution, its simplicity is one of its main limitations. In fact the assumption of coherent rotation is a strong approximation in situations where the magnetisation reversal occurs via curling or buckling, resulting in an overestimate of the coercive field of the system. Moreover, as the Stoner-Wohlfarth model describes only equilibrium states of the magnetisation, it lacks the description of the magnetisation dynamics, thus preventing to describe systems characterised by domain wall formation or movement during the magnetisation reversal.

## 2.8 Magnetisation evolution

To study the dynamics of magnetic systems, a common approach is to start from the analysis of the points of (local) minimum of the energy. Seeking these points of minimal energy is known as the micromagnetic problem and various techniques have been developed for its solution.

Since the evolution of the magnetisation occurs through energy minima, Brown proposed a variational approach to the problem where a small variation of the magnetisation vector around its equilibrium value $\mathbf{M}_0 = M_0 \cdot \mathbf{u}_0$ does not change the energy.

Considering a system with uniaxial anisotropy, in mathematical terms this is expressed taking the functional of the total energy

$$\begin{aligned} E_{\text{total}} &= E_{\text{Zee}} + E_{\text{uni}} + E_{\text{exch}} + E_{\text{dem}} \qquad (2.58) \\ &= \int_V \Big[ -\mu_0 \, M_\text{s} \, \mathbf{u}(\mathbf{r}) \cdot \mathbf{H}_{\text{ext}}(\mathbf{r}) - K_1^\text{u} \left( \mathbf{u}(\mathbf{r}) \cdot \mathbf{c} \right)^2 + \\ &\quad + A \Big( \nabla \mathbf{u}(\mathbf{r}) \Big)^2 - \frac{\mu_0}{2} \, M_\text{s} \, \mathbf{u}(\mathbf{r}) \cdot \mathbf{H}_{\text{dem}}(\mathbf{r}) \Big] \, \mathrm{d}V \qquad (2.59) \end{aligned}$$

and imposing that

$$\frac{\delta E_{\text{total}}}{\delta \mathbf{u}_0} = 0 \qquad (2.60)$$

After some mathematical manipulation we obtain three equations for the components of $\mathbf{u}(\mathbf{r})$ along the three axes x, y and z. These are called Brown's equations and can be written together as [12]

$$\mathbf{u}(\mathbf{r}) \times \left( 2A \nabla^2 \mathbf{u}(\mathbf{r}) + \mu_0 M_\text{s} \mathbf{H}(\mathbf{r}) + 2K_1^\text{u} \Big( \mathbf{u}(\mathbf{r}) \cdot \mathbf{c} \Big) \mathbf{c} \right) = 0 \qquad (2.61)$$

or

$$\mu_0 M_\text{s} \mathbf{u}(\mathbf{r}) \times \left( \frac{2A}{\mu_0 M_\text{s}} \nabla^2 \mathbf{u}(\mathbf{r}) + \mathbf{H}(\mathbf{r}) + \frac{2K_1^\text{u}}{\mu_0 M_\text{s}} \Big( \mathbf{u}(\mathbf{r}) \cdot \mathbf{c} \Big) \mathbf{c} \right) = 0 \qquad (2.62)$$

where $\mathbf{H}(\mathbf{r})$ is now $\mathbf{H}_{\text{ext}}(\mathbf{r}) + \mathbf{H}_{\text{dem}}(\mathbf{r})$. At equilibrium the magnetisation must therefore be locally aligned with an effective field

$$\mathbf{H}^{\text{eff}}(\mathbf{r}) = \frac{2A}{\mu_0 M_\text{s}} \nabla^2 \mathbf{u}(\mathbf{r}) + \mathbf{H}(\mathbf{r}) + \frac{2K_1^\text{u}}{\mu_0 M_\text{s}} \Big( \mathbf{u}(\mathbf{r}) \cdot \mathbf{c} \Big) \mathbf{c} \qquad (2.63)$$

In order to compute the time evolution of the magnetisation towards the equilibrium state, we need to know this effective field for every point in space. From classical physics we know that a magnetic moment subject to an applied field simply precesses around the field direction and their alignment can be achieved only in presence of a damping factor as shown in Figure 2.14.

One equation which describes such an evolution has been introduced by Gilbert [18]:

$$\frac{\mathrm{d}\mathbf{M}(\mathbf{r})}{\mathrm{d}t} = -\gamma \Big( \mathbf{M}(\mathbf{r}) \times \mathbf{H}^{\text{eff}}(\mathbf{r}) \Big) + \frac{\alpha}{M_\text{s}} \left( \mathbf{M}(\mathbf{r}) \times \frac{\mathbf{M}(\mathbf{r})}{dt} \right) \qquad (2.64)$$

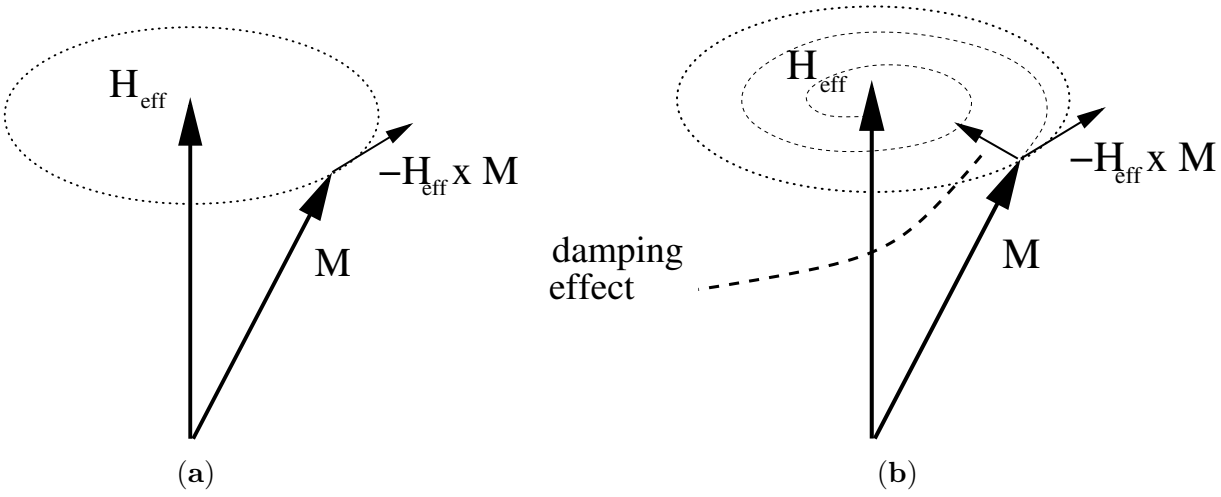


Figure 2.14: Damping effect on magnetisation evolution: a) undamped dynamics b) dynamics in presence of a damping term.

where $\gamma$ is the gyromagnetic ratio and $\alpha$ a phenomenological damping parameter. With some manipulation this equation can be transformed into another one which is easier to solve due to the absence of the magnetisation time derivative on the right-hand side. This is called Landau-Lifshitz-Gilbert [19] equation and is written as

$$\frac{\mathrm{d}\mathbf{M}(\mathbf{r})}{\mathrm{d}t} = -\frac{\gamma}{1+\alpha^2}\Big(\mathbf{M}(\mathbf{r}) \times \mathbf{H}^{\mathrm{eff}}(\mathbf{r})\Big) - \frac{\gamma\alpha}{M_{\mathrm{s}}(1+\alpha^2)}\Bigg(\mathbf{M}(\mathbf{r}) \times \Big(\mathbf{M}(\mathbf{r}) \times \mathbf{H}^{\mathrm{eff}}(\mathbf{r})\Big)\Bigg) \quad (2.65)$$

Given an initial magnetisation $\mathbf{M}_0 = \mathbf{M}(t_0)$, one can in principle compute the solution of Eq. (2.65). To compute numerically the effective field from Eq. (2.63) on the right-hand side of Eq. (2.65), the most difficult part is Eq. (2.26), which needs to be solved to find the magnetic scalar potential $U_{\mathrm{dem}}$ for the demagnetizing field $\mathbf{H}_{\mathrm{dem}}$ in Eq. (2.19). The two standard approaches used to solve Eq. (2.19) are the Finite Difference Method (FDM) and the Finite Element Method (FEM) and the differences between these two methods are presented in Chapter 3.

## 2.9 Applications of magnetic materials

The interplay among the various energies introduced in Sec. 2.4 gives magnetic materials a rich set of tunable characteristics which are associated to as many fields of application. Besides "common" applications, such as in radio speakers, credit cards, electric engines or sensors, there are other applications closer to the forefront of technology, such as magnetically levitated trains (Maglev), magnetic resonance imaging (MRI), particle accelerators

and magnetic bottles for nuclear fusion experiments.

Concerning magnetic phenomena found in nature, two of the most important are the natural shield from solar wind represented by the magnetosphere, with one of the consequences being aurorae, and the reversal of the Earth magnetic field over time, which is studied by a branch of science called paleomagnetism and has led to the theory of plate tectonics and continental drift [20].

Among all these functions, one of the most interesting applications of magnetic materials is in data storage devices, a field which has shown an impressive rate of development in the last 50 years but where practical limits on the maximum areal density achievable with current manufacturing techniques start to become apparent [21].

### 2.9.1 Hard disk drives

In a hard disk drive a bit of information is physically represented by a so called bit cell. In each cell, containing several magnetic grains in a 2D arrangement, the magnetisation given by the average remanent state of the grains can be uniform or change its orientation going from one side of the cell to the other. As shown in Figure 2.15, in magnetic disks these cells are lined-up in tracks, equally spaced, with the physical extension given by the density of data of the medium. Following a magnetic track, if the magnetisation orientation changes over the interval of the cell the datum is interpreted as a 1, if the orientation is constant the datum is a 0.

If the transition between the two magnetisation directions is not well defined within a cell, in the reading process a cell encoding a 1 may be misclassified as encoding a 0. This problem is technically identified as the noise of the medium, and can be avoided only if each bit cell contains a large number of grains (of the order of 50-100). The approach used so far to increase the areal density maintaining a sufficient number of grains per cell has been to reduce the size of the grains.

However, below a certain size the grains are subject to the SuperParamagnetic Limit (SPL), expressed by an energy barrier over which the remanent state is no more a stable state of the magnetisation, but it can reverse spontaneously due to the thermal energy of the system. Such energy barrier is given by

$$E_{\mathrm{b}} = KV \tag{2.66}$$

where $K$ is the anisotropy energy density (usually taken as $K_1$ in Eq. (2.29) or (2.30)) and $V$ the effective volume of the particle. The thermal stability of a grain (expressed by the expected time before the magnetisation reversal) can be estimated by the Arrhenius-Neél

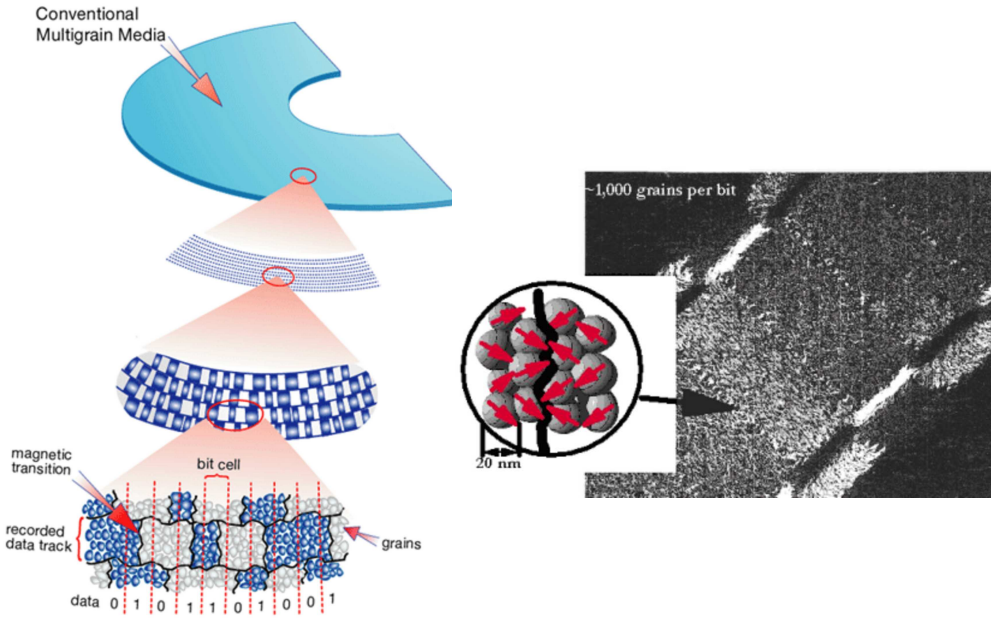


Figure 2.15: Bit cells on a conventional hard drive (courtesy of Hitachi GST).

law

$$\tau = \tau_0 \exp^{E_\mathrm{b}/k_\mathrm{B}T} \tag{2.67}$$

where $k_\mathrm{B}$ is the Boltzmann's constant, $T$ the absolute temperature and $\tau_0$ the inverse of the attempt frequency assumed to be of the order of $10^{-9}$ to $10^{-11}$ s [22, 23, 24].

As the energy density $K$ is a multiplicative factor in Eq. (2.66), anisotropy properties are commonly exploited to increase the energy barrier $E_\mathrm{b}$.

This is achieved using anisotropic materials that stabilise the direction of the magnetisation along the intended axes but, although higher anisotropy means higher control on the magnetisation direction, if the value is too high the writing of data may be impossible.

A simple calculation using Eq. (2.67) results in a $KV$ product greater than 55 $k_BT$ to ensure thermal stability over a 5 years period [23]. This conclusion, together with the fact that current head designs cannot generate more 800 kA/m of write field in the recording media, gives an estimation of 8 nm as the lower limit for the grain dimension [25] in the CoCr-based alloys currently used for hard disk drives [21].

A possible solution to the SPL is to replace the continuous medium, where the SPL applies to each of the grains, with a set of separated cells, so that the volume $V$ in Eq. (2.66) corresponds to the entire volume cell. Arrays with single-domain elements, also called bit-

patterned media, are a promising implementation of this idea. In these arrays the size of the elements is sufficiently large to avoid the superparamagnetic limit and at the same time sufficiently small to obtain large areal densities. The elements can be connected or isolated, and the best choice is still an open question. The properties of magnetic media manufactured with this approach can be tuned acting both on the characteristics of the magnetic material and on the shape of the single elements.

Concerning the size of the elements, to guarantee a sufficient areal density the dimensions should be between few tens and few hundreds of nanometres. This size is consistent with the current state-of-art for densities on commercial devices, now able to store up to 200 Gbit of data per square inch [26], with each bit cell covering an area of about 3200 $nm^2$.

### 2.9.2 MRAMs

One of the most promising applications of patterned media for magnetic recording is Magneto-resistive Random Access Memory (MRAM).

The simplest variant, sketched in Figure 2.16, is designed as an array of magnetic memory cells which are addressed by so called bit and word lines instead of the relative position on a track used in hard disk drives.

Each bit cell consists of a Magnetic Tunnel Junction (MTJ) obtained from a three layer (ferromagnetic metal - insulator - ferromagnetic metal) structure. The ferromagnetic layers, which act as electrodes, are made of soft and hard ferromagnetic materials. The soft magnetic layer, called free layer, is connected to the bit line and can have the magnetisation aligned or anti-aligned with the magnetisation of the hard layer. The latter, called fixed layer, is connected to the word line and when a current is flowing, via a tunnel effect, from the fixed layer to the free layer the resistance changes depending on the relative orientation of the magnetisation in the two layers.

This effect is called Tunnel Magneto-Resistance (TMR) [28], and the change in the resistance is used to distinguish between the Parallel (P) and the Anti-Parallel (AP) configuration, which are then used as physical states to encode the two logical states 0 and 1.

Rather than using a magnetic head like in hard disk drives, a bit is written applying a magnetic field on the soft layer through the application of a current both in the bit and word lines corresponding to the chosen cell. The applied field must be chosen in order to switch the soft layer but not the hard layer and dedicated solutions must be used to avoid the circulation of current through different (multiple) paths. The reading process uses a similar approach: a weaker current flows through the addressed bit and word lines and is used to measure the resistance of the cell, which is then converted in the logical 0 and 1.

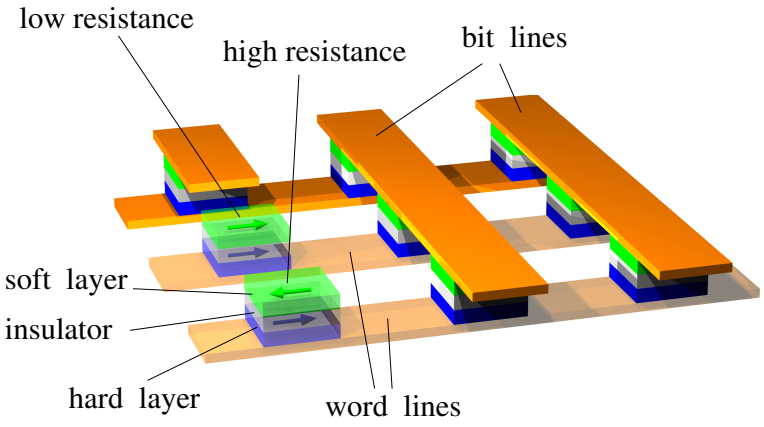


Figure 2.16: Working principle of MRAM cell (reproduction from [27]).

Commercial applications of these devices [29] use a free layer made of a synthetic antiferromagnet and the easy-axis of the free and hard layers is at 45° with respect to the directions of the word and bit lines [30, 31]. In this case the switching mechanism uses impulses of current in both the word and bit lines to "toggle" (thus the name Toggle-MRAM) the magnetisation in the free layer, and the switching can be described by the Stoner-Wohlfarth model.

The main advantage of MRAMs over hard disk drives is to have non-volatile storing of data without the use of any mechanical part in the device; on the other hand, two significant drawbacks characterising these devices are the presence of fringe fields near switching elements (also present in hard disk drives) and the need of two current directions to switch the magnetisation in the soft layer.

A possible solution to the two-directions current is the use of an improved designs able to use only one current direction to switch the soft layer between the two logical states, but the fringe fields problem can be addressed only avoiding the use of magnetic fields in the writing process or at least reducing the strength of the field.

The latter result can be achieved by using a thermally assisted technology where the free layer is brought near its Curie temperature so that the magnetisation requires a lower applied field to switch. The best solution is however to avoid the use of magnetic fields in the writing process, a result obtained by using the so-called spin-torque effect. This effect relies on the possibility to have the electrons angular momentum of a spin-polarised current to be transferred to the electrons of the ferromagnetic metal, thus controlling by an electric current the magnetisation switching in the ferromagnet.

At present the main practical problem of devices based on spin-torque transfer is the large current density required for the switching of the magnetisation. Therefore the design

of memory elements based on spin-torque effects is a very active research field and in the following chapters some numerical methods to study potential structures for spin-torque based MRAM devices are presented.

## 2.10 Summary

The discovery of magnetism is attributed to ancient Greeks, who noted the unique attractive properties of what today are called lodestones. Over the centuries these stones have been used in medicine and navigation, with one of the most important applications being the compass (as remarked at the opening ceremony of 2008 Olympic Games held in Beijing, China). A milestone in the study of their properties is represented by 'De Magnete' of William Gilbert, a treatise on the properties of magnetic materials known at the end of 1500 where he reported of other attractive properties of matter which are non-magnetic in origin, calling them electric.

Despite the thorough experimental description, Gilbert could not understand the intimate nature of such properties, and it took more than 200 years to have a significant development in the comprehension of these phenomena; as it happens many times in Physics, the sparkle came from a casual observations. The author was Hans Christian Ørsted, who noted the deflection of a magnetic needle placed nearby a wire fed by an electric current. This discovery prompted a series of technological innovations such as the telegraph, electric motor and dynamo, as well as important theoretical developments, and by 1873 Maxwell's equations marked the completion of the theory linking magnetism and electricity.

At the same time an exhaustive explanation of the properties of permanent magnets was still missing, and was Pierre Weiss in 1907 to put some light on the subject. He postulated the presence in magnetic materials of tiny permanent magnetic moments, and the existence of a molecular field responsible for the cooperative behaviour of these moments over microscopic regions.

The advent of quantum mechanics confirmed his ideas. One of the consequences of the new laws describing the microscopic world was that atoms are characterised by an orbital and spin angular momentum, with the latter being the main source of the magnetic properties in matter.

Depending on the interaction between the atomic moments, magnetic materials can be classified as diamagnetic, paramagnetic, ferromagnetic, antiferromagnetic or ferrimagnetic. For their weak magnetic properties all the non-ferromagnetic materials are often considered non magnetic, while the ferromagnetic ones are the most used as permanent or temporary magnets. They are typically characterised by three parameters, saturation magnetisation,

coercivity and remanent field, and the interaction between their atomic moments can be expressed by four energies (and associated fields): Zeeman energy, exchange energy, demagnetising energy and anisotropy energy.

The Zeeman energy is associated to an external field applied to a magnetic specimen, and its effect is to align the magnetisation in the sample along the direction of such a field.

The exchange energy has a pure quantum origin and is due to the overlapping wave functions of neighbour atoms. Its effect is to maintain aligned or anti-aligned the magnetic moments over extended, though microscopic, regions of a magnetic material and can be seen as the source of the molecular field postulated by Weiss.

The demagnetising energy is the effect of surface and volume magnetic charges which appear in a magnetic sample both at the interface between regions with different magnetisation direction and at the surface of the sample. Depending on the size of the sample, the demagnetising energy favours a curled magnetisation configuration or a configuration made of magnetic domains. The first case occurs when the specimen is comparable with the exchange length, a characteristic length defined by the balance between the exchange and demagnetising energy. Larger samples present magnetic domains while smaller ones can be treated as having a uniform magnetisation configuration, with their magnetic properties well described by the Stoner-Wohlfarth theory.

The anisotropy energy is associated to the tendency of the magnetisation to lie along certain directions. Magnetic anisotropy can have various origins, but the most important for the purpose of this thesis are magnetocrystalline anisotropy and shape anisotropy. The first one is due to the spin-orbit interaction between the electrons orbitals and the crystal lattice, while the second is a direct consequence of the demagnetising field, which favours a local alignment of the magnetisation with the surface of the material.

The theory which describes the balance between these energies at length scale between a few nanometers and some micrometers is called micromagnetism: it is based on the assumption of a continuous and differentiable magnetisation function and uses a local mean field approximation to describe the metastable configurations of a magnetic system. Such theory has been developed by William W.F. Brown and together with the work of Landau and Lifshitz on the time evolution of the magnetisation allows to reproduce experimental magnetic patterns and describe complex magnetic systems with high accuracy.

Because of the large number of variables involved, such theory is not appropriate for the description of magnetic applications like radio speakers, credit cards, magnetically levitated trains or particle accelerators, but it is giving a substantial contribution to the development of a technology with a strong impact on the society: data storage devices.

The vast majority of magnetic data storage devices are represented by hard disk drives, where a bit of information is physically represented by a so called bit cell. In each cell,

containing several magnetic grains in a 2D arrangement, the net remanent magnetisation of the grains along a given direction is encoded as the logical 0 and 1. With this design the amount of information that can be stored on a given device is controlled by the physical extension of each cell. To avoid noise in the medium the number of grains per cell has to be of the order of 50-100, and an increase in the density of information, corresponding to a reduction in the size of the cells, can be achieved only reducing the size of the grains.

The limits of this approach start to become apparent, since below a certain size the grains are subject to the SuperParamagnetic Limit (SPL), expressed by an energy barrier over which the remanent state is no more a stable state of the magnetisation, but it can reverse spontaneously due to the thermal energy of the system, with a consequent loss of the stored information. A possible solution to the SPL is to replace the continuous medium, where the SPL applies to each of the grains, with a set of separated single-domain elements, where the size is sufficiently large to avoid the superparamagnetic limit and at the same time sufficiently small to obtain large areal densities.

The most promising candidate for such media, also called bit-patterned media, is the MRAM. Commercial MRAM devices store information in cells made of a (ferromagnetic metal - insulator - ferromagnetic metal) tri-layer using the relative orientation of the magnetisation in two ferromagnetic metal layers. A current flowing via a tunnel effect in the insulator is at the base of the reading mechanism which, exploiting the Tunnel Magneto-Resistance (TMR) effect, uses the variation of intensity to distinguish the relative orientation of the magnetisation in the two layers.

Besides the reading process, in these devices an electric current can also be used to store information. The key of the storing mechanism is the spin-torque effect. This effect relies on the possibility to have the electrons angular momentum of a spin-polarised current to be transferred to the electrons of the ferromagnetic metal, thus controlling by an electric current the magnetisation switching in the ferromagnet. Such effect in existing MRAM designs requires large current densities, and improved designs requiring lower current densities are an active research field. In this thesis some numerical methods to study potential structures for spin-torque based MRAM devices are presented.

# Chapter 3

# Computational micromagnetics

## 3.1 Introduction

In many fields of physics the use of computer simulations has become a fundamental tool for a better understanding of experimental results and the comparison to theoretical predictions.

This is especially true in the field of micromagnetics, where the number of variables involved in a typical problem is very large (3N, with N being the number of atoms or cells in the specimen) [32] and analytical solutions are restricted to a very limited number of particular cases.

Despite the micromagnetic model being based on a mean field approximation, which in principle allows to discretise the problem without taking into account all the quantum effects occurring at the atomic scale, the investigation of micromagnetic systems using computational models requires a very fine discretisation of the specimen in order to satisfy one of the assumptions presented in Sec. 2.5: the magnetisation must be a smooth function over the domain of the magnetic body, so that Eq. (2.35) is a legitimate expression of the exchange energy.

Together with the domain, also the magnetisation vector and the equations associated to the various energy terms are discretised, and the main discretisation methods used in micromagnetic problems are finite differences and finite elements: for finite differences the cells are same-size cuboids over all the space, whereas for finite elements the cells are elements with arbitrary polyhedral shape on an irregular grid. In principle with the finite differences approach the constraint on the cells being of constant size could be dropped, a solution which however prevents the use of the efficient FFT techniques (explained in Sec. 3.2) in the computation of the demagnetising field.

This chapter describes how to use the finite differences method (FDM) and the finite element method (FEM) to solve the crucial point in any micromagnetic simulation, that

is the computation of the demagnetising field in the Poisson problem of Eq. (2.21). As the FEM is the principal technique used for the simulations in the rest of the thesis, a detailed description of the method is provided in Sec. 3.3, while for the FDM only a brief introduction is presented in Sec. 3.2. Concerning the FEM, the mathematical background is introduced first, and subsequently the Eq. (2.19)-(2.25) are expressed in their computational form. The derivation using the standard FEM is extensively described, and a brief discussion of the improvement achievable with the hybrid Finite Element/Boundary Element Method is presented. Sec. 3.4.3 presents the derivation of the computational form of the energies introduced in the previous chapter, and the chapter ends with the description of two numerical techniques for the integration of Eq. (2.65), the LLG equation.

## 3.2 The Finite Differences Method

The modelling of a micromagnetic system by the Finite Differences Method (FDM) requires to approximate the magnetisation over the magnetic body as a series of magnetisation vectors, one for each cuboid (also called discretisation cell): the vector is placed at the centre of the cell, with constant magnitude $M_s$ and direction correspondent to the average of the magnetisation over the cuboid. The result is a set of magnetisation vectors on a regular grid at a distance $d_i$ apart ($i = x, y, z$ for a 3D geometry) along the main axes of the space, where $d_i$ is constant over all the domain and chosen in order to satisfy the small-angles approximation between neighbour magnetisation vectors leading to Eq. (2.35). Such choice implies that $d_i$ must be smaller than the characteristic lengths of the material and a typical value for Permalloy ($M_s = 8 \cdot 10^5$ A/m, A=$13 \cdot 10^{-12}$ J/m), the magnetic material used for all the simulation in the rest of the thesis, is $d_i \leq 5$ nm. Once the simulation grid is defined, the Laplacian in Eq. (2.63) is approximated by finite differences quotients on the three main axis while for the computation of the demagnetising field the expression in Eq. (2.15) is used. This is possible because also the magnetisation evolution is discretised, with Eq. (2.65) being substituted by a finite differences expression according to one of the methods briefly described in Sec. 3.5.1. With this approach at each state the magnetisation $\mathbf{M}$ is treated as a constant over each cell, and the demagnetising field experienced by the dipole at the generic position $\mathbf{r}_{i,j,k}$ can be expressed as [33]

$$\mathbf{H}_{i,j,k} = -\sum_{l,m,n} \mathbf{N}(\mathbf{r}_{i,j,k} - \mathbf{r}_{l,m,n}) \cdot \mathbf{M}_{l,m,n} \tag{3.1}$$

where $\mathbf{N}$ is the demagnetising tensor of the cuboid. For a non-uniform magnetisation distribution such tensor depends on the distance on the simulation grid between the dipole at position $(i, j, k)$ and any other dipole at position $(l, m, n)$, thus making Eq. (3.1) a

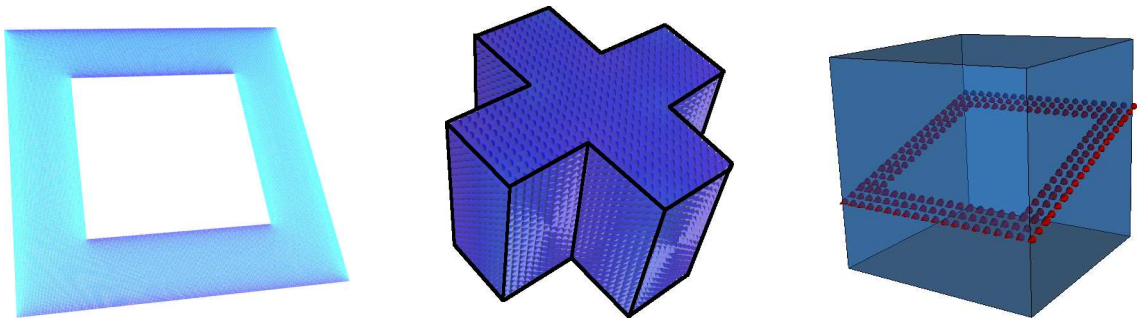

(**a**) (**b**) (**c**)

Figure 3.1: Prism-like geometries: (a) thin square ring, (b) thick cross and (c) hollow cube.

numerical convolution, and the computation of the field over all the space requires $n^2$ operations if the domain is divided in $n$ cells.

However the form of Eq. (3.1) can be exploited in the Fourier transformed space, where the convolution of $N$ and $M$ in the original space becomes a product of the two functions in the transformed one. The use of Fast Fourier Transform (FFT) algorithms allows to have a computation of Eq. (3.1) in the Fourier space which scales as $O(n \log n)$, although the usual constraints for the application of FFT must be satisfied [34]: the maximum sampling frequency of the function is limited by the discretisation of the domain and the number of cells in each direction must be a power of 2. Once the demagnetising field in the Fourier space is computed, its expression is inverted back in the real space. As the demagnetising tensor is a function of the geometry, the computation of the demagnetising factor is done only once at the beginning of the simulation, while for the magnetisation vectors the Fourier transformation and successive inversion is done at each step of the discretised time evolution.

As the FDM is based on a uniform domain discretisation, this approach is best suited to prism-like geometries such as those in Figure 3.1. For curved geometries the staircase approximation of the contours introduces spurious magnetic charges on the surface of the objects, which may affect the computation of the demagnetising field over all the space and eventually the magnetisation evolution in the system. Algorithms to reduce this effect are available [35, 36] but to our knowledge they are not implemented in public/commercial micromagnetic simulation codes.

One major advantage of the FDM over the FEM is the small memory requirement for the simulation of magnetic thin films. In fact using the pure FEM the memory requirements to compute the demagnetising field scale as $O(\mathcal{N}^2)$, with $\mathcal{N}$ being the number of nodes of the overall mesh, and using the hybrid Finite Element/Boundary Element

(FE/BE) Method (presented in Sec. 3.4.2) the memory requirements scale as $O(N^2)$ with $N$ now being the number of surface nodes of the unstructured mesh.

In the pure FEM the stiffness matrix is sparse, so that the memory footprint can be reduced with the use of specific compression methods, but also in the FE/BE case, characterised by a fully populated matrix, the memory footprint can be improved up to $O(N \log N)$ using methods which "approximate" the boundary element matrix. In this thesis, however, the results for large systems with a flat geometry (*e.g.* the connected rings array described in Chapter 7) are obtained using the FDM approach.

## 3.3 The Finite Element Method

The Finite Element Method (FEM) is a technique that allows to solve partial differential equations (PDE) in a numerical form without any constraint on their domain. This property is based on the discretisation of the computational domain in an unstructured mesh and the consequence is a superior accuracy of the method with respect to the finite differences. In each cell of the mesh the solution is approximated with polynomials whose coefficients are determined minimising the distance from the exact solution [37]. Minimisation is performed using a norm in a suitable vector space and the accuracy of the solution can be improved arbitrarily with an adaptive refinement of the mesh on the domain.

### 3.3.1 Discretisation of domain

The FEM is founded on two ideas. The first one is domain discretisation and consists of tiling the domain with small elements.

Given a PDE defined on a domain $\Omega$, the quality of the domain discretisation, or mesh, is related to the accuracy of the approximate solution of the PDE on $\Omega$. The quality of the mesh is usually assessed looking at the characteristics of the single elements, and takes into account their shape, size, number and similarity [38]. The local error is defined as $||u^i - u^i_{\text{int}}||$, with $u^i$ the exact solution of the partial differential equation on the element $i$ and $u^i_{\text{int}}$ the interpolated solution given by the FEM. The norm is defined as an integral over the individual elements and the error can be reduced with a refinement of the mesh. An example is shown in Figure 3.2, where the problem is defined on a 2D disc and the tiling is made with triangles.

Given the PDE and the domain of the problem, the placement of nodes is performed using application-specific algorithms, whose design is an active area of study because efficient algorithms for mesh modification (insertion and deletion of points) play a key role for mesh generating heuristics. In a typical discretisation the mesh is of high quality if the

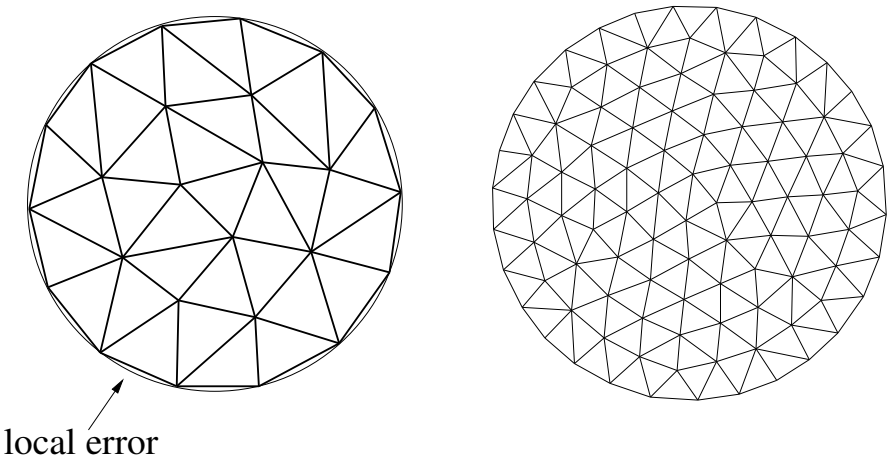


Figure 3.2: Mesh example: triangulation of a circle. The refinement decreases the local error $||u^i - u^i_{\text{int}}||$ between the real solution $u^i$ of the partial differential equation on the element $i$ and the interpolated solution $u^i_{\text{int}}$.

inner angles of the elements are far from 0 and $\pi$ radians, with the ideal value depending on element choice and dimensionality of space, and the shape of the elements is as regular as possible.

The placement phase is performed together with the triangulation phase, where the nodes are connected to create the domain tessellation. A widely used algorithm for this purpose is Delaunay triangulation, which is based on the projection of the nodes onto a higher dimensional convex hull and uses convexity properties to determine mesh connectivity.

Once the domain is meshed, the nodes are numbered in a way suitable for an efficient manipulation of the stiffness matrix. The stiffness matrix is assembled from the equations describing the solution of the PDE on the nodes of the mesh.

The result is a system of linear algebraic equations whose matrix is highly sparse as well as symmetric. Its derivation is explained in the next section.

### 3.3.2 Approximation of the function

The second element of FEM is the approximation of the PDE solution through a function defined on an element basis over the mesh. Usually this is done using polynomials, such that the global function $U(\mathbf{r})$, approximating the real solution of the PDE, is piecewise continuous over each element. The global function can then be expressed as [39]

$$U(\mathbf{r}) = \sum_{e=1}^{N} u^e(\mathbf{r}) \tag{3.2}$$

where $N$ is the number of elements and $u^e$ the approximation of the real PDE solution over the element $e$.

In this way the problem can be tackled in two steps: a trial solution of the problem is first defined through test functions on an element basis and then these individual test functions are merged over the entire space minimising the distance from the exact PDE solution.

As an example of the use of this technique let us assume to have a problem defined on the $x$-$y$ plane and to use triangular elements for the mesh. This is a typical application of FEM and the generalisation to higher dimensions requires few modifications to this scheme.

When we choose the degree of the polynomial for the local trial function $u^e(\mathbf{r})$ we have to take into account the degrees of freedom related to the single element. The degrees of freedom are defined as the number of nodes associated to each element and the polynomial must have as many free parameters as the number of these nodes.

If we decide to use first order elements, where the nodes of the mesh are associated with the vertices of the simplices, the lowest polynomial has degree 1 and can be expressed as

$$u^e(x, y) = p_1 + p_2 x + p_3 y \tag{3.3}$$

which can be written in a compact form as

$$u^e(x, y) = \begin{pmatrix} 1 & x & y \end{pmatrix} \begin{pmatrix} p_1 \\ p_2 \\ p_3 \end{pmatrix} \tag{3.4}$$

where $p_1$, $p_2$ and $p_3$ are the unknown coefficients to be found imposing the solution $U(\mathbf{r})$ on the entire space to be as close as possible to the exact solution of the problem. This problem is rather complicated when expressed in the global coordinates $x$ and $y$ but can be simplified using a local reference system [40].

With reference to Figure 3.3, taking $\xi = 1, 2, 3$ and defining $u^e_\xi = u^e(x_\xi, y_\xi)$ the function $u^e(\mathbf{r})$ on the nodes of the arbitrary triangle, we can use the Eq. (3.4) to write

$$\begin{pmatrix} u^e_1 \\ u^e_2 \\ u^e_3 \end{pmatrix} = \begin{pmatrix} 1 & x_1 & y_1 \\ 1 & x_2 & y_2 \\ 1 & x_3 & y_3 \end{pmatrix} \begin{pmatrix} p_1 \\ p_2 \\ p_3 \end{pmatrix} \tag{3.5}$$

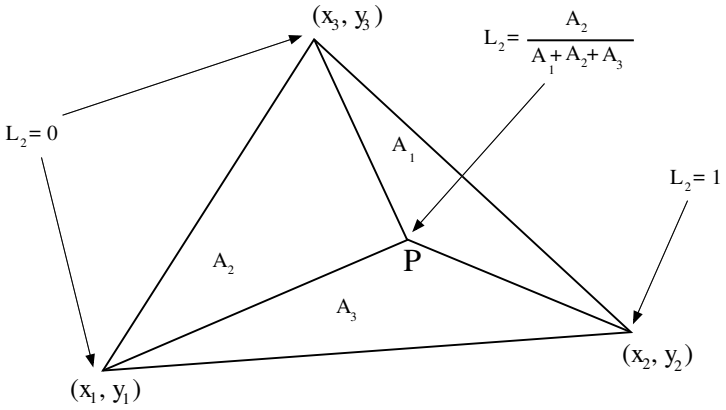


Figure 3.3: Mesh element in 2D. The coordinates of a point $P = P(x, y)$ are defined in the local reference system $(L_1, L_2, L_3)$, where $1, 2, 3$ are labels associated with the nodes of the triangle ($(x_1, y_1)$,$(x_2, y_2)$ and $(x_3, y_3)$ are node positions of the mesh). The coordinates $L_i$ are functions of the position $(x, y)$ inside each triangle and can be expressed as a proper ratio of the areas $A_1, A_2, A_3$ defined by the point $P$. As an example, $L_2$ is the ratio between the area $A_2$ and the total area $A_1 + A_2 + A_3$ of the triangle.

Solving this system for $p_1, p_2$ and $p_3$ and substituting into Eq. (3.4) we obtain

$$u^e(x, y) = \begin{pmatrix} 1 & x & y \end{pmatrix} \begin{pmatrix} 1 & x_1 & y_1 \\ 1 & x_2 & y_2 \\ 1 & x_3 & y_3 \end{pmatrix}^{-1} \begin{pmatrix} u_1^e \\ u_2^e \\ u_3^e \end{pmatrix} \tag{3.6}$$

Finally defining

$$\begin{pmatrix} L_1(x, y) & L_2(x, y) & L_3(x, y) \end{pmatrix} = \begin{pmatrix} 1 & x & y \end{pmatrix} \begin{pmatrix} 1 & x_1 & y_1 \\ 1 & x_2 & y_2 \\ 1 & x_3 & y_3 \end{pmatrix}^{-1} \tag{3.7}$$

and $L_\xi = L_\xi(x, y)$ for $\xi = 1, 2, 3$ we can write

$$u^e(x, y) = \begin{pmatrix} L_1 & L_2 & L_3 \end{pmatrix} \begin{pmatrix} u_1^e \\ u_2^e \\ u_3^e \end{pmatrix} = L_1 u_1^e + L_2 u_2^e + L_3 u_3^e \tag{3.8}$$

This equation is the solution $u^e(\mathbf{r})$ expressed by the same polynomial of Eq. (3.3) in the local coordinate system $(L_1, L_2, L_3)$, where the unknown coefficients are now the values of the solution at the nodes 1, 2 and 3. This transformation allows to simplify the

computation of $u^e(x,y)$ using the properties of the local coordinates $L_\xi$ for the calculation of the coefficients $u^e_\xi$ . These properties can be summarized as:

- the expression of $L_\xi$, $\xi = 1,2,3$ in terms of global coordinates is given by

$$L_\xi(x,y) = \frac{a_\xi + b_\xi x + c_\xi y}{2A} \tag{3.9}$$

with the variables $a_\xi$, $b_\xi$ and $c_\xi$, cycling on $\xi,\eta,\zeta = 1,2,3$, being

$$a_\xi = x_\eta y_\zeta - x_\zeta y_\eta \tag{3.10}$$
$$b_\xi = y_\eta - y_\zeta \tag{3.11}$$
$$c_\xi = x_\zeta - x_\eta \tag{3.12}$$

and the denominator is

$$2A = \begin{vmatrix} 1 & x_1 & y_1 \\ 1 & x_2 & y_2 \\ 1 & x_3 & y_3 \end{vmatrix} \tag{3.13}$$

- the inverse transformation, from local to global coordinates, is expressed by

$$x = \sum_{\xi=1}^{3} L_\xi x_\xi \tag{3.14}$$
$$y = \sum_{\xi=1}^{3} L_\xi y_\xi \tag{3.15}$$

- the $L_\xi$ are linear in $x$ and $y$ and satisfy the condition

$$L_\eta(x_\xi, y_\xi) = \delta_{\eta\,\xi} \qquad \eta,\xi = 1,2,3 \tag{3.16}$$

- they are related to each other by the condition

$$L_1 + L_2 + L_3 = 1 \qquad \forall\,(x,y) \tag{3.17}$$

- their integral over the element is given by

$$\int_{A_e} L_1^m\, L_2^n\, L_3^q \,\mathrm{d}A_e = \frac{2\,A\,m!\,n!\,q!}{(m+n+q+2)!} \tag{3.18}$$

Depending on the operators in the original PDE, the element equations $u^e(\mathbf{r})$ can be computed in various ways and a class of methods commonly applied in micromagnetic

systems is that of minimum residuals, which are based on the minimisation of a functional associated with the micromagnetic equations.

The norm is defined as the projection on a base of independent functions and the minimisation of the functional is performed setting this norm to zero.

The accuracy of the method depends on the properties of these projecting, or "weighting", functions and one of the most used is the Galerkin method.

### 3.3.3 Galerkin method

Let us consider the boundary value problem associated with a Poisson equation. This problem can be seen as the generalisation of Eq. (2.21) for the magnetic scalar potential in our micromagnetic description and can be expressed by

$$D\,U(\mathbf{r}) = f(\mathbf{r}) \qquad \mathbf{r} \in \Omega \tag{3.19}$$

where $D$ is a second order differential operator, which we will take to be $\nabla^2$ in the rest of the discussion and $f(\mathbf{r})$ is the function containing information about the specific problem on the domain $\Omega$ and its boundaries. Following the derivation presented in [41], in the FEM the solution $U(r)$ is approximated using Eq. (3.2) and the null contribution of every $u^e(\mathbf{r})$ outside the element $e$ leads to the decomposition of Eq. (3.19) on an element basis

$$D\,u^e(\mathbf{r}) = f^e(\mathbf{r}) \qquad \mathbf{r} \in \Omega^e \tag{3.20}$$

where $\Omega^e$ now represents the domain of a single element $e$. Eq. (3.8) allows to express the solution over each element as a linear interpolation of the function computed on the nodes and Eq. (3.16) reduces our problem to find solutions that satisfy

$$D\,L^e_\xi\,u^e_\xi = f^e_\xi \qquad \xi = 1 \ldots n \tag{3.21}$$

where $n$ is the number of nodes for each element $e$, $L^e_\xi = L^e_\xi(\mathbf{r})$ are the local coordinates and $u^e_\xi$ and $f_\xi$ are the values of the trial solution of the problem and the value of $f(r)$ in the node $\xi$ of the element $e$, respectively.

In order to use a variational approach to find the coefficients $u^e_\xi$ in Eq. (3.21), let us define the residual as

$$R(L^e_\xi) = G\,L^e_\xi - f^e_\xi \qquad \xi = 1 \ldots n \tag{3.22}$$

where $G$ is the operator $u^e_\xi\,D$. If now we compare this functional with Eq. (3.21), we can see the latter as the solution of a minimisation problem.

With the method of weighted residuals the minimisation is done over an arbitrary set

of independent functions, and the Galerkin method simplifies the matter by taking the same functions $L_\xi^e$ as the weighting functions. Therefore the minimisation is expressed by

$$\int_{\Omega^e} R(L^e)\, L_\xi^e \,\mathrm{d}\omega = 0 \qquad \xi = 1 \ldots n \tag{3.23}$$

$$\int_{\Omega^e} \big(G\, L_\xi^e\big) L_\xi^e \,\mathrm{d}\omega = \int_{\Omega^e} f_\xi^e L_\xi^e \,\mathrm{d}\omega \tag{3.24}$$

$$\int_{\Omega^e} u_\xi^e \big(D\, L_\xi^e\big) L_\xi^e \,\mathrm{d}\omega = \int_{\Omega^e} f_\xi^e L_\xi^e \,\mathrm{d}\omega \tag{3.25}$$

where the set of equations in Eq. (3.25) is used to build the stiffness matrix and compute the unknowns $u_\xi^e$. Finally the approximated solution over all the domain $\Omega$ is given by

$$U(\mathbf{r}) = \sum_{e=1}^{N} u^e(\mathbf{r}) \qquad \mathbf{r} \in \Omega \tag{3.26}$$

$$= \sum_{e=1}^{N} \sum_{\xi=1}^{n} u_\xi^e \, L_\xi^e(\mathbf{r}) \tag{3.27}$$

## 3.4 Computation of the demagnetising field

Now that we have introduced the concepts of the FEM, we are able to compute the demagnetising field in our computational model. To fit with real applications its description will be done generalising in 3D the concepts introduced in Sec. 3.3.2 for the 2D case.

In the previous chapter we have seen how the demagnetising field is created by the magnetisation of the material. Its origin is expressed by Eq. (2.20), where $\mathbf{M}(\mathbf{r})$ is a magnetisation distribution and $\mathbf{H}_{\mathrm{dem}}(\mathbf{r})$ the unknown field used in Eq. (2.13) to compute the demagnetising energy. The introduction of a scalar potential $U_{\mathrm{dem}}(\mathbf{r})$ allows to reduce the problem of the calculation of $\mathbf{H}_{\mathrm{dem}}(\mathbf{r})$ to the Poisson equation (Eq. (2.21)) with the boundary conditions expressed by Eq. (2.23) - (2.25).

In Sec. 3.3.3 we have seen how the variational approach can be used to find the solution of the Poisson problem. In that case the information about the boundary conditions of the problem were implicit in the function f($\mathbf{r}$) but in the present case their treatment requires a separate analysis. In fact the potential $U_{\mathrm{dem}}(\mathbf{r})$ is defined over all the space and in computer simulations there are two ways to deal with the value of the magnetic potential at infinity: extending the meshed region well beyond the magnetic objects in the empty space and adopting the standard FEM, or using a mesh which covers only the magnetic objects and adopting the Boundary Element Method (BEM). The first approach, adapted from [42] and [43] to the 3D case, is explained in detail in the following section, while the second approach is presented in Sec. 3.4.2.

### 3.4.1 Standard FEM approach

With the standard FEM approach the magnetic region and its boundary are enclosed in the numerical model and the potential is set to zero on the outer model boundary. Therefore Eq. (2.25) becomes

$$U_{\mathrm{dem}}(\mathbf{r}) = 0 \qquad \forall \mathbf{r} \in \partial\Omega \tag{3.28}$$

and we can apply the Galerkin method to approximate the potential $U_{\mathrm{dem}}(\mathbf{r})$ on the domain. The residual Eq. (3.22) is therefore defined as

$$R(\mathbf{r}) = \nabla^2 U_{\mathrm{dem}}(\mathbf{r}) - \nabla \cdot \mathbf{M}(\mathbf{r}) \tag{3.29}$$

where, calling $U(\mathbf{r}) \equiv U_{\mathrm{dem}}(\mathbf{r})$, we have

$$U(\mathbf{r}) = \sum_{e=1}^{N} u^e(\mathbf{r}) \tag{3.30}$$

$$= \sum_{e=1}^{N} \sum_{\xi=1}^{n} L_\xi^e \, u_\xi^{\mathbf{e}} \tag{3.31}$$

and

$$\mathbf{M}(\mathbf{r}) = \sum_{e=1}^{N} \mathbf{m}^e(\mathbf{r}) \tag{3.32}$$

$$= \sum_{e=1}^{N} \sum_{\xi=1}^{n} L_\xi^e \, \mathbf{m}_\xi^e \tag{3.33}$$

where $n$ is the number of nodes for each element $e$ and $L_\xi^e = L_\xi^e(\mathbf{r})$ are the local coordinates. In this coordinate system $u_\xi^e$ is the solution of the problem in the node $\xi$ of the element $e$ and $\mathbf{m}_\xi^e$ the corresponding magnetisation.

The minimisation in Eq. (3.23) is then expressed by

$$\int_V \Big( \nabla^2 U(\mathbf{r}) - \nabla \cdot \mathbf{M}(\mathbf{r}) \Big) L_\eta \, \mathrm{d}V = 0 \qquad \eta = 1 \ldots m \tag{3.34}$$

where $m$ is the number of nodes of the entire mesh. This expression can be rewritten as

$$\int_V L_\eta \nabla^2 U(\mathbf{r}) \, \mathrm{d}V = \int_V L_\eta \Big( \nabla \cdot \mathbf{M}(\mathbf{r}) \Big) \, \mathrm{d}V \qquad \eta = 1 \ldots m \tag{3.35}$$

and for its solution we use Green's theorem with the boundary condition Eq. (2.24).

Suppose that $\phi(\mathbf{r})$ is a $l^2$ function defined on a domain $\Omega$ and $\psi(\mathbf{r})$ is $l^1$ on the same domain. One of the forms of Green's theorem [44] states

$$\int_{\Omega}\left(\psi(\mathbf{r})\,\nabla^2\phi(\mathbf{r})\right)\,\mathrm{d}\omega = \oint_{\partial\Omega}\left(\psi(\mathbf{r})\frac{\partial\phi(\mathbf{r})}{\partial\hat{\mathbf{n}}}\right)\,\mathrm{d}\sigma - \int_{\Omega}\left(\nabla\phi(\mathbf{r})\cdot\nabla\psi(\mathbf{r})\right)\,\mathrm{d}\omega \tag{3.36}$$

and substituting $\psi(\mathbf{r})$ with $L_\eta$ and $\phi(\mathbf{r})$ with $U(\mathbf{r})$, its application to the inner and outer region of the magnetic domain $V$ gives

$$\begin{cases} \int_{V_i} L_\eta\nabla^2 U_i(\mathbf{r})\,\mathrm{d}V_i = \oint_{\partial V_i}\left(L_\eta\frac{\partial U_i(\mathbf{r})}{\partial\hat{\mathbf{n}}}\right)\,\mathrm{d}S - \int_{V_i}\left(\nabla U_i(\mathbf{r})\cdot\nabla L_\eta\right)\,\mathrm{d}V_i \\ \int_{V_o} L_\eta\nabla^2 U_o(\mathbf{r})\,\mathrm{d}V_o = -\oint_{\partial V_i}\left(L_\eta\frac{\partial U_o(\mathbf{r})}{\partial\hat{\mathbf{n}}}\right)\,\mathrm{d}S - \int_{V_o}\left(\nabla U_o(\mathbf{r})\cdot\nabla L_\eta\right)\,\mathrm{d}V_o \qquad \eta = 1\ldots m \end{cases} \tag{3.37}$$

where $U_i$ and $U_o$ are the solutions in the inner and outer regions, respectively, and the sign of the integral on the surface is taken considering a clockwise path. From Eq. (3.35) we can also write

$$\begin{cases} \int_{V_i} L_\eta\nabla^2 U_i(\mathbf{r})\,\mathrm{d}V_i = \int_{V_i} L_\eta\Big(\nabla\cdot\mathbf{M}(\mathbf{r})\Big)\,\mathrm{d}V_i \\ \int_{V_o} L_\eta\nabla^2 U_o(\mathbf{r})\,\mathrm{d}V_o = 0 \qquad\qquad \eta = 1\ldots m \end{cases} \tag{3.38}$$

and applying Eq. (2.24) after combining Eq. (3.37) and (3.38) we have

$$\int_{V_i} L_\eta\Big(\nabla\cdot\mathbf{M}(\mathbf{r})\Big)\,\mathrm{d}V_i = \oint_{\partial V_i} L_\eta\left(\frac{\partial U_i(\mathbf{r})}{\partial\hat{\mathbf{n}}} - \frac{\partial U_o(\mathbf{r})}{\partial\hat{\mathbf{n}}}\right)\,\mathrm{d}S - \int_{V}\left(\nabla U(\mathbf{r})\cdot\nabla L_\eta\right)\,\mathrm{d}V \tag{3.39}$$

$$= \oint_{\partial V_i} L_\eta\Big(\mathbf{M}(\mathbf{r})\cdot\hat{\mathbf{n}}\Big)\,\mathrm{d}S - \int_{V}\left(\nabla U(\mathbf{r})\cdot\nabla L_\eta\right)\,\mathrm{d}V \tag{3.40}$$

so that

$$\int_{V}\left(\nabla U(\mathbf{r})\cdot\nabla L_\eta\right)\,\mathrm{d}V = -\int_{V_i} L_\eta\Big(\nabla\cdot\mathbf{M}(\mathbf{r})\Big)\,\mathrm{d}V_i + \oint_{\partial V_i} L_\eta\Big(\mathbf{M}(\mathbf{r})\cdot\hat{\mathbf{n}}\Big)\,\mathrm{d}S \tag{3.41}$$

This equation can now be expressed in a matrix form. The left-hand-side rewritten on an element basis has the form

$$\int_{V}\left(\nabla U(\mathbf{r})\cdot\nabla L_\eta\right)\,\mathrm{d}V = \sum_{e=1}^{N}\int_{V^e}\left(\nabla u^e(\mathbf{r})\cdot\nabla L_\eta^e\right)\,\mathrm{d}V^e \tag{3.42}$$

and for each of the elements we can write

$$\int_{V^e} \left( \nabla u^e(\mathbf{r}) \cdot \nabla L^e_\zeta \right) \mathrm{d}V^e \overset{(3.31)}{=} \int_{V^e} \left( \nabla \sum_{\xi=1}^{n} L^e_\xi \, u^e_\xi \cdot \nabla L^e_\zeta \right) \mathrm{d}V^e \; \zeta = 1 \ldots n \quad (3.43)$$

$$= \sum_{\xi=1}^{n} \int_{V^e} \left( \nabla L^e_\xi \cdot \nabla L^e_\zeta \right) u^e_\xi \, \mathrm{d}V^e \; \zeta = 1 \ldots n \quad (3.44)$$

where $n$ is the number of nodes of the element. Therefore calling

$$k^e_{i,j} = \int_{V^e} \left( \nabla L^e_i \cdot \nabla L^e_j \right) \mathrm{d}V^e \quad (3.45)$$

the equation Eq. (3.41) can be written as

$$\mathbf{K}\, U = \bar{\mathbf{F}} + \widetilde{\mathbf{F}} \quad (3.46)$$

where, using a definition taken from structural mechanics, $\mathbf{K}$ is the stiffness matrix, the expression $\bar{\mathbf{F}} + \widetilde{\mathbf{F}}$ represents the two terms of the force vector and $U$ is the vector of solutions $u_i$, $i = 1, \ldots, m$ where $m$ is the number of nodes of the mesh. Before going on to derive the expressions of the volume contribution $\bar{\mathbf{F}}$ and the surface contribution $\widetilde{\mathbf{F}}$ to the force vector on the right-hand side of Eq. (3.41), we can express the local coordinates $L^e_i$ in the 3D case and use their properties to rewrite the expression for $k^e_{i,j}$.

Using tetrahedra as mesh elements, the number of nodes per element is $n = 4$ and the expression of $L^e_i$ can be derived from the generalisation of Eq. (3.14), (3.15) and (3.17)

$$\begin{pmatrix} 1 \\ x \\ y \\ z \end{pmatrix} = \begin{pmatrix} 1 & 1 & 1 & 1 \\ x_1 & x_2 & x_3 & x_4 \\ y_1 & y_2 & y_3 & y_4 \\ z_1 & z_2 & z_3 & z_4 \end{pmatrix} \begin{pmatrix} L_1 \\ L_2 \\ L_3 \\ L_4 \end{pmatrix} \quad (3.47)$$

$$\begin{pmatrix} 1 & 1 & 1 & 1 \\ x_1 & x_2 & x_3 & x_4 \\ y_1 & y_2 & y_3 & y_4 \\ z_1 & z_2 & z_3 & z_4 \end{pmatrix}^{-1} \begin{pmatrix} 1 \\ x \\ y \\ z \end{pmatrix} = \begin{pmatrix} L_1 \\ L_2 \\ L_3 \\ L_4 \end{pmatrix} \quad (3.48)$$

$$\begin{pmatrix} a_1 & b_1 & c_1 & d_1 \\ a_2 & b_2 & c_2 & d_2 \\ a_3 & b_3 & c_3 & d_3 \\ a_4 & b_4 & c_4 & d_4 \end{pmatrix} \begin{pmatrix} 1 \\ x \\ y \\ z \end{pmatrix} = \begin{pmatrix} L_1 \\ L_2 \\ L_3 \\ L_4 \end{pmatrix} \quad (3.49)$$

and for $i = 1 \ldots 4$ the result is

$$L_i^e(x, y, z) = \frac{a_i^e + b_i^e x + c_i^e y + d_i^e z}{6V^e} \tag{3.50}$$

where

$$6V^e = \begin{vmatrix} 1 & 1 & 1 & 1 \\ x_1 & x_2 & x_3 & x_4 \\ y_1 & y_2 & y_3 & y_4 \\ z_1 & z_2 & z_3 & z_4 \end{vmatrix} \tag{3.51}$$

and

$$\begin{aligned} a_i^e &= \begin{vmatrix} x_j & y_j & z_j \\ x_k & y_k & z_k \\ x_l & y_l & z_l \end{vmatrix} & b_i^e &= \begin{vmatrix} 1 & y_j & z_j \\ 1 & y_k & z_k \\ 1 & y_l & z_l \end{vmatrix} \\ c_i^e &= \begin{vmatrix} x_j & 1 & z_j \\ x_k & 1 & z_k \\ x_l & 1 & z_l \end{vmatrix} & d_i^e &= \begin{vmatrix} x_j & y_j & 1 \\ x_k & y_k & 1 \\ x_l & y_l & 1 \end{vmatrix} \end{aligned} \tag{3.52}$$

With these definitions Eq. (3.45) becomes

$$k_{i,j}^e = \frac{b_i^e b_j^e + c_i^e c_j^e + d_i^e d_j^e}{36V^e} \tag{3.53}$$

The analysis of the right-hand side of Eq. (3.41), (3.46) requires separate derivations for the two terms. The volume contribution $\bar{\mathbf{F}}$ rewritten on an element basis is expressed by

$$-\int_{V_i} L_\eta \Big( \nabla \cdot \mathbf{M}(\mathbf{r}) \Big) \, \mathrm{d}V_i = -\sum_{e=1}^{N} \int_{V^e} L_\eta^e \Big( \nabla \cdot \mathbf{m}^e(\mathbf{r}) \Big) \, \mathrm{d}V \tag{3.54}$$

and, calling $\mathbf{m}_\xi^e$ the magnetisation at node $\xi$ of element $e$, for each element we can write

$$-\int_{V^e} L_\eta^e \Big( \nabla \cdot \mathbf{m}^e(\mathbf{r}) \Big) \, \mathrm{d}V^e \overset{(3.33)}{=} -\int_{V^e} L_\eta^e \Big( \nabla \cdot \Big( \sum_{\xi=1}^{4} L_\xi^e \, \mathbf{m}_\xi^e \Big) \Big) \, \mathrm{d}V^e \tag{3.55}$$

$$= -\int_{V^e} L_\eta^e \Big( \sum_{\xi=1}^{4} \Big( \nabla \cdot L_\xi^e \Big) \, \mathbf{m}_\xi^e \Big) \, \mathrm{d}V^e \tag{3.56}$$

$$\tag{3.57}$$

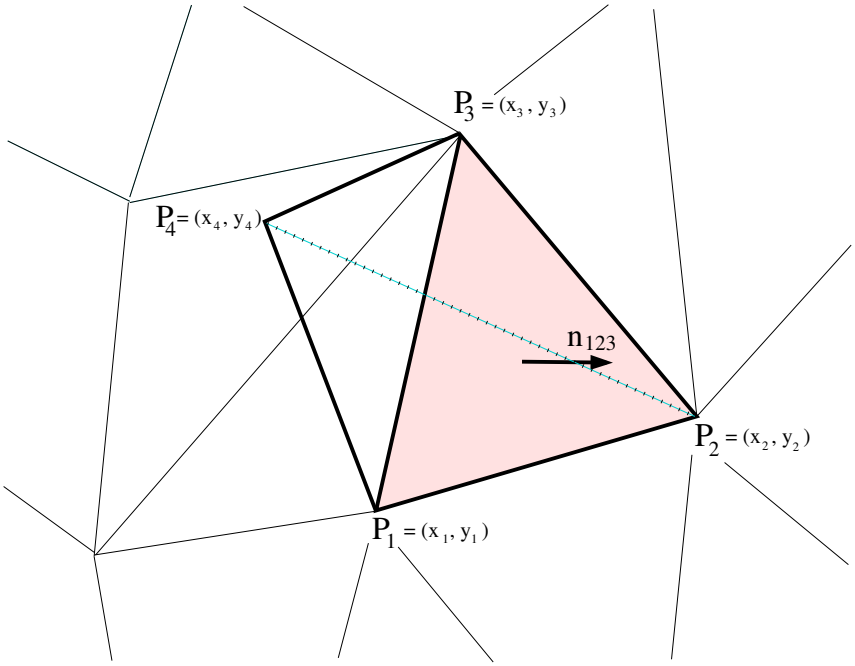


Figure 3.4: Boundary element: outer normal to a boundary surface.

$$\overset{(3.50)}{=} \quad -\frac{1}{6V^e}\sum_{\xi=1}^{4}\left(\begin{pmatrix} b_\eta^e \\ c_\eta^e \\ d_\eta^e \end{pmatrix}\cdot \mathbf{m}_\xi^e\right)\int_{V^e} L_\eta^e \,\mathrm{d}V^e \tag{3.58}$$

$$= \quad -\frac{1}{24}\sum_{\eta=1}^{4}\left(m_{\eta,x}^e\, b_\eta^e + m_{\eta,y}^e\, c_\eta^e + m_{\eta,z}^e\, d_\eta^e\right) \tag{3.59}$$

where the expression of the integral in Eq. (3.58) is computed using the integral formula for the 3D case

$$\int_{V_e} L_1^m\, L_2^n\, L_3^p\, L_4^q \,\mathrm{d}V = \frac{6\, V_e\, m!\, n!\, p!\, q!}{(m+n+p+q+3)!} \tag{3.60}$$

For the surface contribution $\widetilde{\mathbf{F}}$ we have to consider only the elements that lie on the boundary of the magnetic region and among these elements only the nodes that share a face with an element in the outer region. Referring to Figure 3.4, let us assume that the surface integral involves the face whose nodes are $\mathbf{p}_1 = (x_1, y_1, z_1), \mathbf{p}_2 = (x_2, y_2, z_2)$, and $\mathbf{p}_3 = (x_3, y_3, z_3)$. Using the property of the cross product the area $A_{1,2,3}$ of this surface is

$$A_{1,2,3} = \frac{1}{2}|(\mathbf{p}_3 - \mathbf{p}_1) \times (\mathbf{p}_2 - \mathbf{p}_1)| \tag{3.61}$$

and its outward unit normal is defined by

$$\hat{\mathbf{n}}_{1,2,3} = \frac{(\mathbf{p}_3 - \mathbf{p}_1) \times (\mathbf{p}_2 - \mathbf{p}_1)}{|(\mathbf{p}_3 - \mathbf{p}_1) \times (\mathbf{p}_2 - \mathbf{p}_1)|} \tag{3.62}$$

$$\overset{(3.52)}{=} \frac{\Big( - b_4^e, -c_4^e, -d_4^e \Big)}{|(\mathbf{p}_3 - \mathbf{p}_1) \times (\mathbf{p}_2 - \mathbf{p}_1)|} \tag{3.63}$$

On this face $L_4 = 0$ and generalising Eq. (3.17) to the 3D case $L_1 = 1 - L_2 - L_3$, so using Eq. (3.47) a generic vector $\mathbf{p}$ expressed in the local coordinate system can be written as

$$\mathbf{p} = (p_x, p_y, p_z) \tag{3.64}$$

$$= \Big( x_1 L_1 + x_2 L_2 + x_3 L_3, \; y_1 L_1 + y_2 L_2 + y_3 L_3, \; z_1 L_1 + z_2 L_2 + z_3 L_3 \Big) \tag{3.65}$$

$$= \Big( x_1 + (x_2 - x_1) L_2 + (x_3 - x_1) L_3, \; y_1 + (y_2 - y_1) L_2 + (y_3 - y_1) L_3, \; z_1 + (z_2 - z_1) L_2 + (z_3 - z_1) L_3 \Big) \tag{3.66}$$

and the infinitesimal quantity $\mathrm{d}\mathbf{p}$ can be rewritten as

$$\mathrm{d}\mathbf{p} = \frac{\partial \mathbf{p}}{\partial L_2} \mathrm{d}L_2 + \frac{\partial \mathbf{p}}{\partial L_3} \mathrm{d}L_3 \tag{3.67}$$

$$= \Big( x_2 - x_1, y_2 - y_1, z_2 - z_1 \Big) \mathrm{d}L_2 + \Big( x_3 - x_1, y_3 - y_1, z_3 - z_1 \Big) \mathrm{d}L_3 \tag{3.68}$$

$$= \Big( \mathbf{p}_2 - \mathbf{p}_1 \Big) \mathrm{d}L_2 + \Big( \mathbf{p}_3 - \mathbf{p}_1 \Big) \mathrm{d}L_3 \tag{3.69}$$

For the generalisation of Eq. (3.16) to the 3D case and the linearity of the interpolation functions $L_i$ we have $L_2 = 0$ along the vector $(\mathbf{p}_3 - \mathbf{p}_1)$ and $L_3 = 0$ along the vector $(\mathbf{p}_2 - \mathbf{p}_1)$. Therefore the infinitesimal area can be written as

$$\mathrm{d}A_{1,2,3} = |\mathbf{J}| \, \mathrm{d}L_2 \, \mathrm{d}L_3 \tag{3.70}$$

$$= \Big| (\mathbf{p}_3 - \mathbf{p}_1) \times (\mathbf{p}_2 - \mathbf{p}_1) \Big| \mathrm{d}L_2 \, \mathrm{d}L_3 \tag{3.71}$$

where $\mathbf{J}$ is the Jacobian of the linear transformation from $(x, y)$ coordinates to $(L_2, L_3)$ coordinates and the integration is done with $L_3$ going from 0 to 1 and $L_2$ from 0 to $1 - L_3$, for consistency with Eq. (3.61).

Now we have all the elements to derive the computational expression for the surface

term $\widetilde{\mathbf{F}}$ of the force vector. Rewriting the surface contribution on the right-hand side of Eq. (3.41) on an element basis we have

$$\oint_{\partial V_i} L_\eta \Big( \mathbf{M}(\mathbf{r}) \cdot \hat{\mathbf{n}} \Big) \, \mathrm{d}S = \sum_{e=1}^{N} \oint_{\partial V^e} L_\eta \Big( \mathbf{m}^e(\mathbf{r}) \cdot \hat{\mathbf{n}} \Big) \, \mathrm{d}S^e \tag{3.72}$$

where the sum is limited to the elements with a face in common with the outer region and the integral is performed on these faces.

Assuming that the generic element in this sum is represented by the element in Figure 3.4, we have

$$\oint_{\partial V^e} L_\eta \Big( \mathbf{m}^e(\mathbf{r}) \cdot \hat{\mathbf{n}} \Big) \, \mathrm{d}S^e = \oint_{A_{1,2,3}} L^e_\eta \Big( \mathbf{m}^e(\mathbf{r}) \cdot \hat{\mathbf{n}}_{1,2,3} \Big) \, \mathrm{d}A_{1,2,3} \tag{3.73}$$

and from Eq. (3.63) and (3.71) we can write

$$\oint_{A_{1,2,3}} L^e_\eta \Big( \mathbf{m}^e(\mathbf{r}) \cdot \hat{\mathbf{n}}_{1,2,3} \Big) \, \mathrm{d}A_{1,2,3} \;=\; -\int_0^1 \int_0^{1-L^e_3} L^e_\eta \Big( \sum_{\xi=1}^{3} L^e_\xi \, \mathbf{m}^e_\xi \Big) \begin{pmatrix} b^e_4 \\ c^e_4 \\ d^e_4 \end{pmatrix} \mathrm{d}L^e_2 \mathrm{d}L^e_3 \tag{3.74}$$

Remembering that $\mathbf{m}^e_\xi$ is the magnetisation at node $\xi$ of element $e$, the expression for node $\mathbf{p}_2$ is

$$\oint_{A_{1,2,3}} L^e_2 \Big( \mathbf{m}^e(\mathbf{r}) \cdot \hat{\mathbf{n}}_{1,2,3} \Big) \, \mathrm{d}A_{1,2,3} \;=\; -\int_0^1 \int_0^{1-L^e_3} L^e_2 \Big( \sum_{\xi=1}^{3} L^e_\xi \, \mathbf{m}^e_\xi \Big) \begin{pmatrix} b^e_4 \\ c^e_4 \\ d^e_4 \end{pmatrix} \mathrm{d}L^e_2 \mathrm{d}L^e_3 \tag{3.75}$$

$$\begin{aligned} &= -\int_0^1 \int_0^{1-L^e_3} L^e_2 \Big[ b^e_4 \Big( m^e_{1,x} \, L^e_1 + m^e_{2,x} \, L^e_2 + m^e_{3,x} \, L^e_3 \Big) + \\ &\quad c^e_4 \Big( m^e_{1,y} \, L^e_1 + m^e_{2,y} \, L^e_2 + m^e_{3,y} \, L^e_3 \Big) + \\ &\quad d^e_4 \Big( m^e_{1,z} \, L^e_1 + m^e_{2,z} \, L^e_2 + m^e_{3,z} \, L^e_3 \Big) \Big] \mathrm{d}L^e_2 \mathrm{d}L^e_3 \end{aligned} \tag{3.76}$$

$$\begin{aligned} &= -\frac{1}{24} \Big[ b^e_4 \Big( m^e_{1,x} + 2m^e_{2,x} + m^e_{3,x} \Big) + \\ &\quad c^e_4 \Big( m^e_{1,y} + 2m^e_{2,y} + m^e_{3,y} \Big) + \\ &\quad d^e_4 \Big( m^e_{1,z} + 2m^e_{2,z} + m^e_{3,z} \Big) \Big] \end{aligned} \tag{3.77}$$

For the nodes $\mathbf{p}_1$ and $\mathbf{p}_3$ we have respectively

$$\oint_{A_{1,2,3}} L_1^e\Big(\mathbf{m}^e(\mathbf{r})\cdot\hat{\mathbf{n}}_{1,2,3}\Big)\,\mathrm{d}A_{1,2,3} = -\frac{1}{24}\Big[b_4^e\Big(2m_{1,x}^e+m_{2,x}^e+m_{3,x}^e\Big)+ c_4^e\Big(2m_{1,y}^e+m_{2,y}^e+m_{3,y}^e\Big)+ d_4^e\Big(2m_{1,z}^e+m_{2,z}^e+m_{3,z}^e\Big)\Big] \tag{3.78}$$

$$\tag{3.79}$$

$$\oint_{A_{1,2,3}} L_3^e\Big(\mathbf{m}^e(\mathbf{r})\cdot\hat{\mathbf{n}}_{1,2,3}\Big)\,\mathrm{d}A_{1,2,3} = -\frac{1}{24}\Big[b_4^e\Big(m_{1,x}^e+m_{2,x}^e+2m_{3,x}^e\Big)+ c_4^e\Big(m_{1,y}^e+m_{2,y}^e+2m_{3,y}^e\Big)+ d_4^e\Big(m_{1,z}^e+m_{2,z}^e+2m_{3,z}^e\Big)\Big] \tag{3.80}$$

In the end of all this procedure we have the solution of the scalar potential expressed as the solution of the linear algebraic system

$$k_{i,j}u_j = \bar{f}_j + \widetilde{f}_j \tag{3.81}$$

where $i$ and $j$ run over the nodes of the mesh and the entries of $\mathbf{K}$ are different from 0 only if the nodes $i$ and $j$ are connected. The surface contribution expressed by the term $\widetilde{f}_j$ is limited to the nodes on the surface of the magnetic domain while the volume contribution expressed by $\bar{f}_j$ has effect within this region. In both cases the total contribution is computed summing up the contributions from all the elements connected to the specific node and at the boundaries of our model the potential is set to 0.

Having shown how the scalar potential can be computed, the expression for the demagnetising field is derived computing the gradient of $U_{\mathrm{dem}}(\mathbf{r})$ on an element basis using its values on the nodes

$$\mathbf{H}_{\mathrm{dem}}(\mathbf{r}) = -\nabla U_{\mathrm{dem}}(\mathbf{r}) \tag{3.82}$$

$$\overset{(3.31)}{=} -\nabla\sum_{e=1}^{N}\sum_{\eta=1}^{4} L_\eta^e u_\eta^e \tag{3.83}$$

$$= -\sum_{e=1}^{N}\sum_{\eta=1}^{4} u_\eta^e \nabla L_\eta^e \tag{3.84}$$

$$\overset{(3.50)}{=} -\sum_{e=1}^{N}\sum_{\eta=1}^{4} \frac{u_\eta^e}{6V^e}\Big(b_\eta^e\,,c_\eta^e\,,d_\eta^e\Big) \tag{3.85}$$

### 3.4.2 Finite Element/Boundary Element Method

The Boundary Element Method (BEM) is a numerical approach for the solution of boundary value problems which makes use of integral equations rather than partial differential equations as in the FEM. In micromagnetic problems the main strength of this approach is the solution of a field problem by solving an equivalent source problem, so that open regions can be treated without truncation of the empty space as in the pure FEM approach. In more detail, with a hybrid use of the BEM, the magnetic scalar potential of Eq. (2.19) can be calculated over all the space using only the mesh elements within the magnetic region. This method, proposed by Fredkin and Koehler [45], solves Eq. (2.21) by splitting the problem in two parts. Calling $\hat{\mathbf{n}}$ the unit outward normal to the surface of the magnetic body(ies), a solution $U_1$ is first found in the interior of the magnetic body(ies) using the standard FEM. This is done imposing

$$\nabla^2 U_1(\mathbf{r}) = \nabla \cdot \mathbf{M}(\mathbf{r}) \tag{3.86}$$

with Von Neumann boundary condition

$$\frac{\partial U_1(\mathbf{r})}{\partial \hat{\mathbf{n}}} = \mathbf{M}(\mathbf{r}) \cdot \hat{\mathbf{n}} \tag{3.87}$$

and assuming $U_1(\mathbf{r}) = 0$ in the outer space. This is equivalent to have a fictitious dipole layer on the surface of the magnetic body(ies), which will be compensated by an "anti-dipole" layer introduced artificially. The latter can be regarded as the source of the magnetic field needed to apply the BEM, and the second part of the problem is then to compute the magnetic potential $U_2$, defined such that

$$U_{\mathrm{dem}}(\mathbf{r}) = U_1(\mathbf{r}) + U_2(\mathbf{r}) \tag{3.88}$$

using the Boundary Element Method. From Eq. (2.21), (3.86) and (3.88) we have

$$\nabla^2 U_2(\mathbf{r}) = 0 \tag{3.89}$$

and the Dirichlet boundary conditions are set at infinity and on the surface $\partial R$ of the magnetic body(ies) with

$$U_2(\mathbf{r}) \longrightarrow 0 \quad \text{for} \quad |\mathbf{r}| \longrightarrow \infty \tag{3.90}$$

and by the expression

$$U_2(\mathbf{r}) = \int_{\partial R} U_1(\mathbf{r}') \frac{\partial \gamma(\mathbf{r}, \mathbf{r}')}{\partial \hat{\mathbf{n}}(\mathbf{r}')} \, \mathrm{d}\mathbf{r}' \tag{3.91}$$

where $\gamma$ is the Green function

$$\gamma(\mathbf{r}, \mathbf{r}') = \frac{1}{|(\mathbf{r} - \mathbf{r}')|} \tag{3.92}$$

In its discretised form Eq. (3.91) can be expressed as

$$\mathbf{\Phi_2} = B\ \mathbf{\Phi_1} \tag{3.93}$$

with $\mathbf{\Phi_1}$ and $\mathbf{\Phi_2}$ being the vectors containing the values of the potential $U_1$ and $U_2$ on the surface nodes of the magnetic body(ies), respectively, and $B$ is the so called boundary element matrix. If the mesh uses first order elements, an analytical formula given by Lindholm [46] that describes the potential of a triangular dipole layer with linearly varying source density can be used to compute the matrix elements.

The boundary element matrix $B$ is a dense $N \times N$ matrix, where $N$ is the number of surface boundary nodes (surface nodes of the magnetic body(ies)), and even for moderately sized problems its storage may require a considerable amount of memory. This characteristic is critical in the case of thin film geometries, where the surface nodes represent a large part of the total nodes of the mesh. However the matrix $B$, containing information on the geometry of the system, needs to be computed only once, and there are approximation techniques [47] which allow to reduce the size of the matrix maintaining a control on the error introduced by such approximation.

The values of $\mathbf{\Phi_2}$ on the boundary nodes obtained from Eq. (3.93) are used as boundary conditions for the solution of Eq. (3.89) in all the internal nodes, the nodes of the mesh inside the magnetic objects.

With this approach the values of $U_2$ are computed for all the nodes of the mesh (since the empty space is not meshed), and $U_{\mathrm{dem}}(\mathbf{r})$ is known over all the space by Eq. (3.88) having previously computed the values of $U_1$ over all the nodes from Eq. (3.86) and (3.87) using the standard FEM.

Eventually the demagnetising field $\mathbf{H}_{\mathrm{dem}}(\mathbf{r})$ is computed over all the (meshed) space from $U_{\mathrm{dem}}(\mathbf{r})$ using the expression in Eq. (2.19), which takes the form of Eq. (3.85) in its numerical version.

### 3.4.3 Computational energies

With the expression of the demagnetising field obtained by the FEM or FEM/BEM the demagnetising energy can be written as

$$E_{\rm dem} = -\frac{\mu_0}{2}\int_V \mathbf{M}(\mathbf{r})\cdot\mathbf{H}_{\rm dem}(\mathbf{r})\,{\rm d}V \tag{3.94}$$

$$E_{\rm dem}^{\rm num} = -\frac{\mu_0}{2}\sum_{i=1}^{m}\mathbf{m}_i\cdot\mathbf{h}_i^{\rm d}\,V_i \tag{3.95}$$

where $m$ is the number of nodes in the mesh and $V_i$ the volume associated with each node $i$. Calling $V_\eta^i$ the volume of the $\eta-$th element containing the node $i$, in the 3D case the node volume is the sum of all $V_\eta^i$ weighted by the number of nodes per element [48]

$$V_i = \frac{1}{4}\sum_{\eta=1}^{4} V_\eta^i \tag{3.96}$$

In the same way the analytical expressions for Zeeman and uniaxial anisotropy energies can be transformed into their computational analog by:

$$E_{\rm Zee} = \int_V -\mu_0\,\mathbf{M}(\mathbf{r})\cdot\mathbf{H}^{\rm a}(\mathbf{r})\,{\rm d}V \tag{3.97}$$

$$E_{\rm Zee}^{\rm num} = -\mu_0\sum_{i=1}^{m}\mathbf{m}_i\cdot\mathbf{h}_i^a\,V_i \tag{3.98}$$

and

$$E_{\rm uni} = \int_V -K_1^u\left(\frac{\mathbf{M}(\mathbf{r})\cdot\mathbf{c}}{\mathbf{M}_s}\right)^2{\rm d}V \tag{3.99}$$

$$E_{\rm uni}^{\rm num} = -K_1^u\sum_{i=1}^{m}\frac{|\mathbf{m}_i\cdot\mathbf{c}|^2}{|\mathbf{m}_i|^2}\,V_i \tag{3.100}$$

where the uniaxial anisotropy constant $K_1^u$ is assumed to be constant over all the magnetic material and the magnitude of the magnetisation vector is set to $M_s$.

The computational version of the exchange energy can be computed with the same procedure used for its continuous expression. In fact it is sufficient to substitute the sum over the unit cells in Eq. (2.7) with a sum over the nodes $N$ of the mesh provided that their separation is smaller than the exchange length of the material (see Eq. (2.52)).

With this definition the numerical exchange energy in the case of a material with a

simple cubic unit cell is defined by

$$
\begin{aligned}
E_{\text{exch}}^{\text{num}} &= A\int_V \Big(\nabla \mathbf{u}(\mathbf{r})\Big)^2 \,\mathrm{d}V && (3.101)\\
&= A\sum_{e=1}^{N}\int_{V^e}\sum_{\eta=1}^{4}\Big(\nabla L_\eta^e \mathbf{u}_\eta^e\Big)^2 \,\mathrm{d}V && (3.102)\\
&= A\sum_{e=1}^{N}\sum_{\eta=1}^{4}\frac{\Big(u_{\eta,\mathrm{x}}^e b_\eta^e + u_{\eta,\mathrm{y}}^e c_\eta^e + u_{\eta,\mathrm{z}}^e d_\eta^e\Big)^2}{36V^e} && (3.103)\\
&= A\sum_{i=1}^{m}\alpha_i && (3.104)
\end{aligned}
$$

where $\mathbf{u}(\mathbf{r})$ is a unit vector pointing in the direction of the magnetisation and $\alpha$ contains the information on the derivative of the interpolated $\mathbf{u}(\mathbf{r})$.

## 3.5 Computational dynamics

In Sec. 2.8 we have seen how the dynamics of the magnetisation vector is based on the LLG equation. That equation describes how an effective applied field and a damping term control the evolution of the magnetisation of a system towards a point of minimum energy. The lack of an analytical solution requires a numerical approach to the problem and various numerical schemes have been developed to this aim. These techniques differ on the balance between accuracy, stability and computational requirements and two methods are presented here that, when combined, result in a scheme particularly suitable for our case. In fact the computation of the right-hand side of Eq. (2.65) is dominated by the derivation of the demagnetising field, an heavy computational task which can be effectively addressed with the 4th-order Runge-Kutta method coupled with the Adams-Bashforth-Moulton multistep method [34].

Before describing the concepts behind the Runge-Kutta method let express the LLG equation in its numerical form. Recalling the expression of the effective field given in Eq. (2.63)

$$
\begin{aligned}
\mathbf{H}^{\text{eff}}(\mathbf{r}) &= \frac{2A}{\mu_0 M_{\text{s}}}\nabla^{\mathbf{2}}\mathbf{u}(\mathbf{r}) + \mathbf{H}(\mathbf{r}) + \frac{2K_1^u}{\mu_0 M_{\text{s}}}\Big(\mathbf{u}(\mathbf{r})\cdot\mathbf{c}\Big)\mathbf{c} && (3.105)\\
&= \frac{2A}{\mu_0 M_{\text{s}}}\nabla^{\mathbf{2}}\mathbf{u}(\mathbf{r}) + \mathbf{H}_{\text{dem}}(\mathbf{r}) + \mathbf{H}_{\text{ext}}(\mathbf{r}) + \frac{2K_1^u}{\mu_0 M_{\text{s}}}\Big(\mathbf{u}(\mathbf{r})\cdot\mathbf{c}\Big)\mathbf{c} && (3.106)\\
&= \mathbf{H}_{\text{exch}} + \mathbf{H}_{\text{dem}} + \mathbf{H}_{\text{ext}} + \mathbf{H}_{\text{uni}} && (3.107)
\end{aligned}
$$

within the numerical model described so far the contribution from the exchange energy in

this expression represents a problem. In fact the first order of the interpolation functions $L_i$ makes the second derivative of the term $\mathbf{h}_{\text{exch}}$ difficult to evaluate. Therefore its computation is performed expressing the field $\mathbf{H}_i$ associated to node $i$ with volume $V_i$ using the relation

$$\mathbf{H}_i = -\frac{1}{V_i \mu_0 M_\text{s}} \left( \frac{\delta E}{\delta \mathbf{u}_i} \right) \approx -\frac{1}{V_i \mu_0 M_\text{s}} \left( \frac{\partial E}{\partial \mathbf{u}_i} \right) \tag{3.108}$$

The contribution from the exchange energy to the field $\mathbf{H}_i$ can be derived by expressing the exchange energy in local coordinates as

$$\begin{aligned}
\mathbf{H}_i^{\text{exch}} &= -\frac{1}{V_i \mu_0 M_\text{s}} \left( \frac{\partial E_{\text{exch}}}{\partial \mathbf{u}_i} \right) && (3.109)\\
&= -\frac{1}{V_i \mu_0 M_\text{s}} \frac{\partial}{\partial \mathbf{u}_i} \left( \int_V A \Big( \nabla \mathbf{u}(\mathbf{r}) \Big)^2 \, \mathrm{d}V \right) && (3.110)\\
& && (3.111)\\
&= -\frac{A}{V_i \, \mu_0 \, M_\text{s}} \frac{\partial}{\partial \mathbf{u}_i} \left( \sum_{e=1}^{N} \int_{V^e} \sum_{\eta=1}^{4} \Big( \nabla L_\eta^e \mathbf{u}_\eta^e \Big)^2 \, \mathrm{d}V \right) && (3.112)\\
&= -\frac{A}{V_i \, \mu_0 \, M_\text{s}} \sum_{e=1}^{N} \sum_{\eta=1}^{4} \frac{\partial}{\partial \mathbf{u}_i} \Big( \nabla L_\eta^e \mathbf{u}_\eta^e \Big)^2 \, V^e && (3.113)\\
&= -\frac{A}{V_i \, \mu_0 \, M_\text{s}} \sum_{e=1}^{N} \sum_{\eta=1}^{4} 2 \Big( \nabla L_\eta^e \mathbf{u}_\eta^e \Big) \cdot \frac{\partial \nabla L_\eta^e \mathbf{u}_\eta^e}{\partial \mathbf{u}_i} \, V^e && (3.114)\\
&= -\frac{A}{V_i \, \mu_0 \, M_\text{s}} \sum_{e=1}^{N} \sum_{\eta=1}^{4} 2 \Big( \mathbf{u}_\eta^e \nabla L_\eta^e \Big) \cdot \nabla L_\eta^e \delta_{i\eta} \, V^e && (3.115)\\
&= -\frac{2A}{V_i \, \mu_0 \, M_\text{s}} \sum_{e=1}^{N|_i} \sum_{\eta=1}^{4} \mathbf{u}_\eta^e \nabla L_\eta^e \cdot \nabla L_i^e \, V^e && (3.116)\\
&= -\frac{A}{18 \, V_i \, \mu_0 \, M_\text{s}} \sum_{e=1}^{N|_i} \sum_{\eta=1}^{4} \mathbf{u}_\eta^e \, \frac{b_\eta^e b_i^e + c_\eta^e c_i^e + d_\eta^e d_i^e}{V^e} && (3.117)
\end{aligned}$$

where the sum over the $N$ elements is restricted to the ones containing the node $i$.

As the derivation of the others contributions to the expression of $\mathbf{H}_i$ do not present theoretical problems, dividing both sides of Eq. (3.106) by the quantity $\frac{2K_1^\text{u}}{\mu_0 M_\text{s}}$ we obtain the effective field $\mathbf{h}_{\text{eff}} = \mathbf{h}_{\text{exch}} + \mathbf{h}_{\text{dem}} + \mathbf{h}_{\text{ext}} + \mathbf{h}_{\text{uni}}$ in its non-dimensional form and we can proceed in the integration of LLG equation.

### 3.5.1 Runge-Kutta and Adams-Bashforth-Moulton methods

Runge-Kutta methods are a class of algorithms used to perform numerical integration of Ordinary Differential Equations (ODEs). They are known to have high accuracy and stability and the quality of the approximation of the solution depends on the order of the method. The solution is found using the iterative application of the Euler method, which consists in a Taylor expansion of the function which is refined at each iteration. The initial value problem represented by the LLG equation can be expressed by

$$y' = f\big(t, y_t\big) \qquad y(t_0) = y_0 \tag{3.118}$$

and the formula for its solution using the Euler method is

$$y_{t+h} = y_t + hf(t, y_t) + O(h^2) \tag{3.119}$$

where the solution is estimated at time $t + h$ using the current value $y_t$ and its derivative $f(t, y_t)$ times the time step $h$. This formula approximates the solution at first order in $h$ and Runge-Kutta methods minimise this error using trial steps to the midpoint of the interval $h$. The trial solutions obtained in this way are then combined to cancel out the errors in the Taylor expansion of $y$ at time $t+h$. The most common Runge-Kutta method is the 4th order one, whose name is commonly abbreviated to RK4 and is based on four evaluations of the function $f(t, y_t)$ to advance the solution $y$ from $t$ to $t + h$:

$$\begin{aligned}
k_1 &= hf(t, y_t) && (3.120)\\
k_2 &= hf(t + \frac{h}{2}, y_t + \frac{k_1}{2}) && (3.121)\\
k_3 &= hf(t + \frac{h}{2}, y_t + \frac{k_2}{2}) && (3.122)\\
k_4 &= hf(t + h, y_t + k_3) && (3.123)\\
y_{t+h} &= y_t + c_1k_1 + c_2k_2 + c_3k_3 + c_4k_4 + O(h^5) && (3.124)
\end{aligned}$$

where $c_1 = \frac{1}{6}, c_2 = \frac{1}{3}, c_3 = \frac{1}{3}, c_4 = \frac{1}{6}$.

The solution obtained with this algorithm depends on the choice of the time step $h$ and the efficiency of the integrator can be strongly improved with an adaptive step size. The reason is that, depending on the shape of the solution, the time step could result too large or too small for the given point on the solution curve, and a control on the step size is expected to increase the accuracy of the solution minimising the number of function evaluations.

The step size control for the RK4 algorithm can be embedded with a few more computational effort. The control works comparing the solution computed using a step size of

dimension $h$ with the solution obtained using a step size of dimension $h/2$, and the algorithms implementing such approach are classified by the number of function evaluations in the two cases.

The most frequently used algorithm, called RK45, needs six function evaluations at each time step to compute two solutions of 4th and 5th order Runge-Kutta algorithm. Setting an error on the difference between these solutions the algorithm controls the accuracy of the overall solution at the current step size and if needed adapts its length.

Despite of its efficiency, the six function evaluations needed by the RK45 algorithm at each time step could become a problem in a typical micromagnetic simulation, because of the lengthy computation of the demagnetising field. Moreover, with algorithms of the Runge-Kutta family only the information from one previous point is used to compute the next one.

This restriction is overcome in multistep methods, where the accuracy in the computation of $y_{t+h}$ is obtained interpolating a polynomial on the previous values $y_t,\ y_{t-h_1},\ y_{t-h_2},\ \ldots,\ y_{t-h_i}$ rather than having an iterative refinement of the solution at each point like in Runge-Kutta methods. The strength of this class of methods is that in the simplest case only one function evaluation is needed at each time step. A common choice among these methods is the so called predictor-corrector method, which computes the solution splitting the task in two sub-tasks at each time step. The first one uses the predictor algorithm. With the initial points $y_t, y'_t, y'_{t-h_i}$ it performs an iteration on the equation

$$y_{t+h} = y_t + h\left(\beta_1\, y'_t + \beta_2\, y'_{t-h_1} + \beta_3\, y'_{t-h_2} + \beta_4\, y'_{t-h_3} + \ldots\right) \tag{3.125}$$

giving an estimated value of $y^{\mathrm{extr}}_{t+h}$ through a polynomial extrapolation. Using the equivalence relation

$$y'^{\mathrm{extr}}_{t+h} = f^{\mathrm{extr}}\big(t+h, y_{t+h}\big) \tag{3.126}$$

the corrector algorithm performs the integration

$$y_{t+h} = y_t + h\left(\eta_1\, y'^{\mathrm{extr}}_{t+h} + \eta_2\, y'_t + \eta_3\, y'_{t-h_1} + \ldots\right) \tag{3.127}$$

This methods require the first three or four points to start the integration and they are typically computed using the RK45 algorithm.

Although predictor-corrector methods ensure a fast computation of the solution, they are more prone to numerical instability than the Runge-Kutta ones. In fact, depending on the properties of the LLG equation, sharp variations in the solution could be missed by the polynomial extrapolation and a possible way to limit this problem is the use of implicit methods. Therefore, a typical choice among predictor-corrector methods is the

Adams-Bashforth-Moulton scheme, where a non zero $\eta_1$ in Eq. (3.127) makes the method implicit.

Besides the one based on time integration of the LLG equation, there is another class of techniques that allow to find configuration of minimum energy for a magnetic system. Given a certain configuration, they are based on the analysis of the energy surface in a surrounding region of the phase space and evolve the system towards the local minima. The main theoretical advantage of this class of methods is to be significantly faster than their peers that describe the dynamics of the system with the integration of LLG equation, but in the rest of the thesis only the latter approach will be used.

## 3.6 Summary

Computational techniques are giving an increasing contribution to the study of micromagnetic systems. They are used to understand and design new experiments, to check theoretical predictions in ideal systems and investigate systems difficult to reproduce in a laboratory. An important task in computational models of micromagnetic systems is the correct discretisation of the domain, which must be done according to the condition which leads to Eq. (2.35): the larger dimension of the simulation cells must be smaller than the exchange lengths of the material. The main discretisation methods used in micromagnetic problems are finite differences and finite elements, and this chapter describes how to use these techniques to express the various energies and solve the crucial point in any micromagnetic simulation, the computation of the demagnetising field in the Poisson problem of Eq. (2.21).

The Finite Differences Method (FDM) uses constant-size cuboids to discretise the magnetic domain, and the solution is found by applying Fast Fourier Transform (FFT) algorithms to a simplified version of the Poisson equation. The simplification is a by-product of the discretisation method, and being based on a uniform domain discretisation the FDM is best suited to the study of prism-like geometries. For curved geometries the staircase approximation of the contours introduces spurious magnetic charges on the surface of the objects, which may affect the computation of the demagnetising field over all the space and eventually the magnetisation evolution in the system.

For such geometries the best discretisation method is the Finite Elements Method (FEM). This method uses an unstructured mesh typically made of simplices (triangles in 2D and tetrahedra in 3D), so that the solution can be adapted to any constraint of the domain. This property assures a superior accuracy of the method with respect to the finite differences, an advantage balanced by the simpler implementation of the latter.

Besides the different discretisation of the domain, the FEM discretises the solution of a

Partial Differential Equation (PDE) with a linear interpolation of the values on the mesh nodes rather than with constant cell-wide values as in the FDM.

In each cell of the mesh the solution is typically approximated with polynomials. The coefficients are determined minimising the distance from the exact solution, a minimisation performed using a norm in a suitable vector space. With this approach the accuracy of the solution can be improved arbitrarily by an adaptive refinement of the mesh on the domain and a common technique used for this purpose is the method of weighted residuals, a variational approach based on the minimisation, element-wise, of the original polynomials using suitable weighting function.

To have a sufficient accuracy of the solution to the Poisson problem, with the standard FEM approach the meshed region must extend in the empty space well beyond the surface of the magnetic objects. This is not the case when using the hybrid Finite Element/Boundary Element Method (FEM/BEM). This method solves the Poisson field problem solving an equivalent source problem, and open regions can be treated without truncation of the empty space as in the pure FEM approach. The difference is in the use of a boundary element matrix, a matrix which stores the information about the interactions between the surface charges of the magnetic objects and whose entries can be computed analytically if the finite element model of the system uses first order elements.

Compared to the demagnetising field, the computation of the remaining fields is typically straightforward and the numerical solution of the LLG equation is performed with algorithms that minimise the number of function calls to compute its right-hand side.

# Chapter 4

# Mesh generation for micromagnetic simulations

## 4.1 Introduction

As introduced in the previous chapter, the FEM has been the main computational model used to obtain the results presented in this thesis. In the most general case, with this approach the domain of the problem is tiled up with arbitrary polyhedra-shaped cells on an irregular grid, and the various fields (demagnetising, exchange, magnetisation but also electric or thermal in multi-physics problems) are defined on the elements of the mesh as explained in Sec. 3.3.2. The meshes used in the simulations of Chapter 6 and 7 are based on triangular (2D case) and tetrahedral (3D case) elements, and have been generated with NETGEN [49], a public 3D mesh generator, and Nmesh, a proof-of-concept mesh generator present in the Nmag framework.

The latter is an attempt to overcome the drawbacks of NETGEN for the generation of meshes used in micromagnetic problems. One of them is the large distribution of distances between nearest neighbour nodes (called rod lengths from now on). Since the micromagnetic model requires the magnetisation to satisfy the condition of small angles leading to Eq. (2.38), the mesh must have a maximum rod length which is smaller than the characteristic lengths of the material. If the distribution of rod lengths is very broad, the rod length $a_0$ specified in the NETGEN script must be taken much smaller than those to avoid having the maximum values beyond the limit. Since the average rod length is inversely proportional to the number of nodes in a mesh, and the associated system of equations expressed by Eq. (3.46) or the boundary element matrix $B$ in Eq. (3.93) is proportional to the number of nodes, the increase in memory requirements associated to a small (compared to the characteristic lengths of the material) average rod length represents a main constraint on the dimension of the systems to be investigated. In our

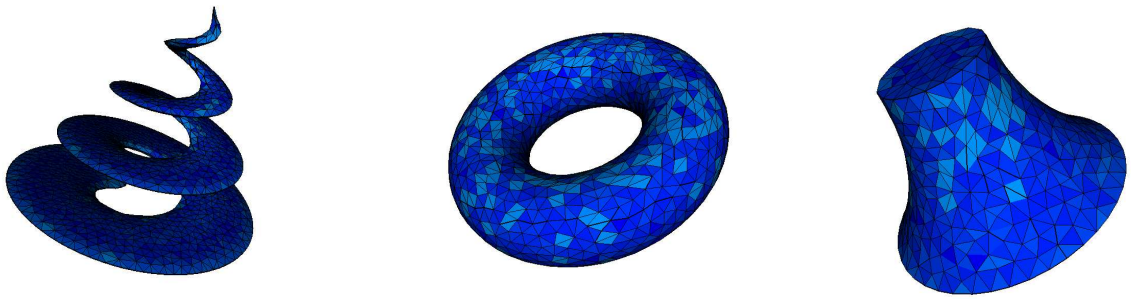

(**a**) (**b**) (**c**)

Figure 4.1: NETGEN hard-to-define geometries: (a) corkscrew, (b) torus and (c) truncated hyperboloid.

experience, for example, to keep the maximum rod length below 5 nm, the rod length to be specified in Netgen had to be at most 2.5 nm, losing a $2^N$ factor (with $N$ the dimension of the space), given the same number of nodes, with respect to an ideal mesh of 5 nm constant rod length in terms of maximum size of the system to be investigated.

Another limitation of NETGEN meshes is given by the restricted set of primitive geometries (plane, cylinder, ellipsoid, elliptic cylinder, cone, prism and polyhedron), so that objects like those in Figure 4.1 are rather difficult if not impossible to define. In some cases we found that a control on the density of mesh points as a function of space was desirable (in particular when dealing with magnetic systems characterised by vortices or domain walls), but NETGEN does not provide such a feature.

The restriction to 3D meshes and the need of a dedicated script to define the mesh completed the reasons to search for possible improvements to NETGEN, and to this aim we developed Nmesh. As mesh generation is an active field of study with a vast literature on meshing algorithms, our approach to the development of Nmesh has been based on one of the most simple algorithms to our knowledge. A brief description of the algorithm is presented in Sec. 4.2, while Sec. 4.2.1 introduces the main source of problems in mesh generation algorithms. The solution implemented in Nmesh is analysed in Sec. 4.2.2, where the performance of two versions of the algorithm is measured against the NETGEN algorithm.

## 4.2 Nmesh algorithm

The algorithm used for Nmesh is based on the work published on DistMesh, an $N$-dimensional mesh generator which requires less than 50 lines of MATLAB code to be implemented [50] and is reported in Appendix A. An initial set of points is distributed

randomly over the region to be meshed. Every point is then connected to its nearest neighbours, and a force acting along the connection pushes them apart with a force inversely proportional to their distance. The relaxation proceeds until an equilibrium of forces or a predefined number of iterations is reached. This algorithm is based on the analogy between the mesh and a truss structure and needs a minimum "pressure" level among the nodes in order to let them spread over all the space, a level controlled by the insertion and deletion of points.

The algorithm used in Nmesh can be roughly split in four parts: initialisation, computation of the forces, time step and node insertion/removal. The following list gives a brief explanation of the steps:

- **initialisation** - a series of basic geometrical objects (ellipsoids, frustums, boxes, but also less common shapes like those in Figure 4.1) are defined in a Python [51] script (see examples in Sec. B.2). These objects are then translated in a series of functions characterised by a positive value in the interior of the object and a negative value in the exterior.

  An example is a sphere of radius 1 in 3D, centered in the origin: the function used in this case is $x^2 + y^2 + z^2 - 1$, which takes negative values in the interior of the object, positive in the exterior and zero on the surface of the sphere. This function can be shown to be valid in N dimensions if we use as many square terms as the number of dimensions.

  Any geometrical transformation (rotation, scaling, shift) on an object is expressed as an affine transformation on the coordinates defining the kernel of the function and the union, intersection and difference of two objects are defined with the operators min, max and functional inversion.

  With this approach a new object which cannot be derived from operations on the basic geometries is easily implemented, and the default transformations are directly applicable without the need of extra functions.

  In the underlying OCaml [52] code, which receives the data from the Python interface, the functions defining the various objects are stored in a data structure, called `fem_geometry`, together with the coordinates of the bounding box, the density of points and the rod length.

  The initial points are inserted at random positions in the interior of the objects, and an initial triangulation allows to create the "truss structure" which is subsequently relaxed;

- **computation of forces** - the first phase of the relaxation involves computing the

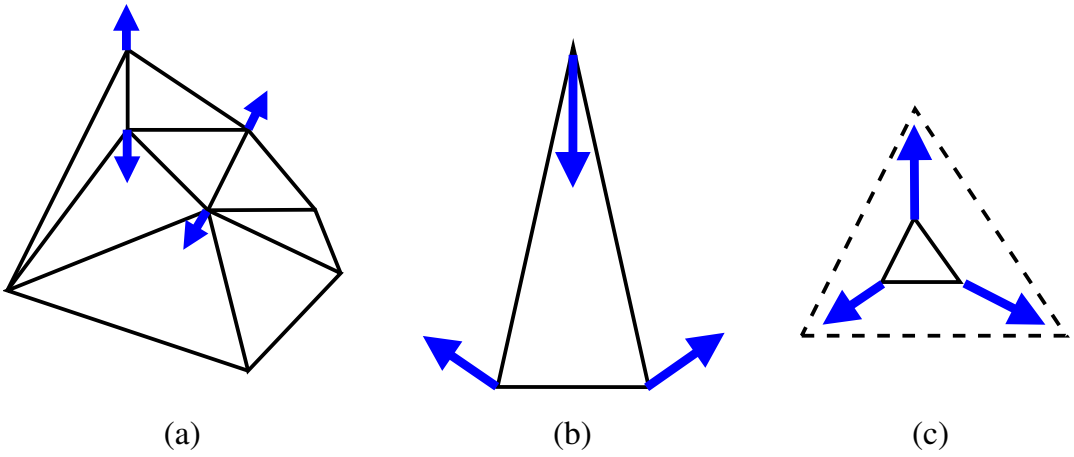


Figure 4.2: Effects of (a) neighbour, (b) shape and (c) volume forces on the nodes and simplices of a mesh.

forces acting on each point and taking the largest resulting force $f_{max}$ as the reference for the time step. The purpose is achieved in two steps. The first is calling Qhull [53] with the list of coordinates associated to the points. Qhull is the algorithm used to create a triangulation from a given set of points, and the outcome is used to obtain the list of simplices of the triangulation and compute the rod lengths between all the neighbour points. The second step is to use the information about the simplices and rod lengths to apply the following forces (whose effects are shown in Figure 4.2):

- ▷ **neighbour force** - this force is applied along each rod connecting two nodes and as previously introduced, it is inversely proportional to the distance between the nodes. The distance is computed as a ratio between the actual distance between the points and the ideal rod length (computed using the density of points provided in the Python script) associated to the middle point. If the distance ratio exceeds 1 the force is null, positive (repulsive) otherwise.

  This force is equivalent to the force in the original algorithm of DistMesh, but in Nmesh another force has also been tested. The new neighbour force is based on a Lennard-Jones potential, so that it becomes increasingly repulsive when the nodes get closer and mildly attractive when they are far apart. The expressions of the two forces are obtained defining the the normalised distance $w$

$$w = \frac{r}{r_0} \tag{4.1}$$

  with $r$ being the actual distance between two neighbour nodes located at

positions $x_1$ and $x_2$

$$r = \mid x_1 - x_2 \mid \tag{4.2}$$

and $r_0$ the ideal rod length in the midpoint $x_0$ between them, defined as

$$r_0 = \frac{R}{\delta(x_0)^{1/D}} \tag{4.3}$$

where $R$ and $\delta$ are the rod length and density of points specified in the Python script, respectively, and $D$ the dimension of the space ( 2 in 2D, 3 in 3D, *etc*). The expression for the linear force and Lennard-Jones potential are [50, 54]

$$\text{Linear force} \quad : \quad F_{\text{lin}} = \begin{cases} 0.0 & \text{if} \quad w > 1.0 \\ 1 - w & \text{otherwise} \end{cases} \tag{4.4}$$

$$\text{Lennard-Jones potential} \quad : \quad F_{\text{L-J}} = (1 - w^4) \cdot e^{-k \cdot w^4} \tag{4.5}$$

where $k$ is a variable taking values between 0.9 and 1.0.

- ▷ **shape force** - calling *sx* the generic simplex the shape force acts on the nodes to keep the simplex as regular as possible. The idea behind the method to compute such force is to rotate *sx* in the reference system of its principal axes of inertia. In this reference frame the associated ellipsoid of inertia is then gradually distorted in a sphere, so that the simplex gradually converges towards a regular one.
- ▷ **volume force** - this force acts on the nodes of each simplex *sx* to keep the volume as ideal as possible. The ideal volume is computed from the formula of a regular $N$-dimensional simplex [1] where the length of the edge ($l$) is represented by the ideal rod length in the centre of the simplex;

As will be discussed in Sec. 4.2.1 and 4.2.2, the neighbour force based on a Lennard-Jones potential and the shape and volume forces are introduced in the meshing algorithm to avoid poor meshes in dimensions higher than 2 (even if their effect is analysed also considering the 2D case). In fact the use of the sole linear neighbour force is sufficient to obtain good meshes in 1D and 2D [50], but in higher dimensions a relatively uniform distance between the nodes (an effect of the linear neighbour force) does not guarantee a high quality mesh. To define the quality of a mesh various measures can be used [55]; in the following discussion we will refer to the

[1]
$$V_N^{\text{ideal}} = \frac{\sqrt{N+1}}{N!\sqrt{2^N}} \; l^N \tag{4.6}$$

distribution of the incircle-to-circumcircle ratio, associated to each simplex of the mesh and defined by $Nr/R$ with $N$ the dimension of the space, $r$ the incircle radius and $R$ the circumcircle radius. Indicatively, meshes are considered of good quality if the distribution of incircle-to-circumcircle ratios does not have values lower than 0.3 (a value depending on the dimension of the space $N$, though) and, recalling the limit on the maximum rod length, the average rod length is as close as possible to the characteristic lengths of the given material.

- **time step** - the time step is the basic mechanism of the relaxation process: during a step each node $i$ is moved from the position $x_i^{\mathrm{t}}$ to the position $x_i^{\mathrm{t}+1}$ by applying the force $\mathrm{f}_i$ resulting from the neighbour, shape and volume components for a time interval dt expressed by a fraction of the quantity $1/\mathrm{f}_{\max}$. If the new position is outside the volume of the objects, the node is brought back on the nearest surface of the mesh, and a new triangulation is performed using the updated positions of the nodes;

- **insertion/removal of nodes** - as the meshing process starts from a random distribution of points, it is quite common to have the presence of regions with very high or very low density of points, especially in the first few steps of the relaxation process. In those cases the number of points is locally modified by inserting or deleting a point, a procedure based on certain conditions about the neighbour force acting on each node as well as the volume of the Voronoi polygon [56] associated to it.

  In more detail, if the force is above a given threshold or its Voronoi volume is too small, the node is identified as removable; if instead the force is very low or the Voronoi volume too large, the node is identified as isolated. If none of these two cases applies, the node status is left to normal. Such evaluation is stored in an array of statuses, one for each node, and the information is processed by a subsequent function which, using a probabilistic approach, for each nodes checks the corresponding status and leaves the node unchanged, deletes it or inserts a new point in a random position around the node itself.

The relaxation process is an iteration over the previous three steps (computation of the forces, time step and node insertion/removal) and when the maximum force $\mathrm{f}_{\max}$ falls below a given threshold (thus representing an equilibrium condition) or a predefined number of time steps is exceeded, the mesh is extracted. The extraction consists in a final triangulation and in the addition of the information about the mesh topology (as until now only the nodes coordinates and list of simplices were passed around). Eventually, after wrapping up the Ocaml resulting structure in a Python object, the mesh is returned to the function called in the Python script.

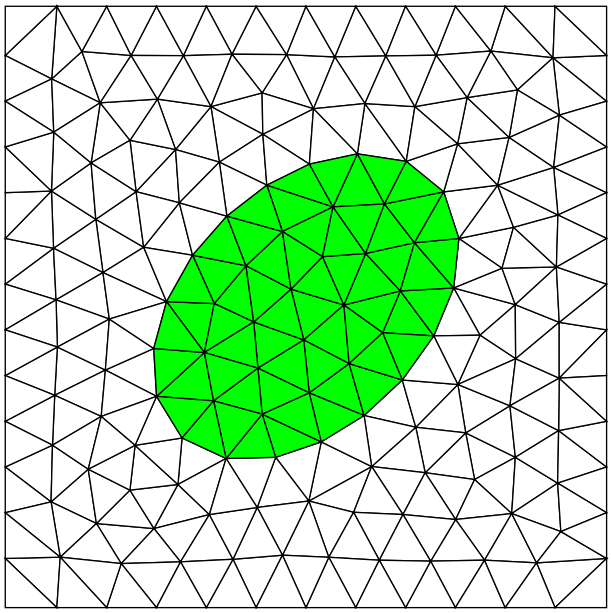

Figure 4.3: Mesh with periodic axes in x and y directions.

On top of these basic functions, further features are implemented in the meshing algorithm. One of those is that the `fem_geometry` structure accepts also a callback function (described in detail in Sec. B.5) to be executed at regular intervals specified by the user: this is a convenient feature to check the evolution of the mesh for debugging purposes, as it allows to extract a number of quality parameters during the mesh relaxation.

Moreover, to deal with the variety of cases and problems that can be encountered during the mesh generation, the main algorithm is split in an engine and a driver: the engine performs the core operations on the partially meshed objects (computation of the forces, time step and node insertion/removal), while the driver checks the status of the engine against possible stopping criteria and extracts a (intermediate) mesh when one of those is satisfied.

Another feature is that the `fem_geometry` is passed to the initialisation function together with optional mobile points, fixed points and periodicity conditions for the bounding box along some direction.

Depending on the status of the periodic boundary flags, the initialisation function performs two operations. If the periodic boundaries are selected, for every periodic axis of the space it creates a one dimensional mesh and copies the resulting points to all the edges of the bounding box along that axis: an example of a periodic mesh along the two axes of the space is shown in Figure 4.3.

The points associated to the meshed axes are then kept fixed and passed to the next

function, which would be directly called if periodic boundaries were not specified. Here the mesh is created, as outlined before, iterating over all the objects defined in the `fem_geometry`, with every new meshed object stored in a list of arrays in the form of nodes coordinates and associated simplices; at the extraction step, the topology is added for the overall mesh.

Among all the features of the Nmesh algorithm, the most notable can be summarised in the following list:

- a varying density of points can be specified by a C-function which is used to change the rod length specified by the user in each point of the space;
- the periodic feature allows to generate meshes with the same position of the nodes on all the boundaries along each axis of the space;
- the mesh can in principle be $N$-dimensional;
- a complete description of a micromagnetic simulation can be contained in a single file;
- by defining the objects with the kernel of functions, there is a a great freedom on their geometry.

From our experience the algorithm is very successful in 1D and 2D but in 3D geometries it suffers the problem common to most mesh generators: the presence of slivers.

### 4.2.1 Slivers

According to Shewchuk [57], slivers are "formed by arranging four vertices, equally spaced around the equator of a sphere, then perturbing one of the vertices slightly off the equator". Together with needles and caps (shown in Figure 4.4), the presence of these elements in a (3D) mesh affects the solution of the system of equations associated to the finite element method (expressed by Eq. (3.46)) by having excessive round-off errors when using direct methods or having a large condition number of the stiffness matrix [38, 58] when using iterative solvers, thus slowing down the computation of the solution.

Algorithms which remove the slivers or tetrahedra with poor quality measures work by inserting nodes near the circumcentre of these tetrahedra, perturbing the position of their nodes [59, 60], or applying a series of local swapping and smoothing operations in a specific order [61, 62, 63].

Due to its $N$-dimensional nature, the approach followed in Nmesh to prevent the formation of slivers has been to use the shape and volume forces previously introduced. This approach has been used to assess the difference between the two neighbour forces (the

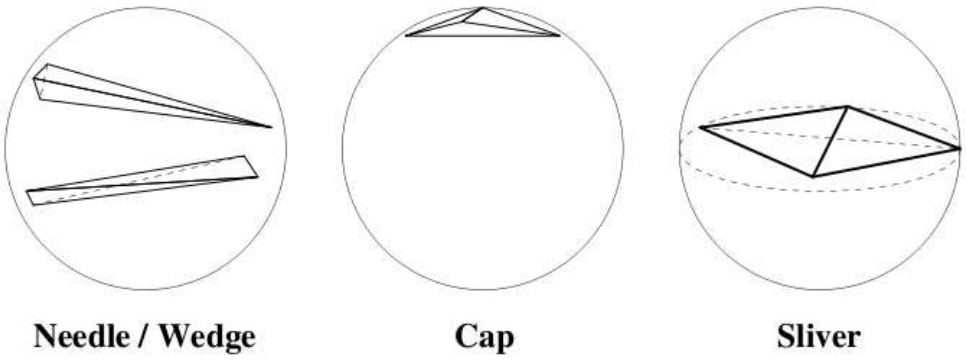


Figure 4.4: Poor quality tetrahedral elements (from [57]). Needles and wedges have edges of greatly disparate length; caps have a large solid angle; for slivers the quality, defined as $3r/R$ (with $r$ the radius of the tetrahedron's inscribed sphere and $R$ the radius of the tetrahedron's circumscribed sphere), is very poor.

one inversely proportional to the distance, called linear force in the following discussion, and the one based on Lennard-Jones potential) and a further comparison has been done with the NETGEN algorithm.

### 4.2.2 Mesh comparisons in 2D and 3D

The comparison between the two neighbour forces has been done for a number of geometries and, taking a circle as an example, the mesh is generated with the script `circle.py`, where a full explanation of the commands is reported in Appendix B.

`circle.py`

```
1  import nmesh
2
3  # create circle
4  ell = nmesh.ellipsoid([5.0,5.0])
5
6  # define bounding box
7  bbox = [[-6.,-6.],[6.,6.]]
8
9  # set the rod length
10 a0 = 0.1
11
12 # create mesh
13 mesh = nmesh.mesh(objects = [ell], bounding_box=bbox, a0=a0)
14
15 # plot mesh
```

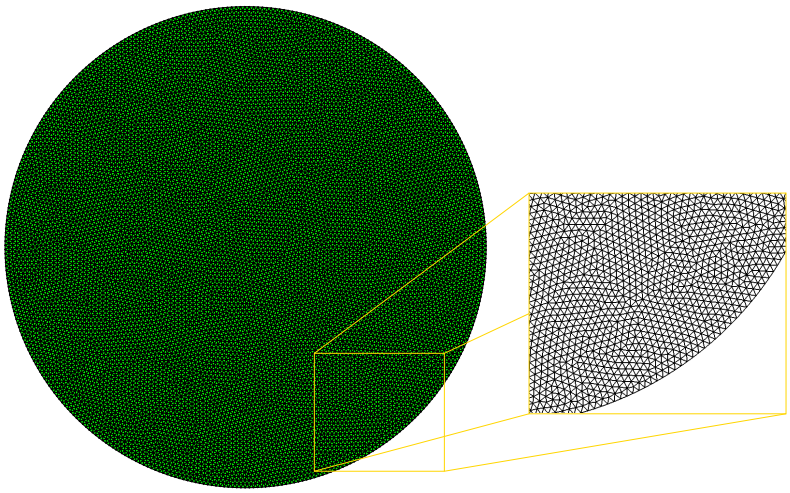

Figure 4.5: Mesh of a circle

```
16 nmesh.visual.plot2d_ps(mesh_ex,"circle.ps")
17
18 # save mesh
19 mesh.save('circle.nmesh')
```

The result of the script `circle.py` is shown in Figure 4.5. The quality of the triangular elements is defined as $2r/R$, with $r$ the radius of the incircle and $R$ the radius of the circumcircle.

Using the linear neighbour force the obtained mesh has 12132 points and 23903 simplices, while the use of the Lennard-Jones potential creates a mesh with fewer points and simplices, 9692 and 19118, respectively. The quality of the elements in the two cases is shown in Figure 4.6.

In the mesh created with the Lennard-Jones potential there are a few simplices with very poor quality, a condition balanced by having about 20% fewer nodes and elements than the mesh generated using the linear force. Concerning the rod lengths, the distribution associated to the two types of force is shown in Figure 4.7.

Again the mesh generated with the linear force is superior to that generated using the Lennard-Jones potential because of the long tail in the distribution of rod lengths for the latter.

Going to a 3D example, the script `sphere.py` has been used to make another comparison between a mesh generated using the linear force and a mesh generated using the Lennard-Jones potential (the choice between the linear force and Lennard-Jones potential has not been exported to the Python interface, so that in our tests we had to recompile

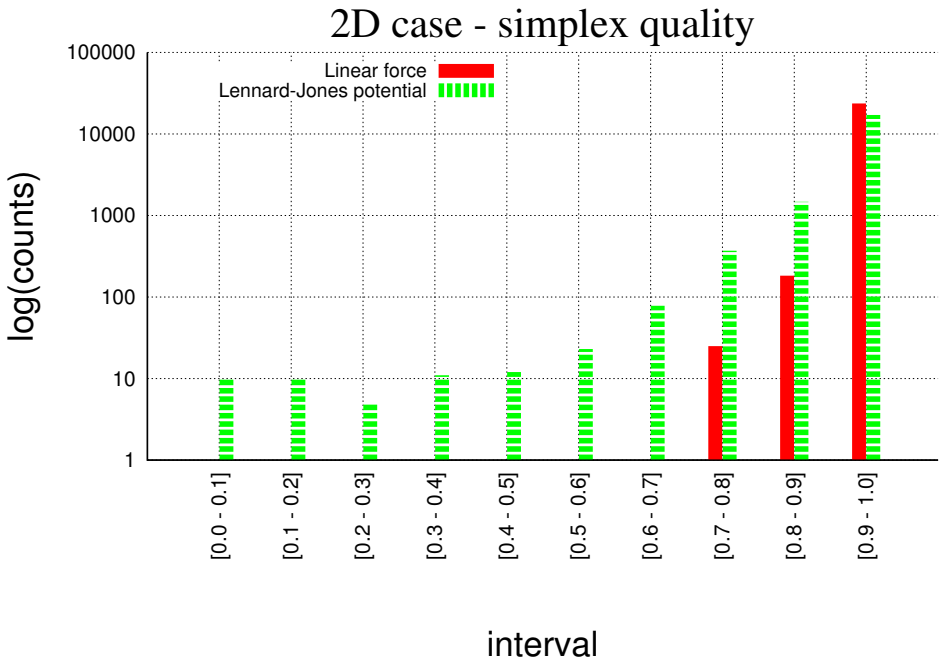


Figure 4.6: Quality of elements for a 2D circular mesh with linear force and Lennard-Jones potential. The lowest value of the quality using the linear force is 0.6, while it goes down to 0.1 when using the Lennard-Jones potential.

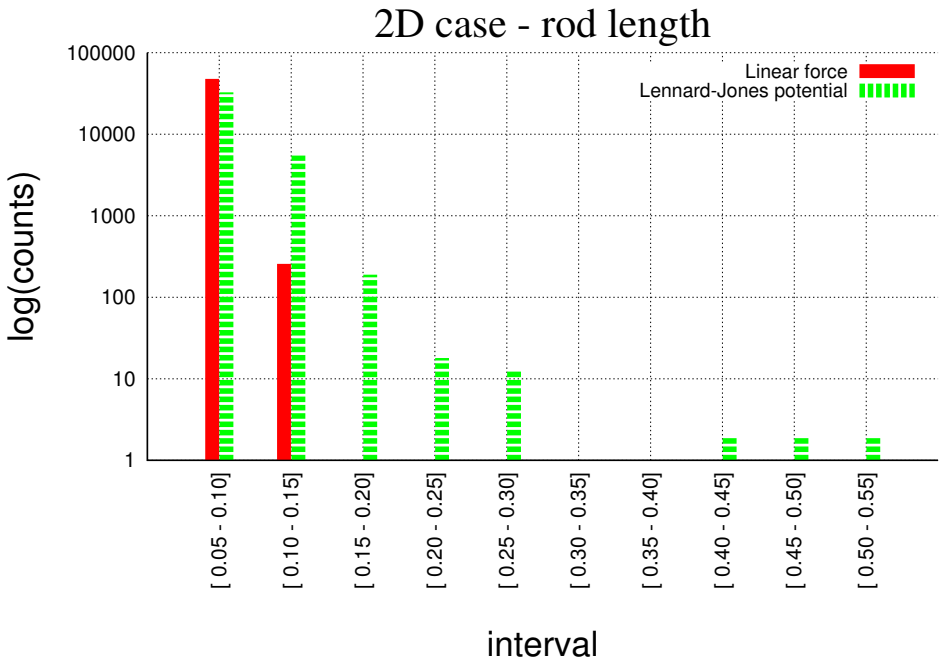


Figure 4.7: Rod length distribution for Nmesh with linear force and Lennard-Jones potential in a 2D circular mesh. The distribution of rod lengths is very narrow using the linear force, and the maximum value is 0.119. In the Lennard-Jones case the distribution has a long tail, and the maximum value is 0.532.

the code to switch from one to the other). Moreover, the two meshes are compared to that generated with NETGEN using the script `sphere.geo`. The values of 0.35 and 0.28 for the rod length in the two script are chosen in order to obtain meshes with comparable average rod lengths.

`sphere.py`

```
import nmesh

# create sphere
sph = nmesh.ellipsoid([3.0,3.0,3.0])

# define bounding box
bbox = [[-3.,-3.,-3.],[3.,3.,3.]]

# set rod length
a0 = 0.35

# create mesh
mesh = nmesh.mesh(objects = [sph], bounding_box=bbox, \
                  a0=a0, max_steps=300)

# plot mesh
vis = nmesh.visual.show_bodies_mayavi(mesh)
nmesh.visual.export_visualisation(vis,"sphere.eps")

#save mesh
mesh.save('sphere.nmesh')
```

`sphere.geo`

```
## mesh of a sphere

algebraic3d

solid sph = ellipsoid (0,0,0;3,0,0;0,3,0;0,0,3) -maxh=0.28;

tlo sph;
```

The result of the script `sphere.py` is shown in Figure 4.8. In this case the quality of the tetrahedra elements is defined as $3r/R$, with $r$ the radius of the insphere and $R$ the radius of the circumsphere.

Using the linear neighbour force the mesh is made of 8309 points and 45669 simplices, while the mesh created with the Lennard-Jones potential has 8780 points and 47134 sim-

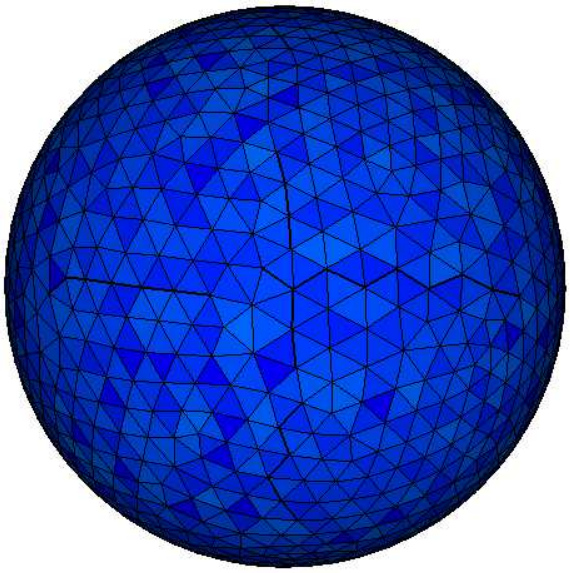

Figure 4.8: Mesh of a sphere.

plices. Comparing these number to those obtained from the NETGEN mesh, made of 6673 points and 34471 simplices, the difference is significant, in the range between 20% and 27% for both points and simplices. Concerning the quality of the simplices, the three cases are compared in Figure 4.9.

Unlike the 2D case, there is no significant difference between the distributions obtained using the linear force and the Lennard-Jones potential, and both show a few elements with very poor quality. This is not the case for the the distribution of qualities in the NETGEN mesh, a result of systematic elimination of bad simplices.

A side effect of such elimination is the difference in the number of simplices for the meshes obtained with Nmesh and that obtained with NETGEN, with the latter being 75% smaller than the others two. This is the consequence of the larger distribution of rod lengths rather than a more uniform distribution of points, as Figure 4.10 show.

The same figure also shows that the meshes generated with Nmesh have most of rod lengths below the value specified in the generation script, a valuable feature when dealing with micromagnetic simulations, as explained in the introduction of the chapter.

Moreover, the Nmesh meshes have relatively narrow bell-shape distributions of rod lengths, with the maximum rod length within 142% of the value specified in the generation script, while the NETGEN mesh has a much wider distribution with the maximum value

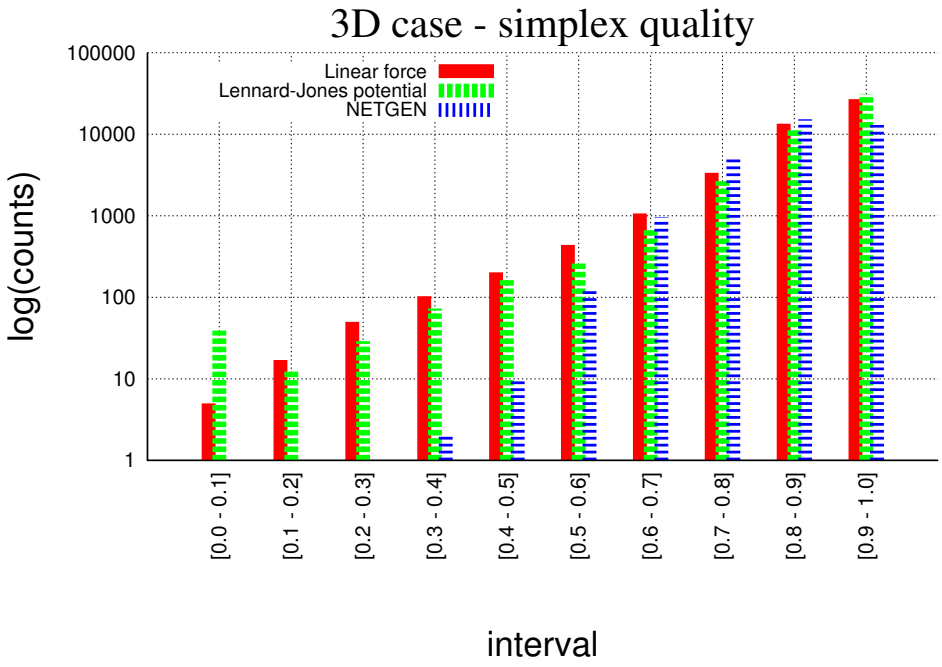


Figure 4.9: Quality of elements for a 3D spherical mesh using NETGEN and Nmesh with linear force and Lennard-Jones potential. The lowest value of the quality using NETGEN is 0.4, while it goes down to 0.1 when using the linear force as well as the Lennard-Jones potential.

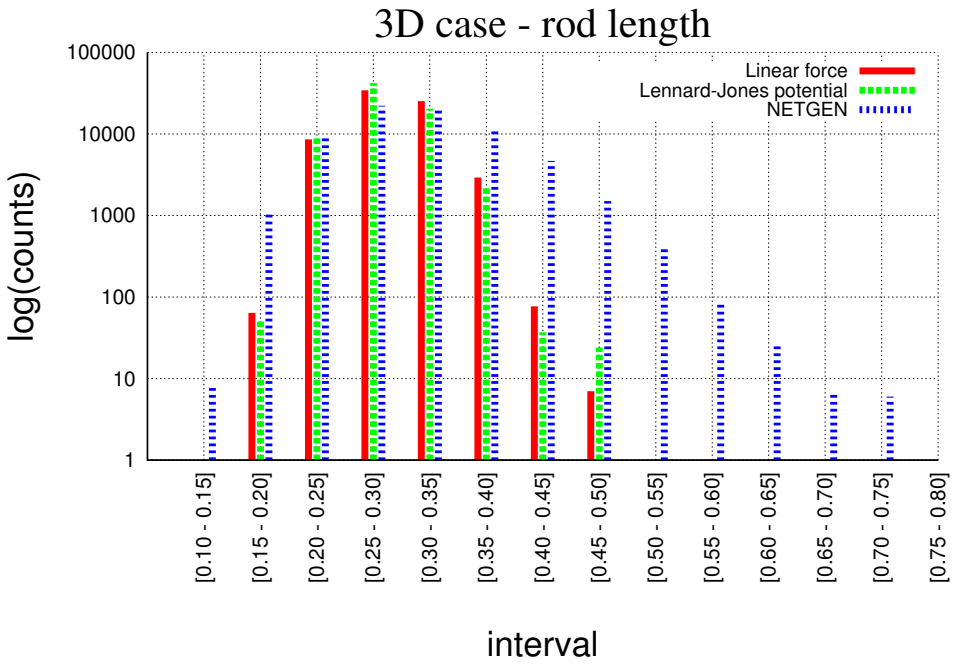


Figure 4.10: Rod length distribution for NETGEN and Nmesh with linear force and Lennard-Jones potential in a 3D circular mesh. The distribution of rod lengths using the linear force or the Lennard-Jones potential in Nmesh is narrower than that of NETGEN, with maximum values of 0.489 and 0.495 in the first two cases, respectively, and 0.778 in the NETGEN mesh.

at nearly 280% of the value specified in the generation script.

The conclusions obtained from these comparisons can be generalised to all the geometries we tested. The use of the Lennard-Jones potential does not show a net advantage over the use of the linear force and having the latter shown a better overall quality in 2D meshes, all the meshes generated with Nmesh have been based on this approach. Moreover in the 3D case the combination of neighbour, shape and volume forces have not been as successful as hoped, so that NETGEN has been the preferred choice to generate 3D meshes (such as those in Chapter 6) and Nmesh has been mostly used for the generation of 1D and 2D meshes (such as that in Chapter 7).

## 4.3 Summary

The Finite Element Method introduced in Chapter 3 has been the main computational model used to obtain the results presented in this thesis. The meshes, based on triangular (2D geometries) and tetrahedral elements (3D geometries), have been generated with NETGEN and Nmesh. NETGEN is a public 3D mesh generator, and being a general purpose software it presents some drawbacks in the generation of meshes for micromagnetic problems related to the distribution of distances between the mesh nodes. Nmesh is a proof-of-concept generator based on the work published on DistMesh and developed to overcome the problems of NETGEN. In Nmesh an initial set of points is distributed randomly over the region to be meshed. Every point is then connected to its nearest neighbours, and a force acting along the connection pushes them apart with a force inversely proportional to their distance, up to a limit specified by the user-defined rod length. The relaxation proceeds until an equilibrium of forces or a predefined number of iterations is reached. This algorithm is based on the analogy between the mesh and a truss structure and needs a minimum "pressure" level among the nodes in order to let them spread over all the space, a level controlled by the insertion and deletion of points. Among all the features of the Nmesh algorithm, the most notable can be summarised in the following list:

- a varying density of points can be specified by a C-function which is used to change the rod length specified by the user in each point of the space;
- a dedicated feature allows to generate meshes which are periodic along each axis of the space;
- a callback function can be executed at regular intervals of the mesh generation, a valuable feature for debugging purposes;

- the mesh can in principle be $N$-dimensional;
- a complete description of a micromagnetic simulation can be contained in a single file;
- the objects to be meshed are defined by the kernel of analytical functions, thus allowing great freedom on their geometry.

From our experience the algorithm is very successful in 1D and 2D but in 3D geometries it suffers the problem common to most mesh generators: the presence of slivers.

Slivers are poor quality simplices present in 3D meshes. They affect the solution of the system of equations associated to the finite element method by having excessive round-off errors when using direct methods or having a large condition number of the stiffness matrix when using iterative solvers, thus slowing down the computation of the solution.

A number of algorithms have been developed to remove slivers from 3D meshes, but the difficulty to extend them in $N$-dimensions has led us to tackle the sliver problem with a different approach: the use of shape and volume forces to keep the simplices as regular as possible.

These forces act on the nodes of the mesh together with the neighbour force previously introduced, and we have tested this solution meshing a large number of geometries.

The tests have been done using two types of neighbour forces: one inversely proportional to the distance between the nodes, called linear force, and one based on Lennard-Jones potential. In 2D geometries we have found that the linear force produces better quality meshes, having a narrower rod length distribution and a higher quality of the simplices.

Going to 3D geometries, meshes obtained with these two forces have also been compared to NETGEN meshes, and the comparison takes place between meshes with comparable average rod length. Unlike the 2D case there is no significant difference between the meshes obtained using the linear force and the Lennard-Jones potential; however both approaches produce meshes having few elements with very poor quality.

This is not the case for the distribution of qualities in the NETGEN mesh, a result of systematic elimination of bad simplices rather than the prevention of their formation as in Nmesh. The consequence of such elimination is that NETGEN meshes have a large distribution of rod lengths, a major problem when dealing with micromagnetic simulations.

Nonetheless, in some cases the use of NETGEN was the only way to have a sufficiently good, though much larger than needed in terms of number of simplices, working mesh.

The conclusions obtained from the comparisons presented in the chapter can be generalised to all the geometries we tested. The use of the Lennard-Jones potential does not show a net advantage over the use of the linear force, and having the latter shown a better

overall quality in 2D meshes, all the meshes generated with Nmesh have been based on this approach. Moreover in the 3D case the combination of neighbour, shape and volume forces have not been as successful as hoped, so that NETGEN has been the preferred choice to generate 3D meshes and Nmesh has been mostly used for the generation of 1D and 2D meshes.

# Chapter 5

# A new approach to (quasi) periodic boundary conditions: the macro geometry

The work described in this chapter has been submitted to the Journal of Applied Physics [64].

## 5.1 Introduction

In micromagnetics, as in many other areas of research, one would often like to simulate a micromagnetic system that is significantly larger than what can be computed within reasonable time and available memory. One way to address this problem is the use of Periodic Boundary Conditions (PBC).

Using PBC, the surface of the system is pushed infinitely far away along the periodic axes. However, in micromagnetics one loses the information about the demagnetisation field of the system due to the disappearing surface charges. This can significantly affect its magnetic behaviour.

To overcome this problem and model large but finite systems a new approach has been implemented in Nmag. This approach is called "macro geometry" and differs from PBC in that the number and position of the quasi-periodic copies are explicitly defined. With this approach the information about the overall shape (*i.e.* the Macro Geometry, or MG in the following) of the system is preserved, thus representing the demagnetisation field more accurately than using PBC.

Sec. 5.2 describes the idea behind the macro geometry approach and Sec. 5.3 and 5.4 present calculations for 3d ferromagnetic structures, quasi-periodic in one or two directions, where the advantages of MG over PBC are shown.

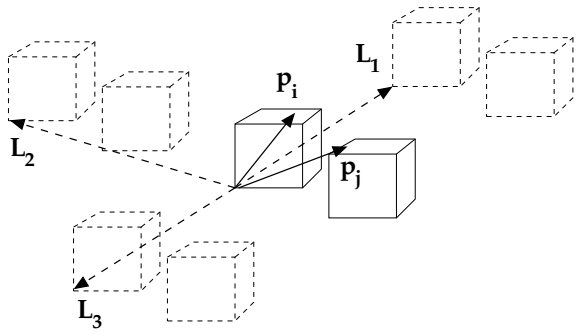


Figure 5.1: Concept behind the macro geometry approach. Quasi-periodic copies of the primary cell are displaced at lattice vectors $\mathbf{L}_k$ and the interactions between the points $(\mathbf{p}_j + \mathbf{L}_k)$ and $\mathbf{p}_i$ are added as extra contribution to the entry $B(i,j)$ of the boundary element matrix, which encodes only the interaction between the points $\mathbf{p}_j$ and $\mathbf{p}_i$ in non-periodic systems.

## 5.2 Macro geometry: theory

The macro geometry concept can be seen as an extension of the hybrid Finite Element/Boundary Element Method (FEM/BEM) described in Sec. 3.4.2.

In fact, despite being initially intended for non-periodic geometries, the ability of the Boundary Element Matrix (bem) $B$ to capture the interaction between surface charges of the magnetic objects can be exploited to deal with quasi-periodic copies of the system.

In a non-periodic system the entry $B(i,j)$ of the bem essentially encodes the expression in Eq. 2.14 where $\mathbf{r} = \mathbf{p}_j - \mathbf{p}_i$ is the vector between the positions $\mathbf{p}$ of the generic nodes $i$ and $j$ lying on the surface of the magnetic objects.

By considering $n$ quasi-periodic copies of the system, extra contributions can be added to $B(i,j)$ such that also the interactions between the generic node $i$ in the primary cell and all the nodes $j_k$, $k = 1 \dots n$ in the $n$ copies of the system are considered.

Calling $\mathbf{L}_k$, $k = 1 \dots n$ the lattice vectors defining the position of $n$ displaced copies of the system, the $k$-th extra contributions to the entry $B(i,j)$ of the bem is obtained similarly to the non-periodic case where now $\mathbf{r} = \mathbf{r}_k = (\mathbf{p}_j + \mathbf{L}_k) - \mathbf{p}_i$, $k = 1 \dots n$ (see Figure 5.1).

In this way the effect of the quasi-periodic copies of the original system is included in the computation of the demagnetising field

and the possibility to define the number and position of such copies allows to simulate very large systems maintaining the information about the overall geometry.

The fact, true also for the PBC approach, that all the virtual copies have the same magnetisation configuration of the original system might be seen as a limitation of this

approach but in the following examples we will see that for some geometries the effect is sufficiently small to have a good agreement between the behaviour of a large magnetic system and its reduced quasi-periodic version.

## 5.3 Demagnetising field in a 1D structure

To evaluate the accuracy of the MG approach we start with its application to a 1D system. We consider a ferromagnetic prism of dimension $L \times 15 \times 15$ nm$^3$ with $L$ going from 15 to 1215 nm and compute the demagnetising field at its centre as a function of the length $L$. When the magnetisation is uniform and aligned with one of the main axes, the value of the demagnetising field has a direct relation with the demagnetising factors of the prism. This values are then compared to a second set of values, obtained using the analytical expression for prisms [65], and we show the good agreement between the two sets.

We use Nmag to model the system by a real (central) cube and a number of quasi-periodic copies along the x-axis (the periodic axis), and compare the results to those obtained from OOMMF [66] using a real prism of length $L$. OOMMF uses an analytical formula to compute the demagnetising field of prisms, which reduces to their demagnetising factors when the magnetisation is aligned along one of the edges, so that the comparison is effectively between MG and analytical results.

The simulation is performed for two cases: (a) with a uniform magnetisation parallel to the x-axis and (b) with a uniform magnetisation along the y-axis, thus orthogonal to the periodic direction.

Figure 5.2 shows the excellent agreement between the Nmag and OOMMF data. On the x-axis of the graph are the number of copies of the cubic unit cell (whose size is $15 \times 15 \times 15$ nm$^3$), while on the y-axis is the demagnetising field at the centre of the prism expressed as the ratio with the saturation magnetisation $M_s$.

Both cases start from a value of 1/3 when the size of $L$ is 15 nm, the demagnetising factor of a cube along any of the axes parallel to an edge. Increasing the value of $L$ or, more precisely, the number of copies of the primary cell in the MG model and the corresponding length of the real prism in OOMMF, the system quickly approaches the geometric characteristics of a needle. Therefore in the case (a) the value of the demagnetising field converges towards 0, the demagnetising factor of an infinite needle with the magnetisation parallel to the longest axis, and a similar behaviour occurs in the case (b), where the demagnetising factor is 0.5. These values are also confirmed simulating the relaxation of a single cell with periodic boundary conditions in OOMMF, where in both cases the deviation is smaller than $1 \times 10^{-8}$ from the value of a truly infinite system.

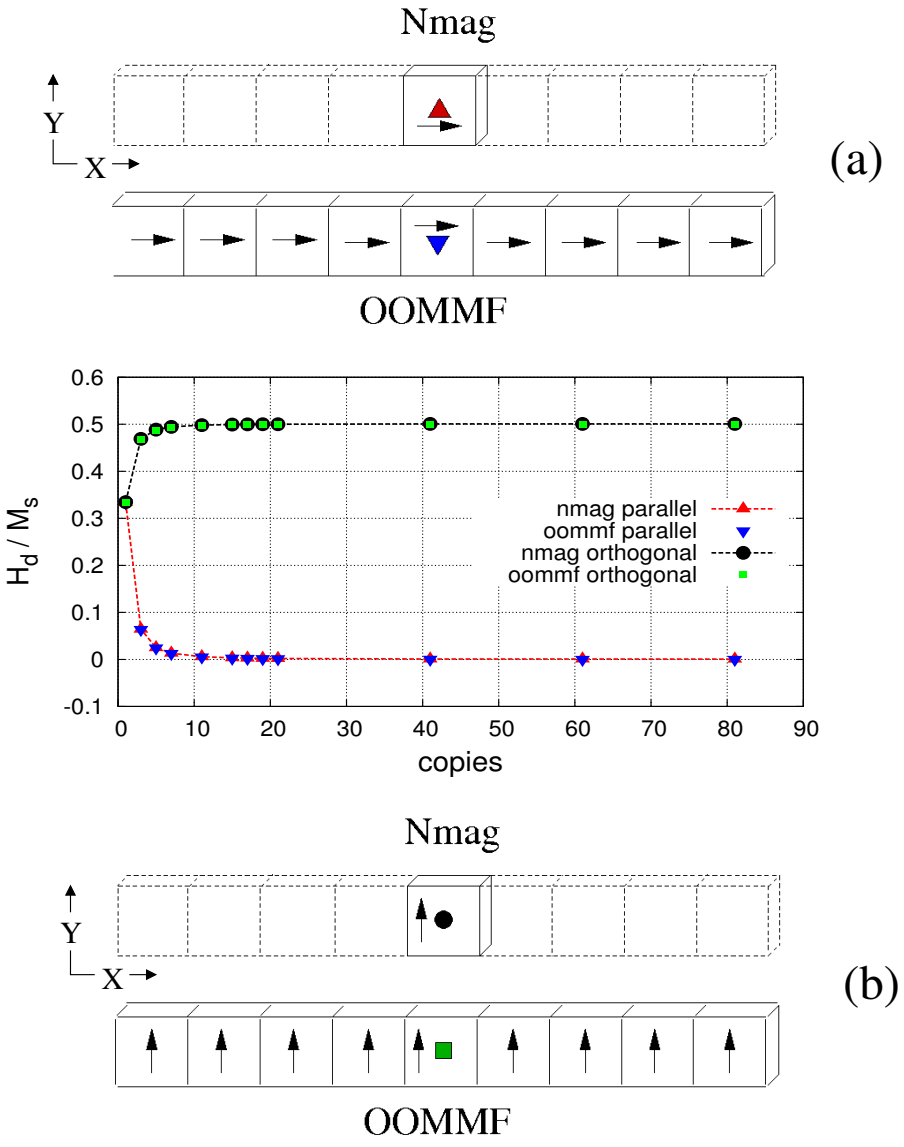


Figure 5.2: Demagnetising field $H_\mathrm{d}/M_\mathrm{s}$ in the central cell of a quasi-periodic array with a uniform magnetisation (a) parallel to the periodic direction and (b) orthogonal to it. The demagnetising field is computed at the centre of the cell using the macro geometry approach (Nmag) and an array of real cubes (OOMMF).

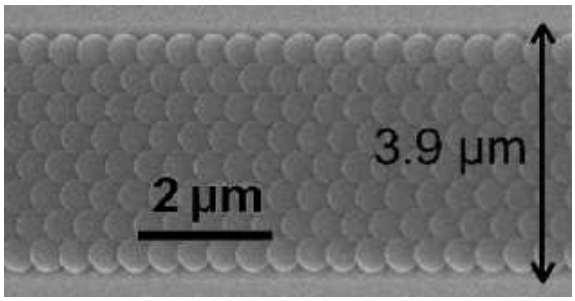


Figure 5.3: Latex template used for sample growth (reproduced from [67]).

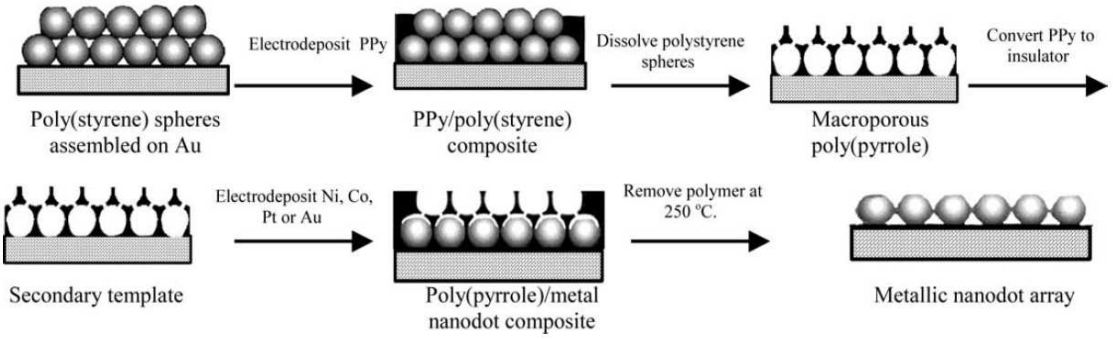


Figure 5.4: Schematic representation of the sequence of steps used in the double templated electrodeposition of arrays of metal nanodots (reproduced from [68])
.

## 5.4 Spheres in a 1D stripe

Having proved its accuracy in a 1D example, the MG is now applied to a 2D geometry. The system under investigation is obtained from the latex template in Figure 5.3.

As explained in Figure 5.4, the technique to obtain an array of magnetic spheres from this template consists of two steps: an array of poly(styrene) spheres like that in Figure 5.3 is used as a first template for the electrodeposition of poly(pyrrole) (PPy) on a Au substrate. The poly(styrene) spheres are then soaked in tetrahydrofuran and the remaining PPy structure, converted to an insulator by cycling a current through it, is used as a secondary template for the electrodeposition of the magnetic material. The final step is the removal by heating of the PPy template, and the resulting array of magnetic nanodots looks like the structure of Figure 5.3 where the latex is replaced by Ni, Co, Pt or Au.

In this example a computational model of the structure in Figure. 5.3 is simulated by

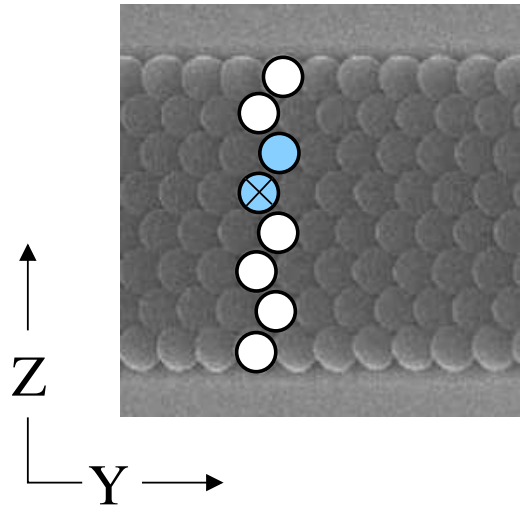


Figure 5.5: The overlaid circles represent the 8 spheres studied in the simplified system. The coloured spheres are part of the Nmag primary cell, the other 6 spheres are represented through 3 image cells of the primary cell. The OOMMF simulations compute the full 8 spheres. The graphs of the magnetisation relaxation in Figure 5.6 refer to the sphere marked with a cross (x).

considering the relaxation of a single sphere in the middle of the array. The material is Py and the numerical integration of the LLG equation is performed using the multi-step method available in the Sundials package [69] (all the Nmag simulations use the same technique unless specified otherwise).

A first simulation is done using a simplified version of the original structure which uses only 8 spheres and is shown in Figure 5.5.

The system is modelled with MG using only the two coloured spheres shown in Figure 5.5.

The simulation is performed on this primary cell, while the rest of the system is obtained by two copies of this cell along the negative z-direction and one copy along the positive z-direction.

The magnetic behaviour of this system is compared to that of 8 real spheres simulated with OOMMF. In this case the numerical integration is performed using the Runge-Kutta method, and all the OOMMF simulations use the same technique unless specified otherwise.

As the distance between the spheres in the original sample is small compared to the size of the spheres, the OOMMF model needs to use a very fine grid to resolve the spacing between the spheres. As a consequence the size of the system which can be simulated in reasonable time must be smaller than that of the original sample, and we decided to

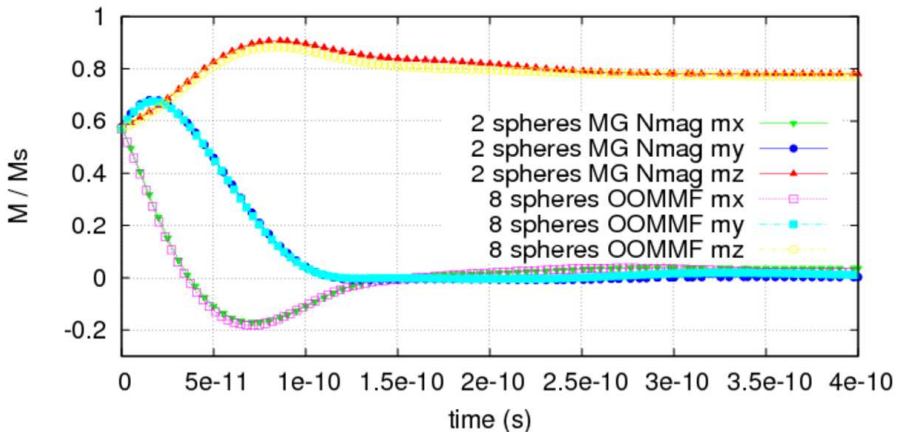


Figure 5.6: Relaxation of the magnetisation in the sphere marked with a cross in Figure 5.5. The primary cell in the Nmag system, made of the two coloured spheres in Figure 5.5, is repeated 4 times along the z-axis using the MG, while the OOMMF system is made of 8 real spheres.

perform the simulation with spheres of radius 25 nm and cells size of $1 \times 1 \times 1$ nm$^3$.

The MG approach does not need a very fine discretisation of the space because in the underlying FEM/BEM method only the magnetic objects are considered. Therefore the non-magnetic space between the spheres is not meshed, and its size does not affect the coarseness of the overall mesh.

Starting from a uniform $[1, 1, 1]$ direction of the magnetisation, the evolution of its three components for the OOMMF model (made of 8 real spheres) and the Nmag one (made of a primary cell containing two spheres, which is copied two times along the negative z-axis and one time along the positive z-axis using the MG) as a function of time is shown in Figure. 5.6. There is no significant difference between the Nmag and OOMMF curves, confirming that in this low-dimensional case MG describes the true system with an high degree of accuracy.

For comparison, it is also interesting to see how an OOMMF model of two spheres with PBC compares to the OOMMF reference model of 8 real spheres.

Such comparison is shown in Figure 5.7. Although the two OOMMF models have a similar behaviour, the comparison with Figure 5.6 shows the magnetisation curves from the previous MG model to be closer to the reference ones.

Going to larger systems, with the MG approach any number of spheres can be easily introduced in the model, while with OOMMF the simulation of 8 spheres is already very computationally demanding, and the only way to simulate more spheres is by using PBC.

Therefore we design a new OOMMF model made of 8 real spheres as in Figure 5.8,

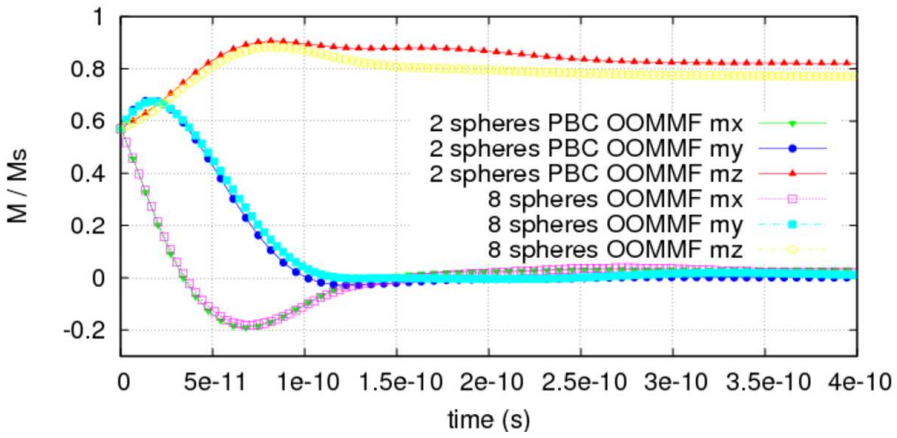


Figure 5.7: Relaxation of the magnetisation using two OOMMF models. The first model uses the two coloured spheres in Figure 5.5 in the primary cell and periodic boundary conditions along the z-axis, while the second model uses the full system of 8 real spheres in Figure 5.5.

with PBC along the z-axis. The relaxation of the magnetisation in this model is now compared to that of an Nmag model with 2 spheres repeated along the y and z-axis by means of MG. For this model we used arrays with dimensions in the range $3 \times 8$ to $31 \times 8$ spheres, where we renamed $1 \times 8$ the system of $2 \times 4$ spheres shown in Figure 5.5.

In this case the starting configuration is a uniform magnetisation along the $[1, 0.1, 0.1]$ direction for all the spheres, that is an out-of-plane direction considering the y-z plane as the plane where the magnetisation will finally lie.

We have found that a MG array of $9 \times 8$ is sufficient to relax the magnetisation along the z-axis (instead of the y-axis as in the $1 \times 8$ model), and the comparison between a $31 \times 8$ array modelled in Nmag and the periodic array modelled in OOMMF is shown in Figure 5.9.

Despite the significant difference between the models the magnetisation evolution in the OOMMF and Nmag models is very similar.

Part of the reason is that the central spheres along the y-axis in the OOMMF model are relatively free from surface effects, thus resembling the environment of the spheres in the Nmag model, and the initial out-of-plane configuration limits the formation of vortices in the outermost spheres (whose evolution is very sensible to small differences in the magnetisation distribution). An image of the relaxed configuration in the OOMMF model with the vortices in the outermost elements is shown in Figure 5.10.

Nevertheless, the MG concept implemented in Nmag shows a possible way to study large finite systems which are otherwise impossible to study with OOMMF. In fact, should

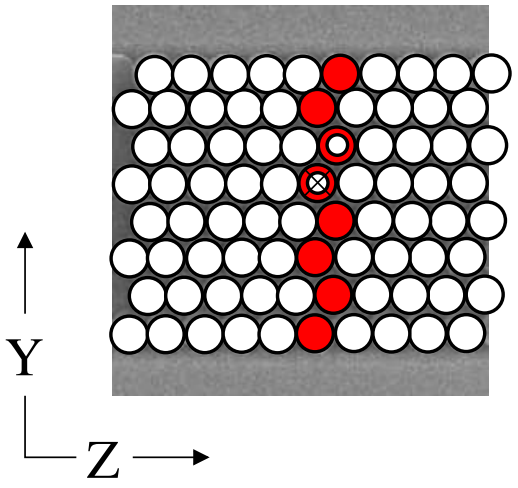


Figure 5.8: OOMMF model of 8 real spheres (red ones) with PBC along the z-axis. The magnetisation curves in the sphere marked with a cross (x) are compared to those obtained from an Nmag model of 2 real spheres (white centre ones) repeated along the y and z-axis using the MG approach.

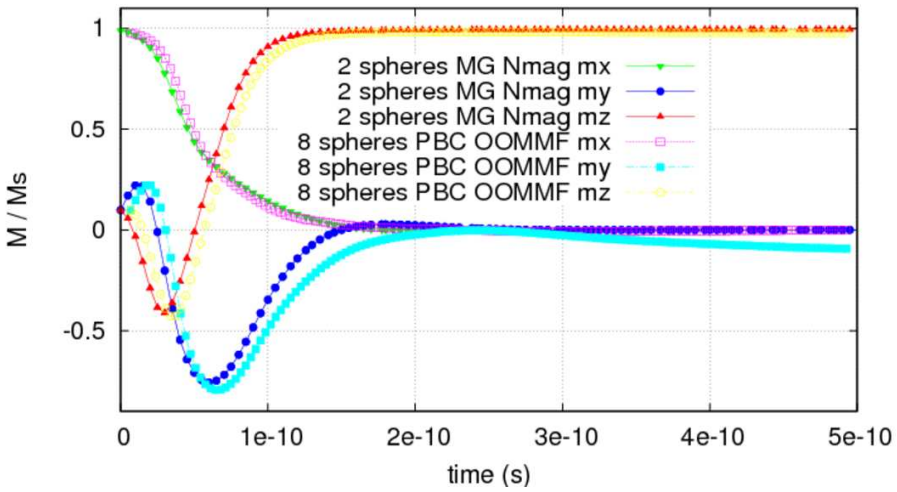


Figure 5.9: Relaxation of the magnetisation in the sphere marked with a cross in Figure 5.8. The primary cell in the Nmag system, made of the two spheres with a white centre in Figure 5.5, is repeated 4 times along the y-axis and 31 times along the z-axis using MG, while the OOMMF system is made of 8 real spheres with PBC along the z-axis.

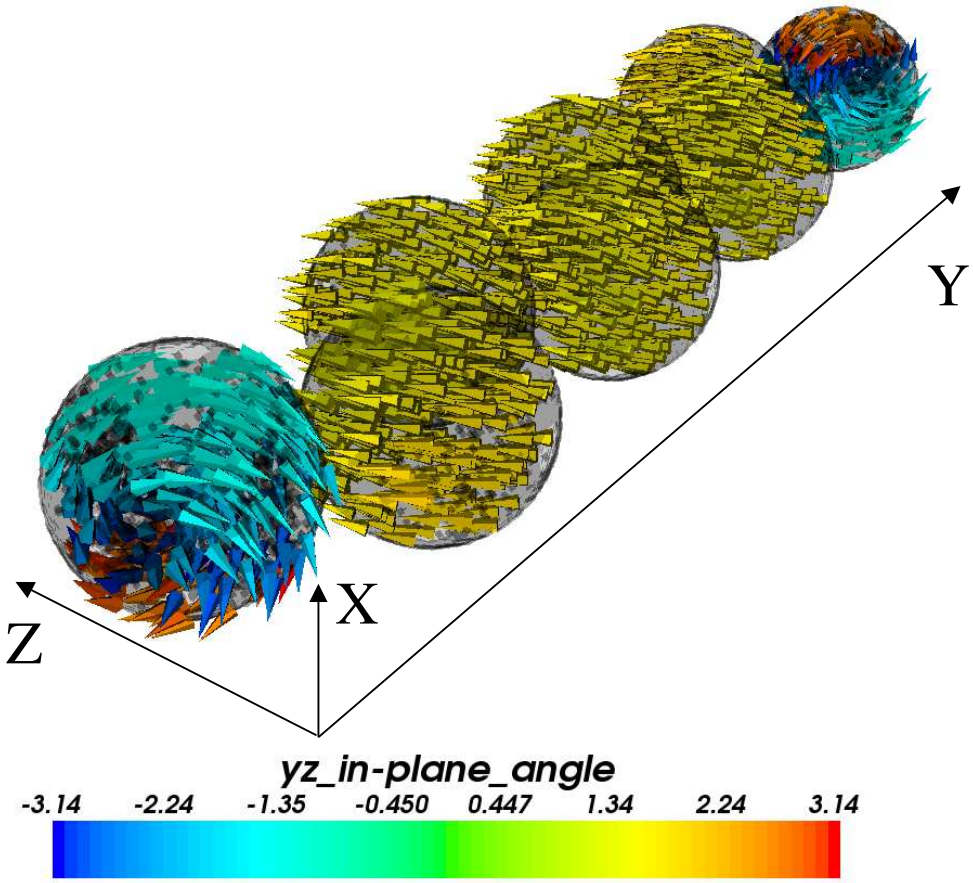


Figure 5.10: Equilibrium configuration of the OOMMF model with 8 spheres and PBC along the z-axis. Vortices appear in the outermost elements along the y-axis.

the size of the experimental sample be used, the OOMMF model with 8 real spheres is too big to be simulated and trying to follow the approach used for Nmag, that is to reduce the number of spheres and use PBC along the y-axis, does not work.

The reason is that OOMMF allows only one axis to be made periodic, so that the case of two spheres repeated 4 times along the y-axis and and infinitely periodic along the z-axis cannot be defined. Besides, the use of two spheres and PBC along the y-axis does not model correctly the full 2D system.

By contrast the Nmag model, using only 2 real spheres and an arbitrary number of quasi-periodic copies, does not have any constraint on the axes chosen to be quasi-periodic and, as Figure 5.9 shows, is able to describe very large systems without sacrificing the accuracy of the results.

## 5.5 Summary

We have introduced a novel approach to treat very large pseudo-periodic magnetic systems. The constraint on the magnetisation configuration, assumed to be the same for all the copies of the primary cell, is the same as that imposed by periodic boundary conditions, but with this approach, called macro geometry approach, the information about the overall shape of the sample is preserved.

The method is derived from the FEM/BEM described in Chapter 3 and its accuracy is tested in 1D and 2D systems.

Concerning 1D systems, the method is initially tested computing the demagnetising field at the centre of a ferromagnetic prism as a function of its length. When the magnetisation is uniform and aligned with one of the main axes, the value of the demagnetising field has a direct relation with the demagnetising factors of the geometry. These values are compared to a second set of values obtained using the analytical expression for prisms and we show the good agreement between the two sets.

Going to 2D systems, we studied the magnetisation relaxation in an array of spheres arranged on a hexagonal lattice and confined along one dimension. Initially a simplified version of the system is modelled in Nmag using two spheres repeated 4 times by means of the macro geometry approach. This model is compared to an OOMMF model using 8 real spheres, corresponding to the full set of elements along the confined dimension of the original system.

We show that there is no significant difference between the Nmag and OOMMF relaxation curves of the system, confirming that in this low-dimensional case the macro geometry approach describes the true system with an high degree of accuracy.

We also show that an OOMMF approach similar to the Nmag one, where instead of

a primary cell of two elements repeated 4 times the OOMMF model uses a primary cell of two elements with periodic boundary conditions, reproduces the reference system with lower accuracy with respect to the macro geometry model.

As the simulation of the full 2D system is beyond practical limits, we approximated it with an OOMMF system of 8 spheres and periodic boundary conditions. In this system the relaxation of the magnetisation from an out-of-plane direction has been compared to that obtained from the macro geometry model using two spheres as primary cell and $31 \times 4$ pseudo-periodic copies, enough to mimic the size of the original system.

We show that also in this case the difference in the magnetisation evolution between the two models is very limited despite their significant difference. This is a confirmation that the macro geometry concept implemented in Nmag is very effective in studying large finite quasi-periodic systems. Due to the limitation of the periodic boundary conditions approach large systems of this type are impossible to model correctly with OOMMF, while the ability of Nmag to define the number and position of the pseudo-periodic copies of the primary cell offers a high flexibility on the size of the systems to be studied.

A further advantage of the macro geometry approach implemented in Nmag over the periodic boundary conditions approach implemented in OOMMF is the simulation time of the investigated systems. Using 8 real spheres (both in Nmag and OOMMF) to simulate the system of Fig. 5.8 (with the white spheres obtained by the MG and the PBC approach, respectively) the simulation time on a machine with an AMD Athlon Dual Core processor and a frequency of 2 GHz is about 6 hours for Nmag and more than 5 days for OOMMF.

# Chapter 6

# Numerical studies of demagnetising effects in triangular ring arrays

The work described in this chapter has been published as a paper in the Journal of Applied Physics [70].

## 6.1 Introduction

As mentioned in Sec. 2.9.1 the continuing increase in areal density of data storage devices requires a new approach in the manufacturing of the recording media. Bit-patterned media (shown in Figure 6.1) have the potential to overcome the super-paramagnetic limit of conventional continuous media, and in Sec. 2.9.2 we have seen that MRAM is one of the most promising applications of such technology.

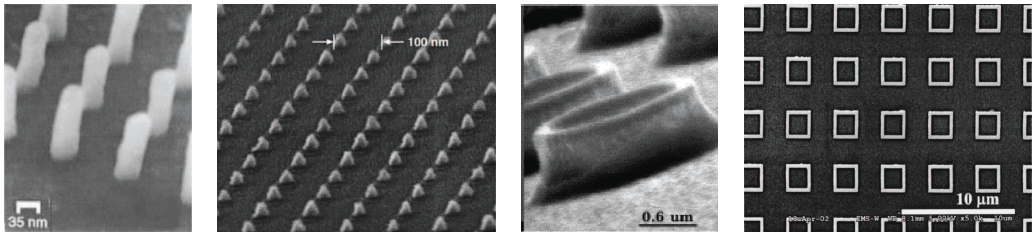


(a) (b) (c) (d)

Figure 6.1: Examples of bit patterned media: (a) array of nanopillars (reproduced from [71]), (b) array of pyramids (reproduced from [72]), (c) array of circular rings (reproduced from [73]) and (d) array of square rings (reproduced from [74]).

Besides nano-pillars, widely studied for their simple design and the possibility to obtain large current densities, thus creating a strong spin-torque effect, another potential geometry studied for MRAM applications is represented by ring elements [75]. The major advantages of these elements over other geometries are the limited number of stable magnetic states, the simple and uniform switching between such states and the weak magnetostatic interaction between neighbour elements when arranged in arrays. Despite these characteristics, imperfections in the manufacturing process can have important effects on their magnetic properties, especially concerning circular ring elements [76].

The introduction of notches or pinning centres can ease this problem [77] but their fabrication in small rings could present a technological challenge [78]. An alternative solution is the use of triangular ring elements, where the pinning centres are an intrinsic characteristic of the geometry and allow to have an high control on the possible magnetic patterns [79].

In such geometries, however, the intensity of the stray field is not as small as in circular rings, and magnetostatic interactions between elements can have a relevant effect on their magnetic behaviour. The interactions, which depend on the dipolar character of the magnetic configurations, typically start to become relevant when the distance between the elements is comparable to their size, and the result is a spread of the magnetic properties as measured on isolated elements.

As the stray field intensity follows a $1/r$ law, when the elements are closely packed the magnetic behaviour of a generic element could be significantly affected by the magnetic configuration of its neighbours. The extreme case is represented by a collective switching of elements, an uncontrollable situation where a single switching element triggers the switching of its neighbours, with the consequent loss of their independent behaviour.

The properties of isolated triangular rings have received increasing attention (*e.g.* [80, 79, 81, 82, 83]) but experimental studies of magnetostatic effects between ring elements are limited to circular ring arrays (*e.g.* [84, 85]). In order to gain a better understanding of the magnetostatic effects in arrays of interacting triangular rings, in this chapter the effect of magnetostatic interactions in a triangular ring array is investigated numerically as a function of the spacing between the elements and the number of elements used in the array.

## 6.2 Bit storage in triangular rings

Depending on the magnetic configurations assumed during the magnetisation reversal, triangular rings can be used to store a bit of information in two ways. If the magnetisation reversal occurs through closure patterns like those in Figure 6.2(a) or (b), the clockwise

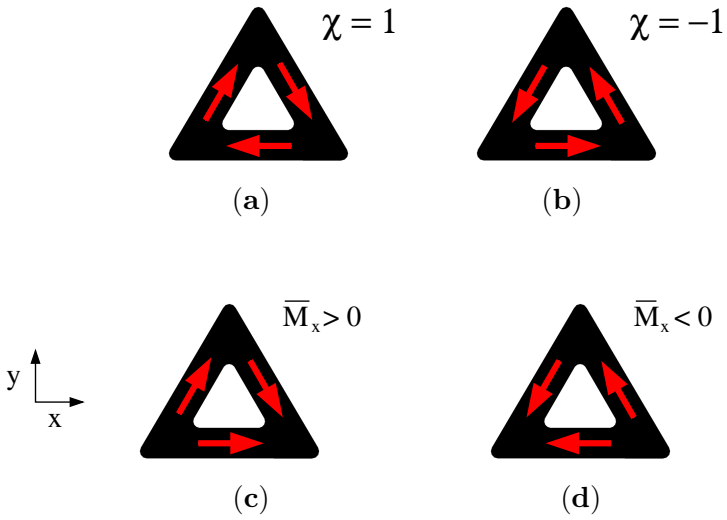


Figure 6.2: Bit storage in triangular ring elements. If the magnetisation configuration at remanence assumes a vortex pattern, the logic 0 and 1 can be encoded by the orientation of the magnetisation as in (a) and (b). If the magnetisation configuration shows a dipolar character, the component of the dipole along a particular direction can be used instead.

or anti-clockwise chirality can be controlled by the direction of the applied field [79], and the orientation of the resulting vortex can be used to encode the logic 0 or 1.

Experimental evidence of vortex states during magnetisation reversal has been shown for rings with lateral size larger than a micrometre [79, 82]. At this size possible configurations with dipolar character (*i.e.* non-closure of magnetic flux) are penalised by the dipolar interaction occurring between the sides of the ring, and the configuration of minimum energy at remanence is represented by the vortex state. Elements characterised by vortex configurations are particularly suitable for bit patterned media applications, since the small stray field produces negligible magnetostatic effects on neighbour elements.

However, going to smaller element sizes the shape anisotropy and exchange energy overtake the dipolar energy as the main drivers of the magnetisation evolution and the configuration at remanence may show a dipole-like behaviour. Simulations of 50 nm size elements show such behaviour when the field is applied along one of the sides of the ring. With this arrangement the magnetisation in the other two sides is always misaligned with respect to the field direction and a net dipole moment is created along the direction of the side parallel to the applied field.

Although the orientation of this dipole can be used to encode two logical bits as shown in Figure 6.2(c) and (d), the stray field associated to these configurations is stronger than that created by a vortex state and coupling effects between neighbour elements may be present even for relative large distance between them.

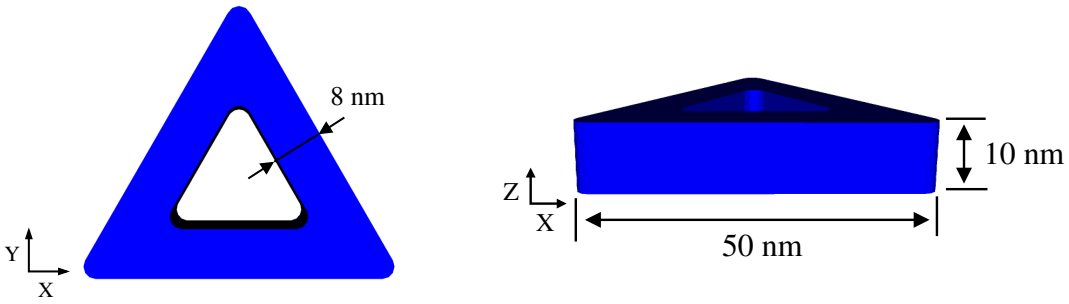


Figure 6.3: Geometric characteristics of a triangular ring.

## 6.3 Computational Model

To study the extend of these coupling effects in arrays of magnetic elements a common approach is to consider one element of the array, to take the remanent magnetisation $M_{\mathrm{r}}$ and coercive field $H_{\mathrm{c}}$ as the characterisation parameters, and analyse how these parameters are affected by changing the configuration of the array [86, 87].

We use the values of $M_{\mathrm{r}}$ and $H_{\mathrm{c}}$ of an isolated ring as those associated to an ideal behaviour of the elements, and follow this approach to show how these values change as a function of the spacing between the elements and the number of elements used in the array.

Figure 6.3 shows the geometric characteristics of the triangular rings used as array elements. Each ring is an equilateral triangle with a lateral size of 50 nm, edge width of 8 nm and a thickness of 10 nm. The size is chosen in order to match the current limit of areal density of information in hard disk drives, of the order of 200 Gbit/in$^2$.

To investigate possible magnetostatic effects between these rings we use an array where the elements are placed on a square lattice with the same periodicity $p$ for the $x$ and $y$ directions (see Figure 6.6). The periodicity $p$ varies between 53 nm and 150 nm, which correspond to an inter-element distance between 3 nm and 100 nm. We use arrays of triangular rings with up to $11 \times 11$ elements. In the following we will show that this is a good approximation of a much larger array.

As we are interested in the magnetic properties induced in the material by its geometry, the presence of crystalline anisotropy may have undesirable effects on the magnetic behaviour. Therefore the material used for the triangular rings has zero magnetocrystalline anisotropy and we used Permalloy with the following magnetic parameters: exchange coupling constant $A = 1.3 \cdot 10^{-12}$ J/m and saturation magnetisation $M_{\mathrm{s}} = 860 \cdot 10^3$ A/m.

Concerning the simulation of the triangular ring array, a slight misalignment between

the field direction and the symmetry axes of the geometry is commonly introduced. This is done to avoid possible numerical artifacts in the magnetic configurations, and in the present case the external field is applied in-plane roughly along the x-axis, tilted off by 0.1 radians ($\sim 5.7°$) in the x-y and x-z planes.

## 6.4 Isolated ring

The hysteretic behaviour of an isolated ring is shown in Figure 6.4. Starting from an applied field of $10^6$ A/m, corresponding to the saturated magnetisation distribution in Figure 6.5-I, the field is decreased in steps of $5 \cdot 10^3$ A/m. At remanence (Figure 6.5-II) the magnetisation bends on the top corner and bottom edge to reduce the demagnetising field from surface charges on the lateral edges. The lateral corners L and R in Figure 6.5-I act as pinning centres around which the magnetisation rotates. The angle $\alpha$ of the magnetisation at these corners goes from 0° at saturation, to 30° at remanence and reaches 60° right before the switching. The coercive field is $H_c = 157.5 \cdot 10^3$ A/m, corresponding to 198 mT, while $M_r = 0.858\ M_s$.

The switching mechanism occurs without the intermediate vortex states found in larger rings [81]. The out-of-plane component of the magnetisation is largest at the top corner of the ring. At $H_c$ this corner acts as a nucleation region and the magnetisation reverses simultaneously over all the ring.

## 6.5 Computation of the demagnetising field

As described in Chapter 3, the computation of the demagnetising field is the most demanding part of a micromagnetic simulation.

To compute the demagnetising field we used the macro-geometry approach explained in Chapter 5 where, as a result of the Finite Element/Boundary Element Method described in Sec. 3.4.2, the size of the Boundary Element Matrix (BEM) is proportional to the square of the number of surface nodes $N_s$ in the meshed geometry. Therefore, if the system is made of a series of identical objects as in our array, the size of the BEM increases quadratically with respect to their number.

Considering that the memory requirement for a single ring simulation is of the order of 22 MB, such behaviour may limit the simulation of an array of triangular rings to a very few elements.

A method to simulate a large number of elements does however exist, and is based on the assumption of identical magnetisation in all the rings of the simulated array.

Considering the array of $5 \times 5$ elements in Figure 6.6, and calling $N_r = 5$ the number

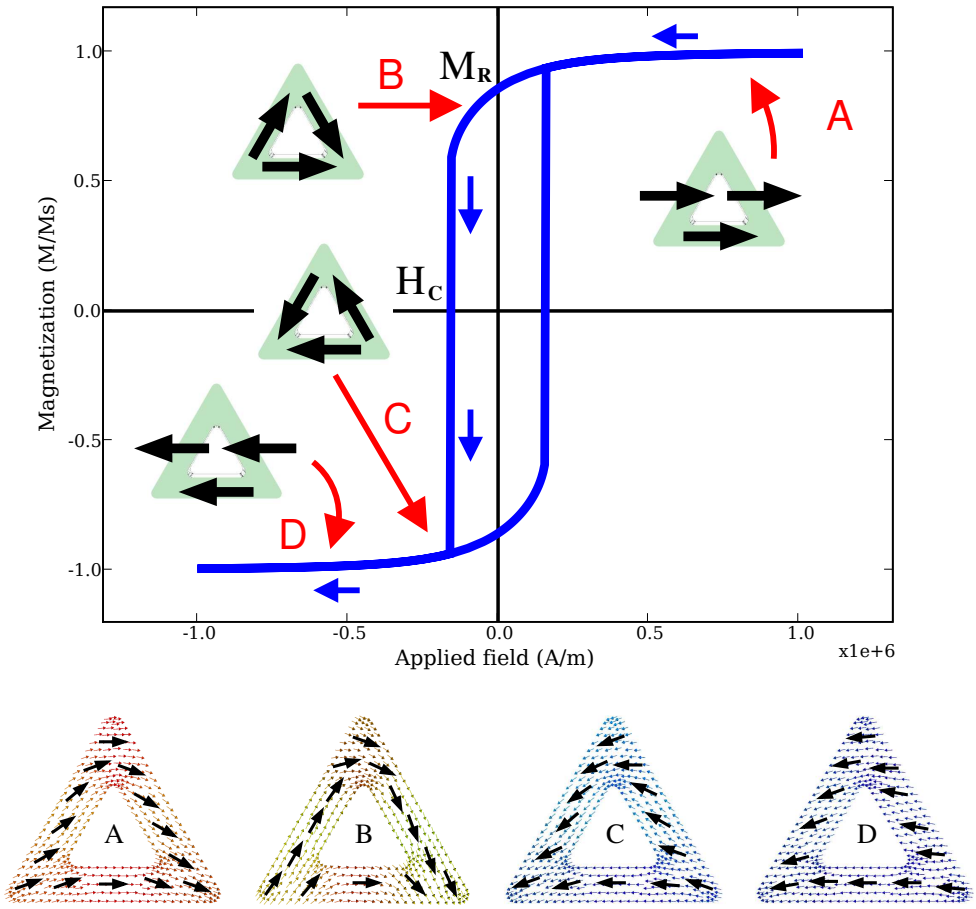


Figure 6.4: Hysteresis curve of an isolated ring. The magnetisation distribution over the ring, shown by black arrows, is shown in more detail for the key points in the 4 rings below.

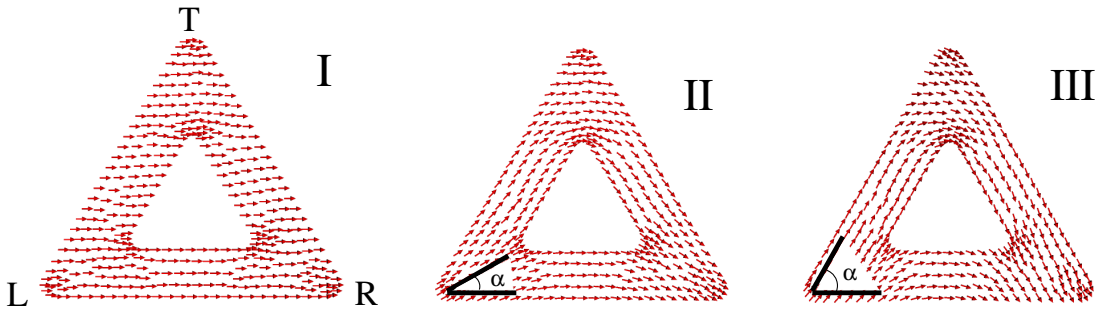


Figure 6.5: Bending angle $\alpha$ of the magnetisation at the lateral corners L and R going from the saturation configuration (I) to the remanence (II) and the coercive field (III) in Figure 6.4. The reversal is driven by the magnetisation in the top corner T, where the out-of-plane component is largest.

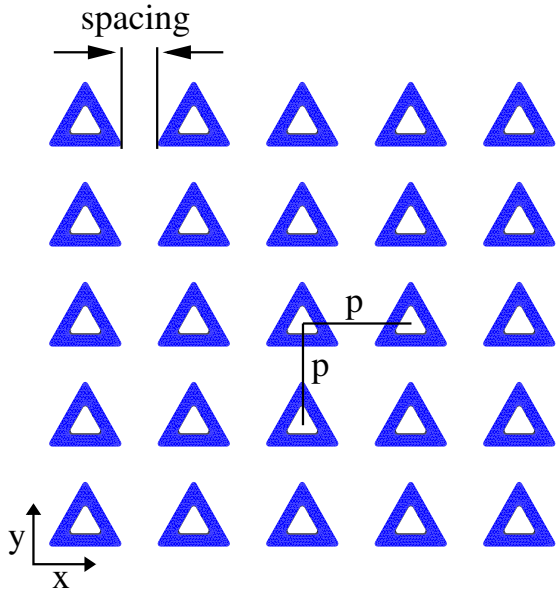


Figure 6.6: Geometric characteristics of a $5 \times 5$ array with periodicity $p$. The applied field is directed roughly along the x-axis, tilted by $\sim 5.7°$ in the x-y and x-z planes.

of rows of the square lattice, this technique is used to study the behaviour of the central triangular ring under the magnetostatic field of the $(N_r^2 - 1) = 24$ other triangular rings and an applied field in the following way.

The magnetisation for the 24 outer rings is computed using a method based on the macro geometry approach for quasi-periodic systems introduced in Chapter 5. Starting with an initial large field pointing in the $x$-direction, which corresponds to a saturate configuration for all the rings, the magnitude of the applied field is gradually reduced to zero and the magnetisation, enforced to be identical in all the rings through the macro geometry approach, evolves towards the remanent state. For all the periodicity values considered the final configuration of each ring is virtually identical to the remanent magnetisation of an isolated ring shown in Figure 6.5-II. As all rings have the same magnetisation, this configuration will overestimate the demagnetising field because the rings do not have the freedom to react individually.

At this point the magnetisation in the outer rings is kept fixed and their demagnetising field is used as an additional field in the simulation of an hysteresis loop for the central ring.

## 6.6 Effect of periodicity

As introduced in Sec. 6.3 the variation of the remanent magnetisation and coercive field as a function of the periodicity $p$ is studied using an array of 121 elements on a $11 \times 11$ square lattice.

The periodicity $p$ (see Figure 6.6) varies between 53 and 150 nm, corresponding to spacings between 3 and 100 nm between the rings. The reversal mechanism for the central ring under the influence of the outer 120 rings is uniform rotation (the same as that of the isolated ring) for nearly all values of $p$. Only for $p = 53$ nm, *i.e.* a 3 nm spacing between neighbour elements, the reversal goes through an intermediate state where the magnetisation assumes an out-of-plane configuration in the left corner of the ring (see Figure. 6.7).

To evaluate the approximation of using a fixed magnetisation for the outer rings, we tested the effect of the magnetisation evolution, under an external applied field, in the central ring of the 121-elements array on one of its first neighbours. The starting configuration is the remanent state, identical in all the rings, described in the previous section. Using this initial configuration an external field is applied to the central ring of the array, while the constraint of fixed magnetisation is relaxed on the closest ring on its left.

With this configuration the magnetisation in the neighbour ring is affected by the

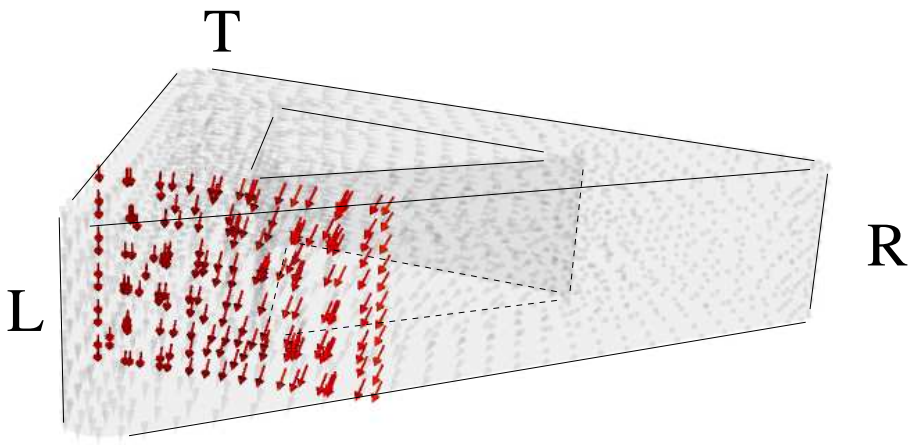


Figure 6.7: Out of plane magnetisation of the central ring for a periodicity $p = 53$ nm between the rings. The letters are used to identify the corners of the ring as left (L), top (T) and right (R).

magnetisation evolution of the central ring. The interaction occurs via the variation of the demagnetising field in the surrounding space, and the analysis of their hysteresis loops is used to estimate the error in the fixed magnetisation approximation for the outer rings.

The system is shown in Figure 6.8, where the distance between the rings is 3 nm (which corresponds to the smallest value of the periodicity, $p = 53$ nm) and the external field is applied only on the right one (assumed to be the central ring of the $11 \times 11$ array).

The magnetisation evolution during an hysteresis loop of the right ring ( Figure 6.9(b) ) induces a small variation of the magnetisation in the left one ( Figure 6.9(a) ). Looking at the scale on the y-axes, the range of the magnetisation in the hysteresis curve for the left ring is about 100 times smaller than that of the right ring. This result indicates that the magnetisation in the first neighbour rings is almost independent of the magnetisation evolution in the central one, and the assumption of fixed magnetisation for the second, third, ... n-th neighbour rings is therefore a good approximation when computing the magnetostatic field from the whole array.

This simulation also shows the asymmetric way the evolution of the magnetisation in the central ring affects the magnetisation of the neighbours. The explanation can be found looking at the simplified model of Figure 6.10.

When the magnetisation in the central ring is "aligned" with the rest of the array as in Figure 6.10(a), the neighbour ring experiences a demagnetising field which is relatively small for the presence of magnetic charges (on all neighbour elements) of opposite sign at close distance from its own surface charges. In this case the effect on the magnetisation within the ring is to have magnetisation patterns which are relatively independent of the

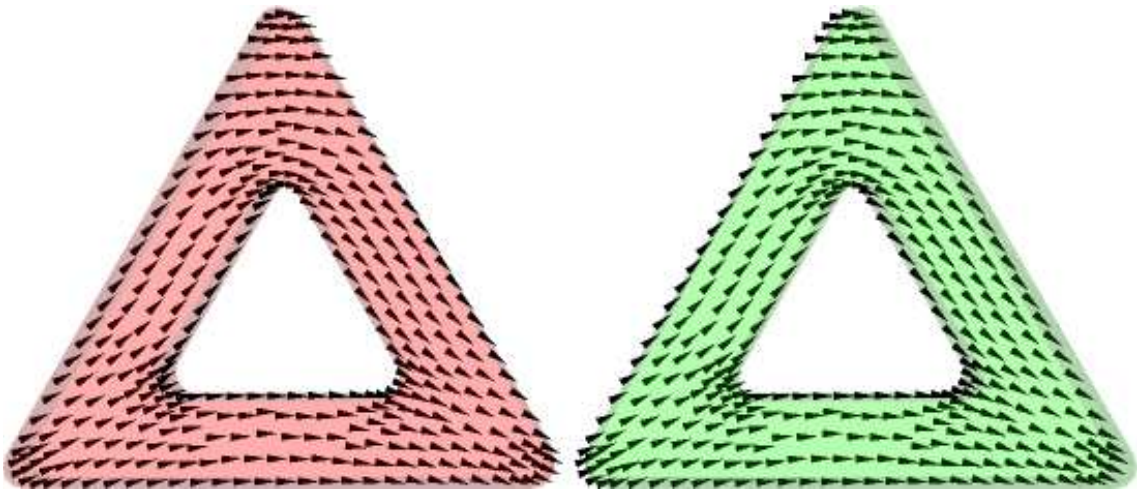

Figure 6.8: Test of fixed magnetisation approximation in the outer rings. The external field is applied on the central ring of the $11 \times 11$ array (green one, on the right) and the magnetisation in the neighbour ring (red one, on the left) reacts to the magnetisation evolution in the central ring.

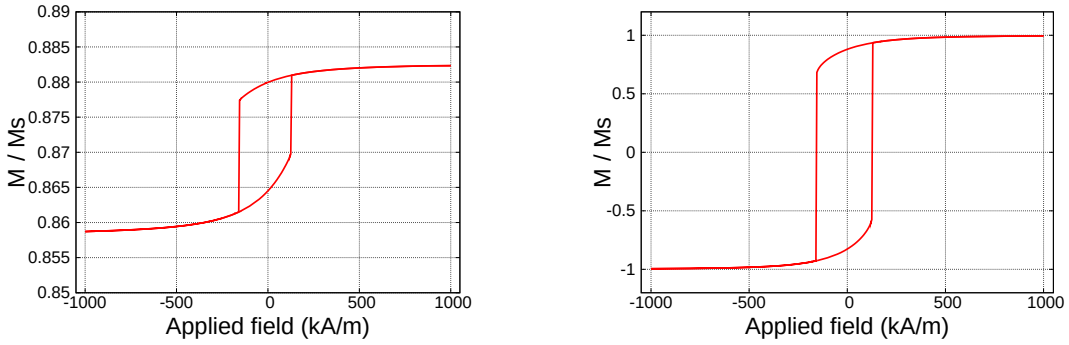


(**a**) (**b**)

Figure 6.9: Hysteresis curves for the central ring of the $11 \times 11$ array (b) and hysteresis curve for the nearest neighbours on its left (a). The range of the magnetisation in the hysteresis curve for the ring in (a) is about 1% of the curve for ring in (b), supporting the assumption of fixed magnetisation for the outer rings.

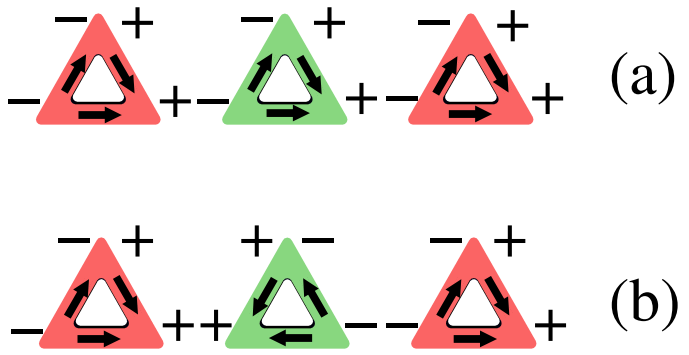


Figure 6.10: Simplified model of magnetisation patterns: (a) with the magnetisation in the central ring (green) "aligned" with the rest of the array; (b) with the magnetisation in the central ring "anti-aligned" with the rest of the array.

shape of the ring, and the consequence is the relatively flat slope of the top part of the hysteresis curve in Figure 6.9(a).

On the other hand, when the magnetisation in the central ring is "anti-aligned" with the rest of the array as in Figure 6.10(b), the neighbour ring experiences a stronger demagnetising field due to the addition of magnetic charges of same sign as its own surface charges on the side towards the central ring. The effect is to have a stronger demagnetising field experienced by the neighbour ring with respect to the previous case, and the associated increased tendency of the magnetisation to follow the ring shape results in the increased slope of the bottom hysteresis curve in Figure 6.9(a).

Going back to the simulations with the whole $11 \times 11$ array, the outcomes are shown in Figure 6.11. Here the remanent magnetisation and coercive field are shown as a function of periodicity $p$. The line with circular marks shows that the coercive field $H_c = 157.5 \cdot 10^3$ A/m of the isolated ring ($p = \infty$) is maintained for values of $p$ of 150 nm, 100 nm and 80 nm. Considering that the latter value corresponds to an inter-element distance of 30 nm, and the size of the elements is 50 nm, this result can be interpreted as the relatively low dipolar character of the magnetisation in the rings. For smaller values of $p$ the magnetostatic interactions affect the switching point of the ring and the magnitude of $H_c$ decreases up to $127.5 \cdot 10^3$ A/m (corresponding to 160 mT) at periodicity $p = 53$ nm.

Concerning the remanent magnetisation $M_r$ (line with square marks), a deviation from the isolated ring case is present for all finite values of $p$. The largest difference, of about 4%, occurs at $p = 53$ nm, where $M_r = 0.825\ M_s$. At $p = 80$ nm, where the deviation of $H_c$ from the ideal case (isolated ring) is negligible, the deviation of $M_r$ from the ideal case is below 1%. Assuming that a 1% difference in $H_c$ and $M_r$ can be taken as a good

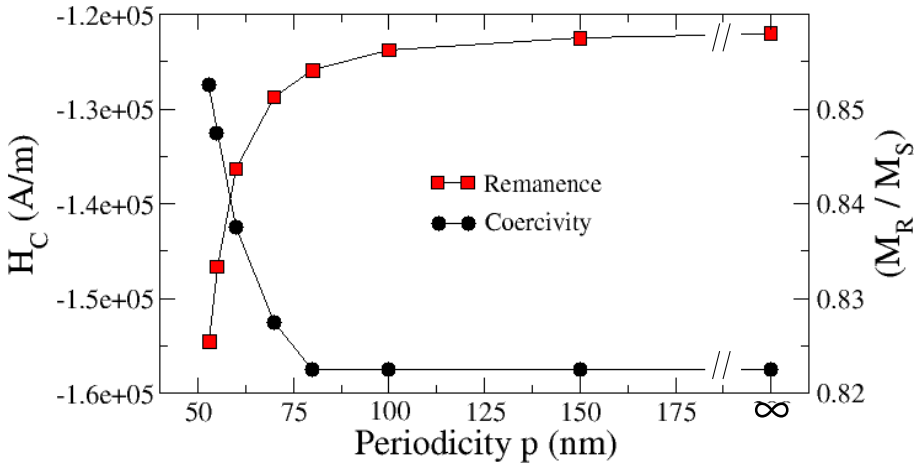


Figure 6.11: Coercive field and remanent magnetisation as a function of the array periodicity. The values for an isolated ring are those with $p = \infty$.

approximation of the ideal behaviour, we deduce that a spacing of 30 nm is the limit for an independent behaviour of the rings.

## 6.7 Reduced array

Carrying out the simulations of the array of rings is more demanding in required execution time than that of an isolated ring, while the memory requirements are the same (by using the method explained in Sec. 6.5).

This extra time effort is proportional to the number of periodic copies, and since the BEM matrix must be computed for each periodic copy, it is also proportional to the square of the number of surface nodes in the mesh of one ring (which determines the size of the BEM matrix). In order to minimise the setup time of the simulation it is then interesting to know which is the minimum size of the array which guarantees a good approximation of the truly periodic system.

To answer this question we consider the set of square arrays ranging from $3\times3$ to $11\times11$ elements, and compare their $H_c$ and $M_r$ values. For all the periodicities $p$, the coercive field and remanent magnetisation of the largest array ($11 \times 11$ elements) is assumed to be the best approximation of the truly infinite case and is therefore taken as the reference value.

The simulations show that reducing the number of elements of the array, the magnetic behaviour for different values of $p$ is qualitatively similar to the largest system considered ($11 \times 11$ elements).

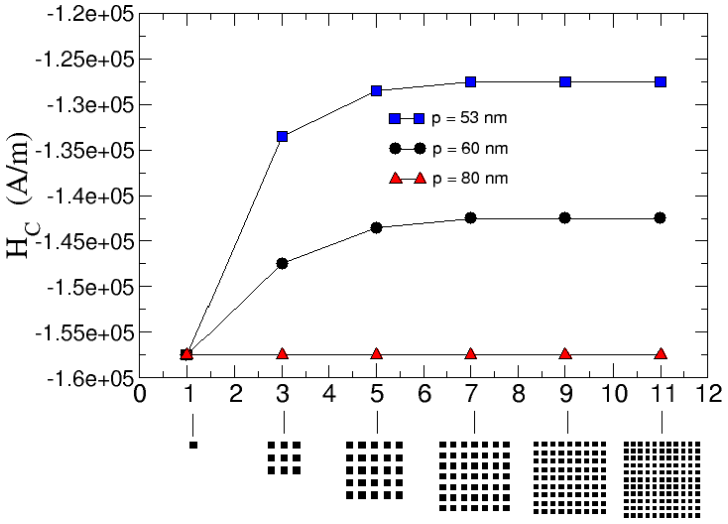


Figure 6.12: Coercive field of reduced arrays as a function of their lateral size (expressed by the array dimension on the x-axis) and the spacing between the elements (expressed by the three curves in the main graph).

Concerning the coercive field, the values of $H_c$ as a function of the array size are shown in Figure 6.12, where only the curves for periodicity values going from 53 nm to 80 nm are displayed. The curves associated to periodicity values larger than 80 nm, missing in the graph, are coincident with the 80 nm one.

The graph shows that the number of lateral elements needed to reproduce the periodic behaviour (associated to the value of the $11 \times 11$ array) increases going from 30 nm to 3 nm spacing (corresponding to $p$ ranging from 80 to 53 nm). In fact with a periodicity $p = 80$ nm between the elements the value of the coercivity is the same for a single ring case and a $11 \times 11$ array of rings (the "periodic" case), while for a distance of 60 and 53 nm between the elements an array of at least $5 \times 5$ elements is needed to have a coercivity value within 99% of the "periodic" value.

As shown in Figure 6.13, in the case of the remanent magnetisation the value obtained reducing the size of the array is always larger than the reference value (associated to the $11 \times 11$ array), but an array size as small as $3 \times 3$ elements is sufficient to have a deviation within 99% of the periodic value for all the $p$ considered.

Assuming that a 1% difference in $H_c$ and $M_r$ can be taken as a good approximations of the periodic behaviour, we have found that a $5 \times 5$ array is sufficient to have the same coercivity value $H_c$ of a periodic array. On the other hand, a similar result is achieved with a $3 \times 3$ array when considering the values of the remanent field $M_r$ . The overall conclusion is therefore that the effect from first and second nearest neighbours in a square

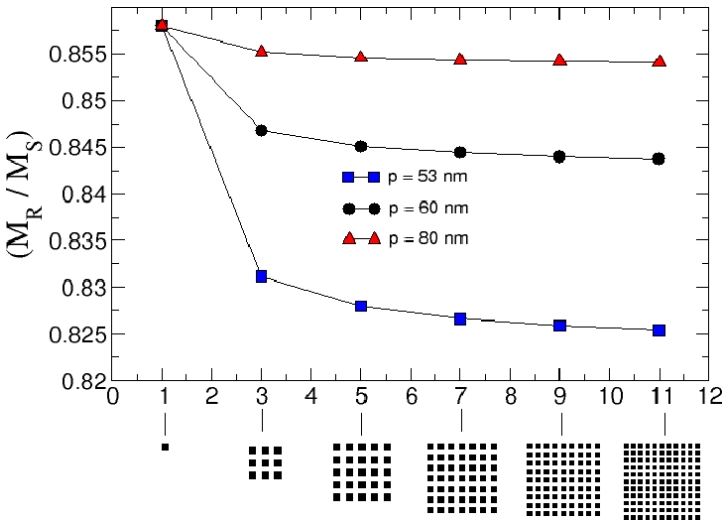


Figure 6.13: Remanent magnetisation of reduced as a function of their lateral size (expressed by the array dimension on the x-axis) and the spacing between the elements (expressed by the three curves in the main graph).

array of triangular elements is a good approximation of a much larger array.

## 6.8 Summary

As we have seen in Chapter 2, a promising technology to overcome the limitations of conventional magnetic recording media is represented by bit-patterned media, with MRAM being one of their most popular applications. Nano-pillars and nano-rings have been widely studied as potential array elements for MRAM devices: nano-pillars have the advantage of a simple design and the possibility to obtain large current densities, thus creating a strong spin-torque effect, while the qualities of ring elements are a limited number of stable magnetic states, the simple and uniform switching between such states and the weak magnetostatic interaction between neighbour elements when arranged in arrays.

Focusing on ring elements, imperfections in the manufacturing process can have important effects on their magnetic properties, a problem reduced with the use of notches or pinning centres in the elements. On this respect, the pinning centres intrinsic in the geometry make triangular rings to be the logical choice in terms of packing factor, available stable states and control of magnetic patterns.

However, in closely packed arrays magnetostatic interactions can have a relevant effect on the magnetic behaviour of single elements, a major constraint in the density of information that can be stored in these devices. To have a quantitative estimate of these

interactions, the effect of the demagnetising field in a square array of 50-nm size triangular elements has been investigated.

Taking the value of the coercivity $H_c$ and remanent field $M_r$ of a central element as the characterisation parameters, the effects of the interactions for different array configurations are analysed comparing these values to those of an isolated ring.

The results are obtained assuming that all the rings of the array have the same static magnetisation configuration (their remanent state), a consequence of the macro geometry approach used in the modelling of the micromagnetic system.

Even if this assumption overestimates the demagnetising field (because the rings do not have the freedom to react individually), the fixed magnetisation in the outer rings is a good approximation of the real effect when an external field is applied on the central ring.

Under these conditions a spacing of 30 nm between the rings along the two main axes of the square array is sufficient to have a deviation smaller than 1% between the behaviour of an isolated ring and that of the central ring of the array. Since the size of the elements is 50 nm, this result can be interpreted as the relatively low dipolar character of the magnetisation in the rings.

A separate analysis has been done to find how the number of elements in the array affects the magnetic properties of the central ring. Starting from $121 \times 121$ elements, sufficient to consider the model as a truly periodic system, the number of elements has been progressively reduced up to an array of $3 \times 3$ elements. Plotting the values of $H_c$ and $M_r$ obtained for the central ring as a function of the array size we found that $5 \times 5$ elements are sufficient to have the same effect of the largest array, since the deviation in $H_c$ and $M_r$ between $5 \times 5$ and $11 \times 11$ elements is below 1% for all the inter-element spacings considered.

Therefore we can conclude that with a distance of 30 nm between the elements each ring can be considered as behaving independently from the others, and the limited effect of the magnetostatic interactions is mostly due to first and second nearest neighbours.

# Chapter 7

# Analysis of anisotropic magneto-resistance in arrays of connected nano-rings

The work described in this chapter has been published as a paper in the IEEE Transactions on Magnetics [88].

## 7.1 Introduction

In the previous chapter we have seen that the interactions between neighbour elements in a periodic array of nano-rings can have a relevant effect on the magnetic properties of the single rings when the elements are closely packed. The investigation of these interactions, useful to find the limits on the density of information in patterned media applications, can be extended to the case of a connected rings array. This approach, besides maximising the interactions between the rings, introduces an anisotropy in the system by connecting the elements along the x and y directions; in experimental results on circular rings this leads to a dependence of the coercive field on the angle of the applied field, where at any given angle a spread of values is observed [89].

In this chapter a numerical investigation of the magnetic and transport properties of a connected rings array is presented, and the results are used to gain insight about the magnetisation patterns and switching processes of the rings. The numerical results in Sec. 7.5 explain the experimental data obtained from the sample in Sec. 7.3 and the comparison in Sec. 7.6 between a numerical approach with a varying current distribution and the so called uniform current model shows the importance to correctly compute the current distribution when deriving the Anisotropic Magneto-Resistance (AMR) of the sample.

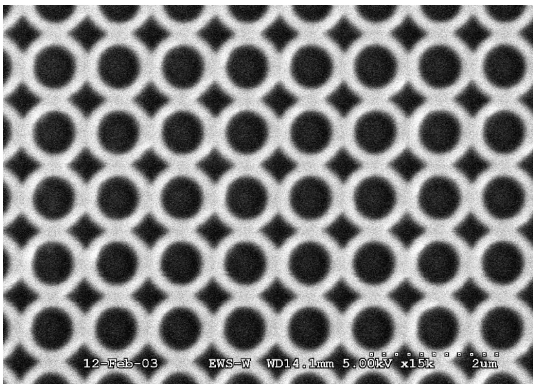


Figure 7.1: SEM image of the connected rings array (reproduced from [90]).

## 7.2 Anisotropic magneto-resistance

The Anisotropic Magneto-Resistance (AMR) is a property of ferromagnetic metals first discovered by William Thomson in 1857 [91]. This effect consists in a variation of the resistance of a ferromagnetic sample when placed in a magnetic field, where the variation shows a dependence on the angle between the magnetisation $\mathbf{M}$ and the direction of the electric current. Defining the resistivity $\rho$ as

$$\rho = \frac{E}{J} \tag{7.1}$$

with $E$ the electric field and $J$ the current density, the phenomenological dependence of the resistivity from the angle $\theta = \angle(\mathbf{M}, \mathbf{J})$ is given by

$$\rho(\theta) = \rho_0(1 + \alpha \cdot \cos^2 \theta) \tag{7.2}$$

In this equation $\rho_0$ is the resistivity of the material at zero applied field and $\alpha$ is a temperature dependent coefficient that can take positive and negative values. In the case of permalloy, the material used for our array, $\alpha$ takes positive values between 1% and 5% and the net effect is to have maxima in the resistivity when the local magnetisation $\mathbf{M}$ is parallel or anti-parallel to the local electric current $\mathbf{J}$.

The origin of the positive and negative variation of the resistance with respect to the value at zero applied field has been a long-standing problem, and it took almost a century since the discovery of Thomson before Robert Potter could eventually explain it, based on early work by Nevil Mott and Jon Smit.

The contribution of Mott came from the attempt to explain the decrease in resistivity of ferromagnetic metals when brought below their Curie temperature. Mott developed the

so-called two-current model [92] where the current, experimentally verified as mostly due to electrons in $s$ orbitals, can be separated in two streams of majority and minority spin electrons.

Defects, phonons and imperfections in the crystal lattice make the conduction electrons scatter between different states but, as the scattering potential does not depend on the spin, Mott assumed that there is no spin transition during scattering events. The current is effectively polarised and the conductivity can be expressed as the sum of two independent contributions.

Moreover, comparing the density of states at the Fermi level for $s$ and $d$ orbitals, Mott expected the majority of scattering to be of $s-d$ type rather than $s-s$, and the independence of the two spin-channels was associated to an independent transition rate in the two cases.

Although being able to explain the decreasing of resistivity below the Curie temperature by the different resistivity of the two channels, Mott's model could not explain the anisotropic characteristic of ferromagnetic metals.

The explanation of such property came with a model developed by Smit, who recognised the role of the spin-orbit interaction as a possible source of anisotropy [93]. Treating such interaction as a perturbation to the energy of the system, Smit deduced that the angle between the current (mainly due to $s$ electrons) and the magnetisation (mainly due to $d$ electrons) affects the transition rate of electrons between $s$ and $d$ orbitals, and thus the current. This approach was further developed by Potter [94], who eventually obtained a $\cos^2(\theta)$ dependence of the resistance on the angle $\theta$ between the current and the magnetisation when he assumed the magnetisation to be directed along one of the crystallographic axes and a nearly filling of the $d$ orbitals, typical of transition metal ferromagnets. With this model the sign of the parameter $\alpha$ in Eq. (7.2) is justified by the predominance of electrons with majority or minority spin as the current carriers, with the majority carriers being those with the largest density of states at the Fermi level.

## 7.3 The sample

Figure 7.1 shows a Scanning Elecron Microscopy (SEM) image of the connected nano-rings sample. Periodic square arrays of 25 nm thick permalloy nano-rings have been prepared by e-beam lithography on a (100) silicon wafer spin-coated with bi-layer resists (PMMA and P(MMA-MAA) copolymer). Using e-beam evaporation in a high vacuum, a permalloy film was deposited, and after a lift-off in acetone the arrays of magnetic permalloy rings were obtained. The elements are circular rings with internal and external diameters of 650 nm and 1100 nm, respectively, and the distance between their centres is 1000 nm.

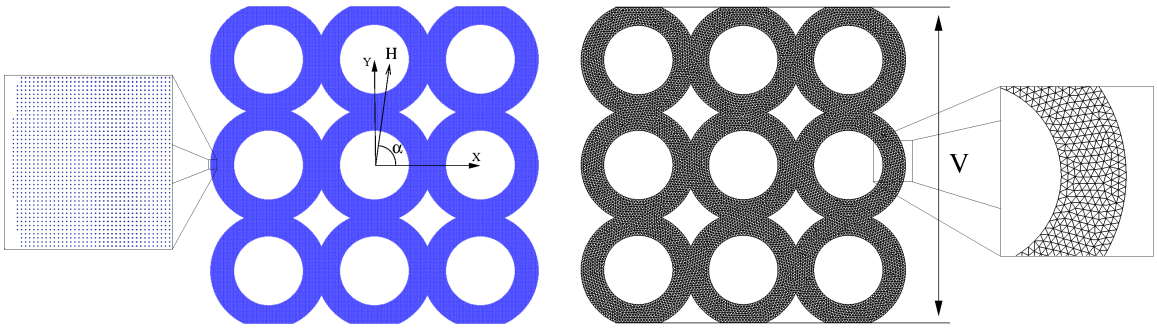


Figure 7.2: (a) Model used in the micromagnetic simulation of the connected rings array with OOMMF (the detail shows the fine regular mesh used with the finite differences approach). The external field **H** is applied nearly along the y-axis ($\alpha = 88°$); (b) Model used for the calculation of the AMR with Nmag (the detail shows the coarse triangular mesh used with the finite elements approach). The voltage $V$ is applied between the top and bottom edges of the system, with the contact regions along the cut rings.

## 7.4 Computational Model

The AMR effect, and in particular the resistivity distribution over the connected rings array, is used to study the transport properties of the array shown in Figure 7.1 when an external field is applied nearly along the y-axis. The magnetisation and current distributions, needed in the calculation of the angle $\theta$ in Eq. (7.2), are obtained using both OOMMF and Nmag.

For the micromagnetic modelling the use of OOMMF has been preferred to Nmag for the smaller memory requirements in the case of extended thin structures. This is because the memory requirement of Nmag scales as $N_s^2$, with $N_s$ the number of surface nodes of the mesh, compared to the $N_a \log N_a$ dependence of OOMMF, with $N_a$ all the nodes of the mesh; however, as we use a single layer of nodes in OOMMF, $N_a = N_s$.

With this choice the curved geometry of the sample requires a very fine grid to be resolved, and the undesired effect on the simulation time has led us to limit the numerical sample to the $3 \times 3$ ring array shown in Figure 7.2(a).

While the magnetisation data has been computed on the whole 3x3 ring system, to minimise surface effects of the magnetisation only the central ring has been used in the analysis of the conductivity. Surface effects, shown in Figure 7.3, are caused by the small size of the model as compared to the experimental sample. In some of the external rings the behaviour is dominated by the shape-induced anisotropy, with the magnetisation creating small vortices over limited zones of the rings or showing vortex states over entire rings.

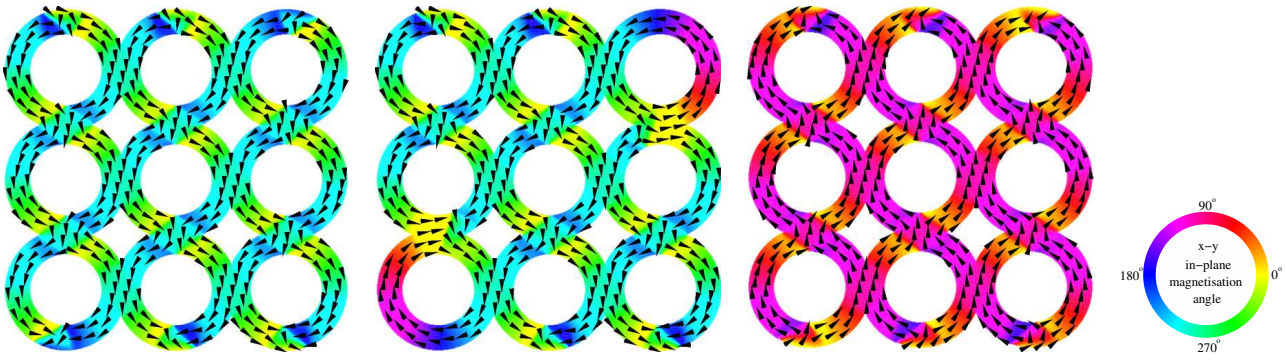


(**a**) (**b**) (**c**)

Figure 7.3: Intermediate states of an hysteresis loop of the computational sample. The small vortices appearing at the top and bottom boundaries of the array before (a) and after (c) the switching are due to surface effects of the magnetisation. The extreme case is the magnetisation configuration shown in (b), where at the boundaries entire rings can show a vortex state.

These configurations are "boundary" effects that are limited to relatively few rings in the experimental sample (which is 1 mm $\times$ 1 mm in size, and contains about $10^6$ elements where the surface elements are no more than few thousands), but account for 5/9 of the rings in our model.

In particular, the vortex state in the corner rings of Figure 7.3(b) is stable enough to prevent the occurrence of the magnetic patterns observed in all the other rings, possibly affecting the "bulk" behaviour in the modelled array. To reduce these surface effects a solution is the use of periodic boundary conditions along the y-axis of the sample. This approach gives the magnetic configurations in Figure 7.4 which, despite showing a larger switching field when compared to the non-periodic model of Figure 7.3(a)-(c), confirm the reduction of surface effects in the outer rings.

Despite the excellent performance for micromagnetic simulations, non-magnetic variables such as electric current and resistivity cannot be included in the OOMMF model, and the only way to perform an AMR analysis of our sample is to transform the data obtained from OOMMF into a format suitable for Nmag; because of the abstraction of the fields in the model, Nmag can deal with any kind of field defined on the mesh and therefore the electromagnetic modelling is not different from the micromagnetic done. The magnetisation distribution is then interpolated over an unstructured mesh with the same geometric parameters of the OOMMF grid and the current and resistivity fields are defined on the new discretisation points.

To study the AMR effect we compute the current distribution by fixing the voltage at the top and bottom interfaces of the system and solving a generalised Poisson equation for

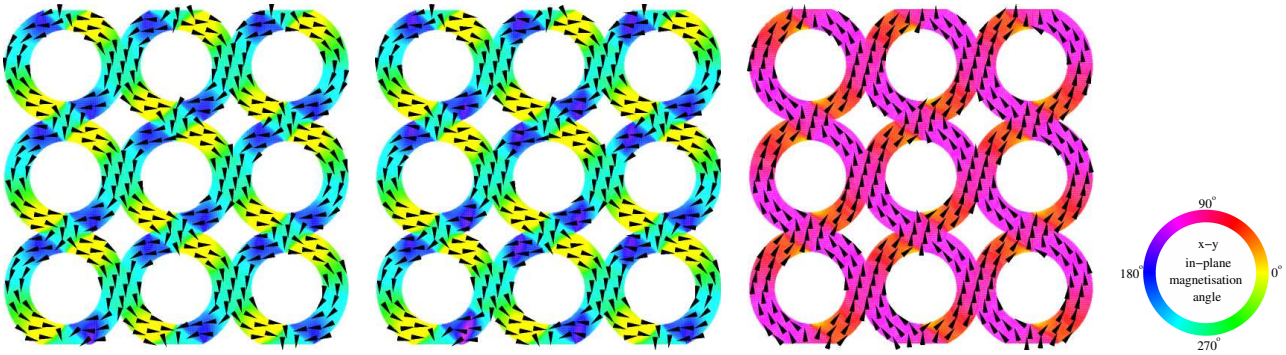


(**a**) (**b**) (**c**)

Figure 7.4: Intermediate states of an hysteresis loop using periodic boundary conditions along the y-axis of the sample. The boundary effects of Figure 7.3 are not present but the coercive field of the sample is larger than that of the non-periodic model.

the electrostatic potential in the absence of magnetic field. In this equation the current density **J** is a function of the magnetisation distribution **M**, with the latter being computed using a standard micromagnetic calculation (that is without the effect of the electric field). As explained later on, this approach is justified by the negligible effect of the current on the magnetisation distribution, and for each value of the external magnetic field the AMR values computed solving the Poisson equation are derived assuming a constant magnetisation distribution. The generalised Poisson equation is derived by combining the equation for the conservation of charge

$$\frac{\partial \rho}{\partial t} + \nabla \cdot \mathbf{J} = 0 \tag{7.3}$$

with Ohm's law

$$\mathbf{J} = \sigma \mathbf{E}. \tag{7.4}$$

In these equations $\rho$ is the electric charge, **J** the current density and **E** the electric field. In the electrostatic case Eq. (7.3) reduces to

$$\nabla \cdot \mathbf{J} = 0 \tag{7.5}$$

and combining Eq.(7.5) and (7.4) with the definition of the electric field $\mathbf{E} = -\nabla\Phi$ we obtain

$$\nabla \cdot \mathbf{J} = \nabla \cdot (\sigma \mathbf{E}) = -\nabla \cdot (\sigma \nabla \Phi) = 0. \tag{7.6}$$

Calling $\hat{\mathbf{n}}$ the unit vector normal to the surface, the solution of this equation is completely defined once we fix the value of the potential at the top and bottom edges of the system

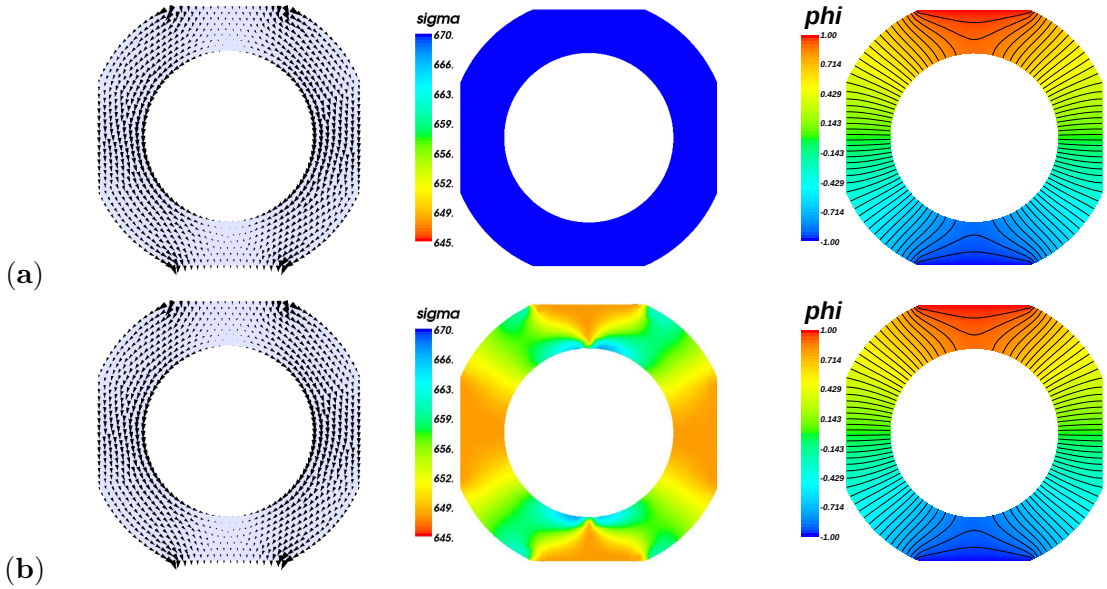


Figure 7.5: Distributions of current density (left), conductivity (centre) and potential (right) for the central ring with: (a) a uniform distribution; (b) when the iteration over Eq.(7.8) and (7.6) reaches self-consistency.

and impose the condition on the boundaries of the system

$$\hat{\mathbf{n}} \cdot \mathbf{J} = 0 \tag{7.7}$$

such that the current must not leave the sample outside the contact regions. From Eq. (7.2) the conductivity $\sigma$ can expressed as

$$\sigma(\theta) = \frac{1}{\rho(\theta)} = \frac{1}{\rho_0 \left(1 + \alpha \cdot \cos^2 \theta\right)} = \frac{\sigma_0}{1 + \alpha \cdot \cos^2 \theta} \tag{7.8}$$

and is therefore a function of $\mathbf{J}$ via the angle $\theta$ between $\mathbf{J}$ and the magnetisation $\mathbf{M}$. From Eq. (7.4) we also know that $\mathbf{J}$ is a function of $\sigma$, so that the distribution of $\Phi$, $\sigma$ and $\mathbf{J}$ can be found only solving Eq. (7.8) and (7.6) iteratively over all the array until self-consistency is reached for both the current and the conductivity distributions. In the computation of the current density $\mathbf{J}$ the Lorentz force is not considered because the applied field is in the plane of the film and any out-of-plane component of the current does not affect its in-plane direction.

Although the magnetisation $\mathbf{M}$ enters in the expression of $\mathbf{J}$ via the angle $\theta$ in the expression of the conductivity $\sigma$, the micromagnetic and electromagnetic modellings of our sample can be treated independently. This is because of the very low current density

(of the order of $10^3$ A/cm$^2$) considered in our analysis: experimentally a current starts to affect the magnetisation, via a spin-torque effect, when the density is above $10^8$ A/cm$^2$, that is 5 orders of magnitude larger than the values used in these simulations; hence in our model the equilibrium magnetisation can be considered independent of the applied electric field $V$ for each value of the external magnetic field, and the only interaction between current and magnetisation occurs through the conductivity redistribution.

An example of the conductivity redistribution using typical parameters of permalloy is shown in Figure 7.5(a) and (b). The magnetisation is assumed to have the equilibrium configuration for an applied field of 1000 mT along the negative direction of the y-axis, and the figures show the distribution of the $\mathbf{J}$, $\sigma$ and $\Phi$ fields on the central ring in the array of Figure 7.2(b). Starting from an initial configuration with a uniform conductivity distribution, shown in Figure 7.5(a), after some iterations (typically less than 10) the system reaches a self-consistent equilibrium where the conductivity has inhomogeneous values over the ring: Figure 7.5(b) shows that the conductivity is lowest where the magnetisation and the current are parallel, and increases with the misalignment between the two fields, with the maximum reached where they are orthogonal; the related fields $\mathbf{J}$ and $\Phi$, associated to the conductivity distribution by Eq. (7.6), are modified accordingly.

With the information about the current distribution, the total current $I$ flowing in the sample for a given voltage $V$ is computed integrating the current density over the contacts surface. The macroscopic resistance of the sample is then given by $R = V/I$ and we compute the AMR ratio $r_{\mathrm{AMR}}$ for each value of the applied field $H$ on the hysteresis curve as

$$r_{\mathrm{AMR}} = \frac{R(H)}{R(H=0)} - 1 \tag{7.9}$$

## 7.5 Hysteresis curve and AMR ratio

In the OOMMF simulation the hysteresis loop of the sample has been obtained varying the applied field from -1 T to 1 T in steps of 2 mT. For each applied field the values of the equilibrium magnetisation are interpolated over a two dimensional unstructured mesh; the mesh, shown in Figure 7.2(b), is then used in Nmag as the domain for the solution of Eq. (7.8) and (7.6) to (iteratively) compute the equilibrium angle $\theta$ between $\mathbf{M}$ and $\mathbf{J}$. The lack of any major constraint in the electromagnetic model and the smooth variation of the current distribution over the mesh allows to relax the constraints on the maximum edge length typical of micromagnetic simulations: to speed-up the simulation time we then used a mesh with an average rod length of 30 nm.

Using a $\rho_0 = 15$ $\mu\Omega$/cm [94] and $\alpha = 3.5\%$ [95] in Eq. (7.2), for each field step the

$r_{\mathrm{AMR}}$ is computed according to Eq. (7.9), and the comparison between the results obtained experimentally and numerically are shown in Figure 7.6(a)-(c).

The qualitative agreement between the measured and numerical AMR curves depends on the model used for the simulations. Using periodic boundary conditions the switching point is 41 mT compared to 23 mT using the non-periodic model. Moreover, the AMR ratio right before the switching point is comparable to that at large applied fields in the periodic model, but has a noticeable difference in the non-periodic model. Comparing Figure 7.6(a) and (c), we can see that the numerical model without periodic boundary conditions shows a better qualitative agreement with the experimental results, even if the quantitative agreement is rather poor. A possible explanation for the discrepancy can be found comparing Figure 7.6(b) and (c): the choice of boundary conditions has a strong effect on the behaviour of our modelled array and, although we restrict the analysis to the central ring, surface effects may still play a relevant role on the magnetisation distribution.

The comparison between the experimental AMR ratio, in the range $(-1.5 \times 10^{-3}, 0.5 \times 10^{-3})$, and those computed numerically, in the range $(-7.2 \times 10^{-3}, 0.4 \times 10^{-3})$ shows that the main quantitative difference between these cases is for large applied fields. A possible explanation is the presence of further anisotropic effects in the experimental sample, triggered by large applied fields, which are not considered in the numerical model.

As the best qualitative agreement with the experimental data is shown by the model without periodic boundary conditions, we use this model to understand the origin of the AMR curve in Figure 7.6(a). To this aim the magnetisation and current distribution for the points I, II and III in Figure 7.6(c) are analysed in detail.

Figure 7.7 shows the magnetisation and current density distributions (left) and the associated conductivity (right) for the central ring of the array at the points I, II and III. In the figures the current density is represented by white arrows of variable length, the magnetisation by black arrows of constant length, and the conductivity distribution is shown using bubbles with radius proportional to the local value of $\sigma$.

At point I the applied field is –1000 mT. With this field the magnetisation at equilibrium is nearly aligned with the negative y-axis over all the ring while the current, bound to follow the shape of the sample, takes the shortest path between the upper and lower interfaces, thus showing a larger value at the inner boundary of the ring as well as in the lateral regions of the upper and lower connections.

In the middle sections of a ring, *i.e.* East (E) and West (W) from the centre (see Figure 7.7-II (b)), the current density is nearly parallel to the magnetisation and from Eq. (7.8) the associated conductivity reaches a minimum. Moving towards the diagonal sections the conductivity increases. In these sections the magnetisation is still pointing in the negative y-direction but the current density, subject to the condition (7.5) at the

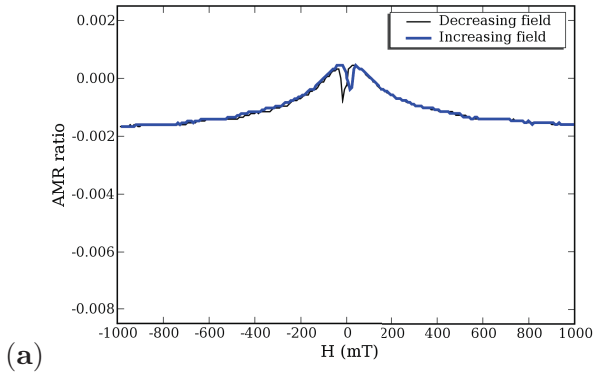


(a)

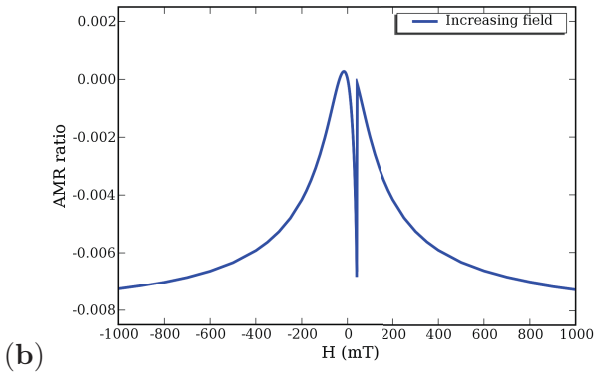


(b)

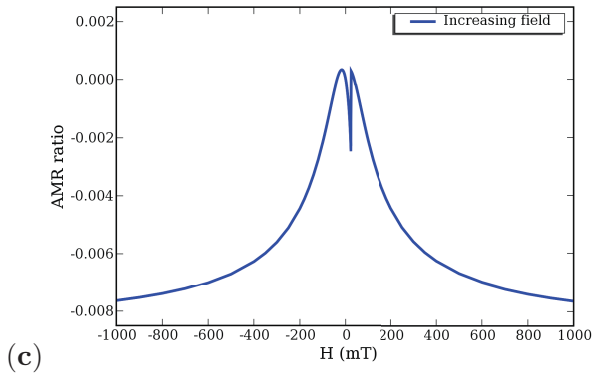


(c)

Figure 7.6: (a) AMR ratio obtained experimentally; (b) AMR ratio obtained numerically using periodic boundary conditions; (c) AMR ratio obtained numerically without periodic boundary conditions. The marked points I, II and III in (c) are discussed in detail and shown in Figure 7.7. Note that the experimental AMR data in (b) contains both branches (for increasing and decreasing applied magnetic field) whereas the simulated data (c) contains only AMR values for increasing field.

interfaces, rotates of an angle $\theta \simeq 45^\circ$ about the magnetisation direction.

Reducing the applied field the variation of the magnetisation in the lateral parts of the ring is negligible; an important modification does however occur in the diagonal sections, where the magnetisation aligns with the shape of the ring to reduce the demagnetising energy.

In this process the current density does not show a big variation from the case in I (a), thus the angle between the magnetisation and current density remains small in the lateral sections and decreases in the diagonal sections of the ring. The net result is a gradual reduction of the overall conductivity of the ring, reflected in an increasing resistivity when we go from point I to point II in Figure 7.6(a).

At point II, correspondent to an applied field of –18 mT, Figure 7.7-II (a) shows that **J** and **M** are nearly parallel over all the ring; the conductivity reaches its minimum virtually everywhere (II (b)), with an average value of $\sigma = 650$ S/m where the case of perfect alignment would give $\sigma = 1/\rho_0(1+\alpha) = 644$ S/m.

With a further increase of the applied field the angle between the magnetisation and the current density increases again in the diagonal parts of the ring. At point III the applied field is positive (22 mT) but the relatively small magnitude (below the coercive field $H_c = 23$ mT) is not sufficient to switch the magnetisation, whose average direction remains along the negative y-axis, though the y-component in the diagonal parts of the ring is smaller than that at point II. The larger angle between current density (which has not significantly changed from point I, to II to III) and magnetisation is reflected in the conductivity distribution (III(b)) in these areas, which presents an increased value if compared to II(b).

As the conductivity decreases going from point I to point II and increases again going to point III, the resistivity has its maximum at point II. This point is therefore associated to a peak in Figure 7.6(a), and analogous arguments hold for the curve above the coercive field, with the only difference being the magnetisation on the ring pointing in the positive y-direction.

## 7.6 Uniform current model

The model we used to compute the equilibrium configuration of the magnetisation is now compared with the so called uniform current model [96, 97]. In this model the conductivity of the system is computed assuming the current density to be uniform and pointing in the negative y-direction everywhere. The distribution of the AMR ratio for this case is represented by the green curve in Figure 7.8, while the blue one is the same curve of Figure 7.6 obtained with the original AMR model.

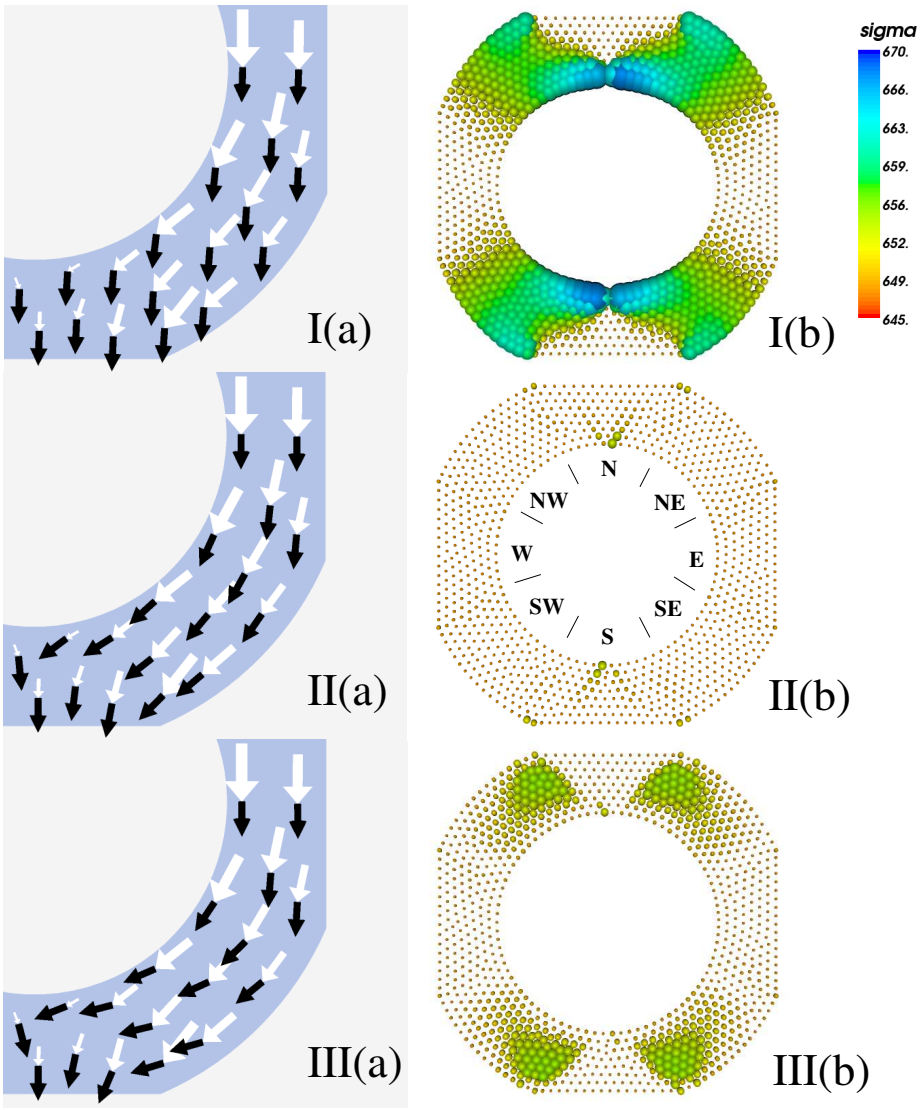


Figure 7.7: (a) Magnetisation and current density evolution in a section of the ring (with the full picture obtainable by symmetry considerations) and (b) corresponding conductivity distributions for the cases marked in Figure 7.6(a). The magnetisation **M** is represented by the black arrows, the current density **J** by the white ones. The conductivity distribution is shown using bubbles with radius proportional to the local conductivity value $\sigma$. The colour scale, expressed in S/m, is the same for all plots.

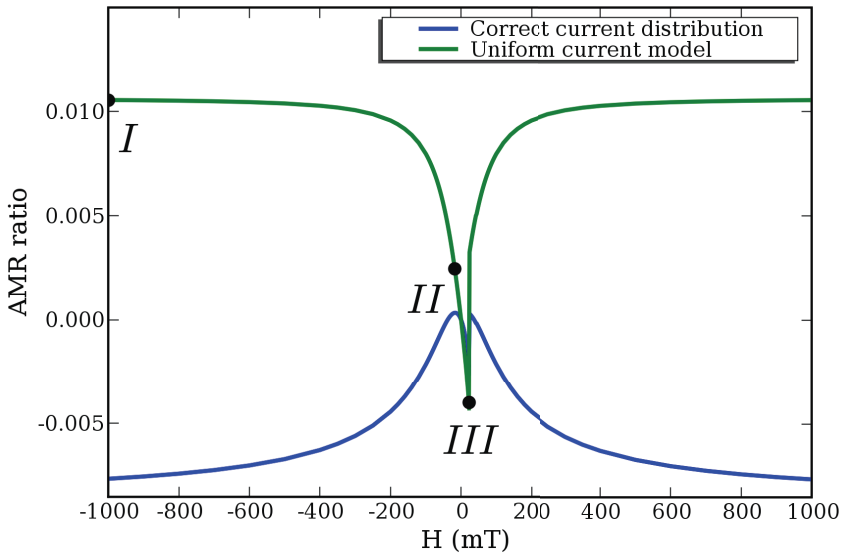


Figure 7.8: Comparison between AMR ratios computed with correct and uniform current models. The small positive value of the AMR at very large fields is due to the misalignment between the direction of the applied field (88° from the x-axis on the x-y plane) and the direction of the uniform current (along the y-axis on the x-y plane).

The magnetisation, current and conductivity distribution for the points I, II and III are shown in detail in Figure 7.9. Comparing Figure 7.7 and 7.9, the differences between the two models are present for all the points considered. The main difference is evidently present in the diagonal parts of the ring, where the misalignment between magnetisation and current density is a function of the applied field.

These results show that the conductivity in the uniform current model is significantly overestimated for the points II and III, while it is underestimated for point I. Moreover, from Figure 7.8 the value of the resistance at point I in the uniform current model shows a variation of the wrong sign with respect to the value at zero applied field when compared to the variation obtained experimentally.

From a quantitative point of view, the values found at point I and II cannot be obtained by any value of the applied field in the original model, while the AMR ratio computed with the uniform current model at point III gives a value $r_{\mathrm{AMR}} \approx -4 \cdot 10^{-3}$. Based on the data shown in Figure 7.6(c), this corresponds to an applied field of $\approx \pm 200$ mT in the original model whereas the actual applied field was 22 mT.

Recalling the experimental curve of $r_{\mathrm{AMR}}$ in Figure 7.6(a), these results indicate the limits of the uniform current model when performing an AMR analysis in confined geometries with rounded shape. On the other hand, the good agreement between the numerical

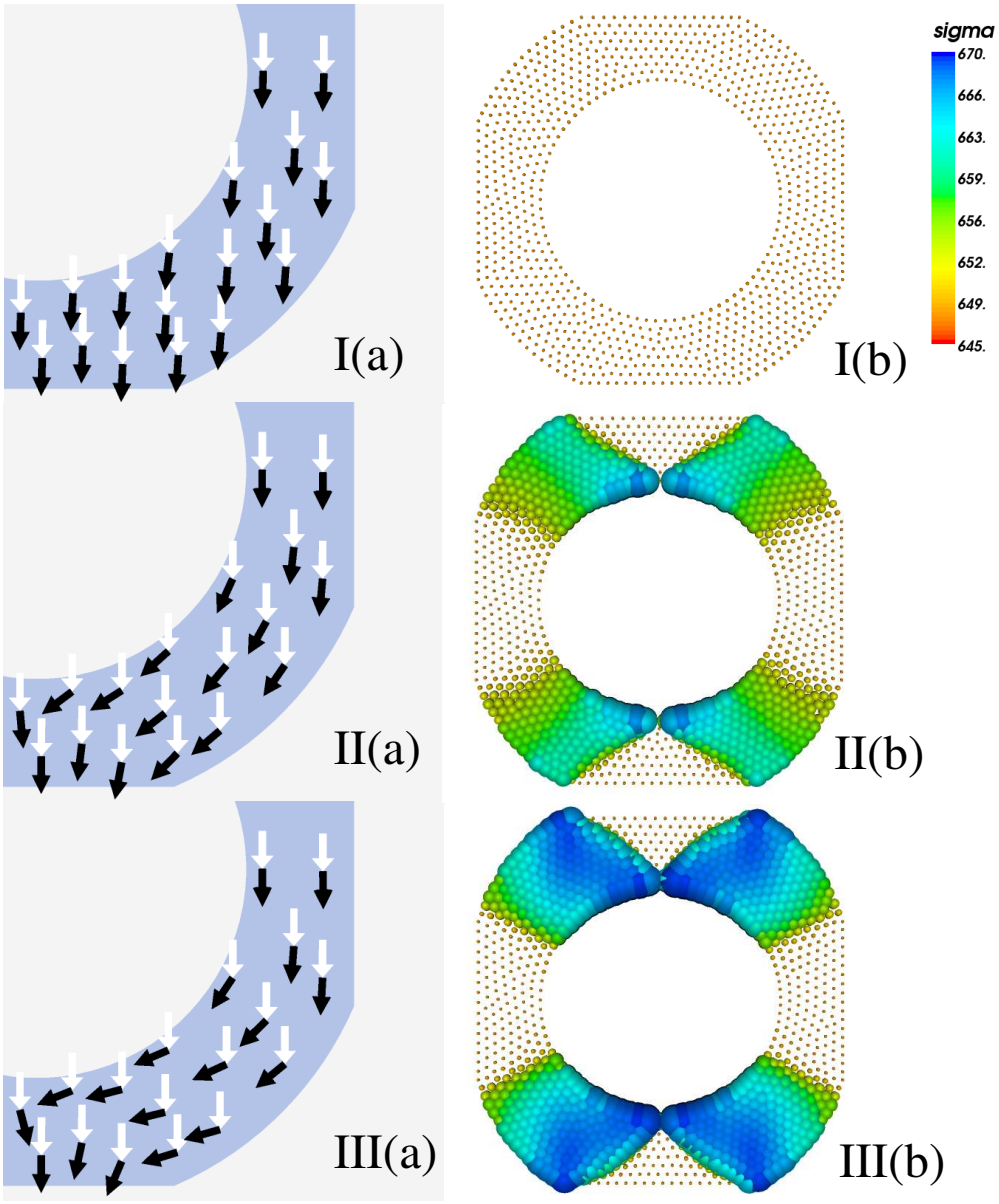


Figure 7.9: (a) The magnetisation and current density and (b) the conductivity distributions in the uniform current model for the cases marked in Figure 7.6(a). The arrows on the edge of the ring in (a) are intended for visualization purposes.

and experimental results of Figure 7.6(a) and (c), though showing a small quantitative difference probably due to the limited number of rings used in the model, show the importance to correctly compute the current distribution in these geometries.

## 7.7 Summary

In this chapter the magnetisation patterns and switching processes of the elements in a square array of connected rings have been studied by means of transport properties measurements.

The investigation is based on the Anisotropic Magneto-Resistance (AMR) effect, a property of ferromagnetic metals which consists in a variation of resistance in a ferromagnetic sample when placed in a magnetic field. The variation in resistance depends on the angle between the magnetisation and the direction of the electric current, and is usually expressed by the so called AMR ratio.

The aim of the analysis is to explain the experimental graph of this ratio during an hysteresis loop of the sample when the external field is applied nearly along one of the principal axis of the structure.

The computational model is obtained combining the micromagnetic model simulated with OOMMF and the electromagnetic model simulated with Nmag.

The magnetisation distribution obtained from OOMMF is interpolated on the unstructured mesh used for the Nmag model; the final model is then obtained coupling the magnetisation and electric fields according to the equations describing the AMR effect. The relation between the magnetisation and the current distribution is non-linear in the local angle between them and we have used a self-consistent approach to determine the AMR values numerically.

These values refer to a mesh made of 9 rings instead of the roughly $10^6$ in the experimental sample, and despite focusing the analysis on the properties of the central one, the relevance of surface effects is clear comparing the original model (without periodic boundary conditions) with one using periodic boundary conditions.

Nevertheless the agreement between the experimental and simulated results is qualitatively very good, and the analysis of the simulations allows to have a clear interpretation of the experimental data despite the poor quantitative agreement.

Finally, to test how the difference in current distribution affects the computation of the AMR ratio we have studied the same system using the uniform current model. In this model the current is assumed to have constant direction and be independent of the magnetisation distribution, an assumption which gives a very bad approximation of the real physics of the system.

We can therefore conclude that a correct computation of the current density is critical for a correct calculation of numerical AMR values, and our self-consistent approach has proved to be very effective in reproducing the equilibrium states of the magneto-electric coupled system.

# Chapter 8

# Summary and outlook

This thesis describes the development of computer simulation methodology, and the application of this methodology to study ferromagnetic structures at the nanoscale.

In Chapters 1 to 4, we have introduced the area of magnetism, the micromagnetic regime, the computational methods used to solve the equations, and described mesh generation techniques used for parts of this work.

In Chapter 5 we have introduced a novel approach to treat very large pseudo-periodic magnetic systems. This approach, called macro geometry, is used to overcome the limitations of Periodic Boundary Conditions (PBC) in situations where the overall shape of the sample has a relevant effect on the magnetisation distribution.

Using PBC, the surface of the system is pushed infinitely far away along the periodic axes. However, in micromagnetics one loses the information about the demagnetisation field of the system due to the disappearing surface charges. This can significantly affect its magnetic behaviour.

With the macro geometry approach the number and position of the quasi-periodic copies are explicitly defined, and the demagnetising field can be computed more accurately than using PBC.

This method has been applied to 1D and 2D arrays of three-dimensional magnetic objects. In a 1D system we computed the demagnetising field of a prism as a function of its length. With the magnetisation parallel or orthogonal to the longest edge, the values of the demagnetising field have a direct relation with the demagnetising factors of the geometry. These values can therefore be compared to the analytical expression of the demagnetising factors available for prisms, and we obtained an excellent agreement between the two sets of data.

Concerning 2D systems, we studied the magnetisation relaxation in an array of spheres arranged on a hexagonal lattice and confined along one dimension. The macro geometry approach was initially tested on a sub-system of 8 spheres where we considered the mag-

netisation evolution in a central element of the array. The behaviour obtained using a primary cell of two spheres and the macro geometry approach to mimic the presence of the other 6 showed a better approximation of the real system than using the same primary cell and PBC. The second test used the previous system of 8 spheres and PBC to approximate the original 2D array. The comparison between the magnetisation evolution in a central sphere of this system and the evolution in the corresponding macro geometry model using a primary cell of two spheres showed how this method can reproduce the effect of large but finite arrays using a minimal set of elements.

In Chapter 6, we have used the macro geometry approach to study to study demagnetising effects between the elements of triangular ring arrays. These elements are particularly suitable for MRAM applications because of the limited number of stable magnetic states, the simple and uniform switching between such states and the weak magnetostatic interaction between neighbour elements.

Using 50-nm size triangular elements, we found that if the spacing between the elements is larger than 30 nm the magnetostatic interactions can be considered negligible.

The results are obtained assuming that the external field is applied to one element of the array, and assuming that all the other rings have the same static magnetisation configuration. Even if this assumption overestimates the demagnetising field (because the rings do not have the freedom to react individually), we shown that the fixed magnetisation in the outer rings is a good approximation of the real behaviour of the array. Moreover, comparing the effect from arrays of different sizes we found that first and second nearest neighbours are the main source of magnetostatic interactions.

If a binary bit of information is stored in each of the rings, these results can be used to estimate the maximum areal density achievable with triangular ring elements, and further simulations are planned using different geometries like square rings, crosses and hollow cubes.

In Chapter 7, we report on studies of transport properties of connected rings arrays. This exploits the multi-physics features of Nmag which allow to extend the micromagnetic model with further equations to compute the electrostatic potential, the current density distribution and its interaction with the magnetisation. The elements were circular rings with internal and external diameters of 650 nm and 1100 nm, respectively, and the distance between their centres was 1000 nm.

The study of transport properties in arrays of connected elements is used to reveal details of the magnetisation patterns which might be hidden when the analysis is limited to the hysteresis loop of the sample. In the case of connected rings arrays, we based our analysis on the Anisotropic Magneto Resistance (AMR) signal.

The variation of the signal is related to the local angle between magnetisation and

electric current and its analysis requires the coupling of the two quantities in the micromagnetic model. Because of the non-linear dependence of the local resistivity on the angle between the magnetisation and the current distribution, in the simulations we used a self-consistent approach to determine the AMR values.

With this technique we obtained good qualitative agreeement with experimental AMR measurements and we shown how the magnetisation in the diagonal sections of the rings was the main cause of the variation of the AMR signal.

More generally, we found the effect of magnetisation on the conductivity of the sample to be a key point when computing the AMR values. We have shown how the uniform current model, where the current is assumed to have constant direction and magnitude and which is sometimes used in the literature to study AMR effects, can lead to qualitatively wrong results.

The study of AMR effects requires low current densities and in our simulations we used values sufficiently small to have a negligible effect of the current on the magnetisation, thus assuming no spin-torque effect and no interaction of the current's Oersted field with the magnetisation.

Looking ahead, further simulations are planned to study spin-torque effects in these systems. Thermal effects coming with larger current densities require the addition of a thermal field in the simulations. The effect of the temperature can be significant also in triangular rings arrays, and simulations of thermally assisted writing processes are the next step in the study of these systems.

Moreover, we plan to use matrix compression techniques for the boundary element matrix, in order to use primary cells with a larger number of elements. The results will be compared to the ones presented in this thesis to evaluate the effect of their size on the magnetic behaviour of the macro geometry model.

# Appendix A

# DistMesh algorithm

This is the DistMesh algorithm (reproduced from [50]) developed by P.-O. Persson and G. Strang which has been used as a reference for the Nmesh algorithm.

```
function [p,t]=distmesh2d(fd,fh,h0,bbox,pfix,varargin)

dptol=.001; ttol=.1; Fscale=1.2; deltat=.2; geps=.001*h0; deps=sqrt(eps)*h0;

% 1. Create initial distribution in bounding box (equilateral triangles)
[x,y]=meshgrid(bbox(1,1):h0:bbox(2,1),bbox(1,2):h0*sqrt(3)/2:bbox(2,2));
x(2:2:end,:)=x(2:2:end,:)+h0/2;                              % Shift even rows
p=[x(:),y(:)];                                               % List of node coordinates

% 2. Remove points outside the region, apply the rejection method
p=p(feval(fd,p,varargin{:})<geps,:);                         % Keep only d<0 points
r0=1./feval(fh,p,varargin{:}).^2;                            % Probability to keep point
p=[pfix; p(rand(size(p,1),1)<r0./max(r0),:)];                % Rejection method
N=size(p,1);                                                 % Number of points N

pold=inf;                                                    % For first iteration
while 1

  % 3. Retriangulation by the Delaunay algorithm
  if max(sqrt(sum((p-pold).^2,2))/h0)>ttol                   %  Any large movement?
    pold=p;                                                  %  Save current positions
    t=delaunayn(p);                                          %  List of triangles
    pmid=(p(t(:,1),:)+p(t(:,2),:)+p(t(:,3),:))/3;            %  Compute centroids
    t=t(feval(fd,pmid,varargin{:})<-geps,:);                 %  Keep interior triangles

    % 4. Describe each bar by a unique pair of nodes
    bars=[t(:,[1,2]);t(:,[1,3]);t(:,[2,3])];                 % Interior bars duplicated
```

```
    bars=unique(sort(bars,2),'rows');                          % Bars as node pairs

    % 5. Graphical output of the current mesh
    trimesh(t,p(:,1),p(:,2),zeros(N,1))
    view(2),axis equal,axis off,drawnow
  end

  % 6. Move mesh points based on bar lengths L and forces F
  barvec=p(bars(:,1),:)-p(bars(:,2),:);                        % List of bar vectors
  L=sqrt(sum(barvec.^2,2));                                    % L = Bar lengths
  hbars=feval(fh,(p(bars(:,1),:)+p(bars(:,2),:))/2,varargin{:});
  L0=hbars*Fscale*sqrt(sum(L.^2)/sum(hbars.^2));               % L0 = Desired lengths
  F=max(L0-L,0);                                               % Bar forces (scalars)
  Fvec=F./L*[1,1].*barvec;                                     % Bar forces (x,y components)
  Ftot=full(sparse(bars(:,[1,1,2,2]),ones(size(F))*[1,2,1,2],[Fvec,-Fvec],N,2));
  Ftot(1:size(pfix,1),:)=0;                                    % Force = 0 at fixed points
  p=p+deltat*Ftot;                                             % Update node positions

  % 7. Bring outside points back to the boundary
  d=feval(fd,p,varargin{:}); ix=d>0;                           % Find points outside (d>0)
  dgradx=(feval(fd,[p(ix,1)+deps,p(ix,2)],varargin{:})-d(ix))/deps; % Numerical
  dgrady=(feval(fd,[p(ix,1),p(ix,2)+deps],varargin{:})-d(ix))/deps; % gradient
  p(ix,:)=p(ix,:)-[d(ix).*dgradx,d(ix).*dgrady];               % Project back to boundary

  % 8. Termination criterion: All interior nodes move less than dptol (scaled)
  if max(sqrt(sum(deltat*Ftot(d<-geps,:).^2,2))/h0)<dptol, break; end
end
```

# Appendix B

# Nmesh user manual

The following sections are extracted from the Nmesh user manual available in the Nmag micromagnetic package. Only the features discussed in Chapter 4 are included and for a complete description of the Nmag features please refer to [2].

## B.1 Meshing an object

To create a mesh, we need to write a Python script that contains the geometry information of the objects that are do to be meshed.

### B.1.1 Meshing an ellipsoid (`tutorial1.py`)

```
1 import nmesh
2
3 cigar = nmesh.ellipsoid( [4,2] )
4
5 bbox = [[-4,-2],[4,2]]
6
7 mesh = nmesh.mesh(objects=[cigar],bounding_box=bbox)
8
9 nmesh.visual.plot2d_ps( mesh, "tutorial1.ps")
```

Line 1 imports the `nmesh` module. All our meshing scripts have to start with this line.

Line 3 creates a first "object" that we would like to mesh. In this case it is an `ellipsoid`, and the ellipsoid is provided by the nmesh-packages (therefore we have to access it with `nmesh.ellipsoid`. We pass two parameters to the ellipsoid, and this are the semi-axes in x-, and y- direction for the ellipsoid.

Note that at this point we have decided to create a two-dimensional mesh. Had we created an ellipsoid object like this,

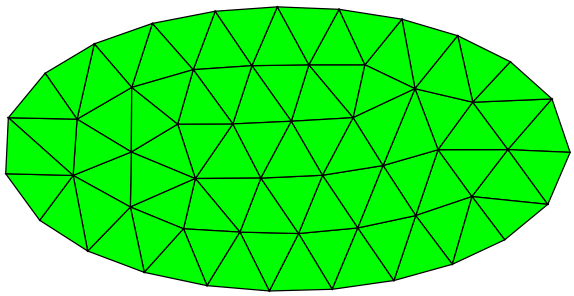

Figure B.1: The output of the `tutorial1.py` example.

```
cigar = nmesh.ellipsoid( [4,2,5] )
```

the we would have a *three-dimensional* object because we have specified the lengths of *three* semi-axes for the ellipsoid.

Line 5 defines a bounding box. The bounding box is a cuboid defined by providing the positions of opposite corners. It is always necessary to provide a bounding box that encloses all the objects to be meshed.

Line 7 carries out the actually meshing work. The arguments given to the function `nmesh.mesh()` are (in this simple case) a list of objects that we would like to mesh. Since we only want to mesh the `cigar`, we include only the cigar in this object list. The function returns a "mesh-object".

Line 9 creates a postscript file that visualises this mesh, and saves this postscript file to a file with name "`tutorial1.ps`".

If we run this script, it produces a mesh similar to the one shown in Figure B.1.

## B.2 The fundamental objects

### B.2.1 The ellipsoid

We have already seen an example for an ellipsoid in section B.1.1. As mentioned before, higher-dimensional ellipsoids are created by providing more lengths for the semi-axes (one for each dimension).

### B.2.2 The box

```
1 import nmesh
2
3 P1 = [0,0] #one corner of box
4 P2 = [5,10]#other corner
```

```
box = nmesh.box( P1,P2 )

bbox = [[0,0],[5,10]]

mesh = nmesh.mesh(bounding_box=bbox, objects=[box])

nmesh.visual.plot2d_ps( mesh, "box.ps")
```

A box is an n-dimensional cuboid and defined by providing the spatial coordinates of two opposite corners. In the example above, these corners are [0,0] and [5,10]. Note that each corner point must be provided as a python list, and both corners need to be provided within another list (as shown in `tutorial3.py` above). This script produces a mesh similar to the one shown in Figure B.2.

### B.2.3 The conical frustum

```
import nmesh

P2 = [0,4]  #center of 'circle' 2
R2 = 3      #radius of 'circle' 2
P1 = [0,0]  #center of 'circle' 1
R1 = 5      #radius of 'circle' 1


frustum = nmesh.conic( P1, R1, P2, R2 )

bbox = [[-5,0],[5,4]]

mesh = nmesh.mesh(objects=[frustum], bounding_box=bbox)

nmesh.visual.plot2d_ps( mesh, "frustum.ps")
```

The output of this script is shown in Figure B.3.

### B.2.4 The conical frustum in three dimensions

All of the objects listed here can be meshed in any (positive-integer) number of dimensions. We show only the frustum as 3d object to demonstrate this.

```
import nmesh
frustum = nmesh.conic([0.0,0.0,0.0],1.0,[2.0,0.0,0.0],2.0)
```

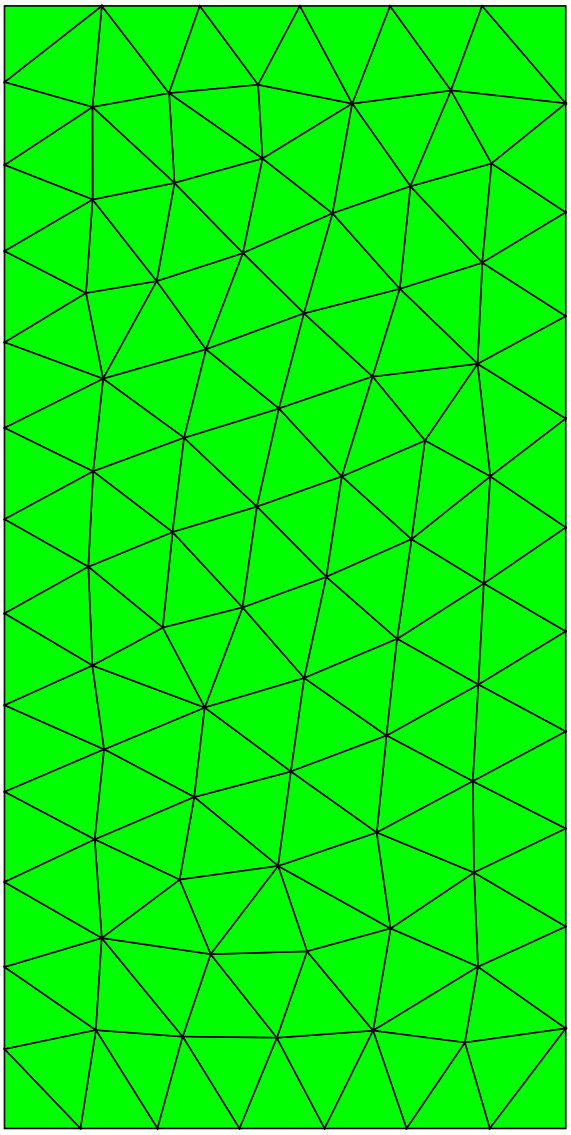

Figure B.2: The output of the `box.py` example.

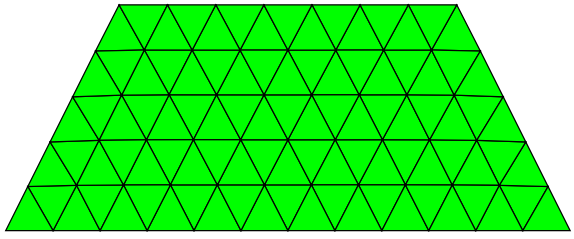

Figure B.3: The output of the `frustum.py` example. In two dimensions, the frustum appears as a trapezoid.

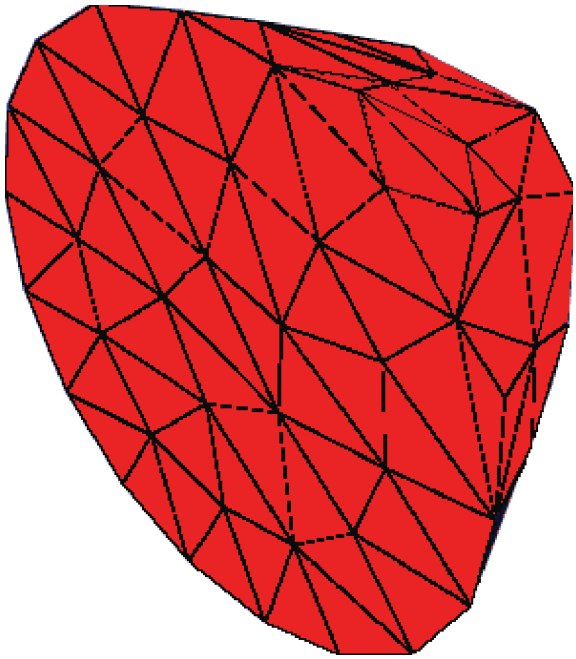

Figure B.4: The output of the `frustum3d.py` example.

```
bbox = [[-2.,-2.,-2.0],[2.,2.,2.]]

mesh = nmesh.mesh(objects = [frustum], bounding_box=bbox)

#create 3d-plot of surfaces
vis = nmesh.visual.show_bodies_mayavi(mesh)

import time
time.sleep(5)
#and save to eps file
nmesh.visual.export_visualisation(vis,"frustum3d.eps")
```

The output of this script is shown in Figure B.4.

## B.3 Translating, scaling and rotating objects

All mesh objects can be translated ("shift"), scaled and rotated. This section provides some examples.

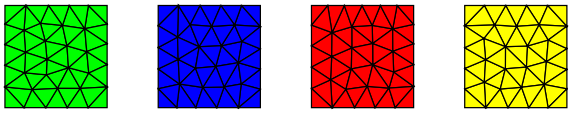

Figure B.5: The output of the `shift.py` example.

### B.3.1 Translation (`shift.py`)

The easiest transformation is to translate an object. This is done by adding an optional argument with name `transform` to the constructor of the object. For example, to shift a box with unit volume by 3 units in x and 4 units in y (in two dimensions), we could use this line:

```
box = nmesh.box( [0,0],[1,1], transform=[ ("shift",[3,4]) ] )
```

Note that actual shift transformation is just `("shift",[3,4])`. The first argument of the tuple specifies that we request a `shift`, the second argument is the translation vector.

Because many such transformations can be specified, these are accumulated in a list (that's where the square brackets come from).

Here is a complete example:

```
import nmesh

squares = []

for i in range(4):
    xshift = i*6
    yshift = 0
    squares.append( nmesh.box( [-2,-2],[2,2],
                               transform=[("shift",[xshift,yshift])]
                               )
                    )

bbox = [[-5,-5],[23,5]]
mesh = nmesh.mesh(objects=squares,bounding_box=bbox)

# plot mesh
nmesh.visual.plot2d_ps(mesh,"shift.ps")
```

and Figure B.5 shows the output.

### B.3.2 Scaling (`scale.py`)

The syntax for scaling is very similar to the syntax for shifting (B.3.1). Here is an example

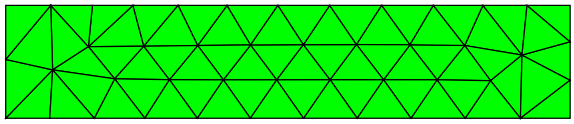

Figure B.6: The output of the `scale.py` example.

```
import nmesh

x = nmesh.box( [0,0],[1,1], transform=[("scale",[10,2])])

bbox = [[-2,-2],[12,4]]
mesh = nmesh.mesh(objects=[x],bounding_box=bbox)

nmesh.visual.plot2d_ps(mesh,"scale.ps")
```

and Figure B.6 shows the corresponding mesh.

### B.3.3 Rotation

**In 2 dimensions (`rotate2d.py`)** Rotation in two dimensions requires only one angle (in degree). The rotation is carried out in the mathematical sense (i.e. counter clock wise). Here is an example

```
import nmesh

x = nmesh.box( [0,0],[5,5], transform=[("rotate2d",30)])

bbox = [[-10,-10],[10,10]]
mesh = nmesh.mesh(objects=[x],bounding_box=bbox,mesh_bounding_box=True)

nmesh.visual.plot2d_ps(mesh,"rotate2d.ps")
```

and Figure B.7 shows the corresponding mesh.

**In 3 dimensions (`rotate3d.py`)** In three dimensions there is a transformation with name `rotate3d` which accepts an axis to rotate around and an angle (in degree) specifying how far to rotate around that axis.

The transformation to rotate around [0,0,1] for 45 degrees would thus read

```
("rotate3d",[0,0,1],45)
```

The complete example is

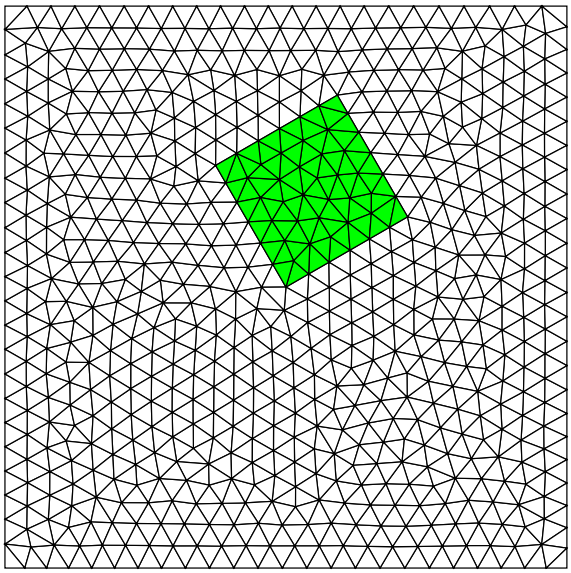

Figure B.7: The output of the `rotate2d.py` example.

```
import nmesh

box1 = nmesh.box( [-1,-1,2],[1,1,4], \
                  transform=[("rotate3d",[0,0,1],45)])

ground = nmesh.box( [-1,-1,-0.3],[1,1,1] )

bbox = [[-2,-2,-0.3],[2,2,4]]

mesh = nmesh.mesh(objects=[ground,box1],bounding_box=bbox,a0=0.5)

mesh.save("rotate3d.nmesh")

# visualise in MayaVi
vis =nmesh.visual.show_bodies_mayavi(mesh)

nmesh.visual.export_visualisation(vis,"rotate3d.eps")
```

and creates the mesh shown in Figure B.8.

**In $n$ dimensions (`rotate.py`)** In general, a rotation is carried out by specifying the indices of the dimensions around which no rotation takes place, and an angle. The syntax to rotate 45 degrees in the x-y plane would therefore be

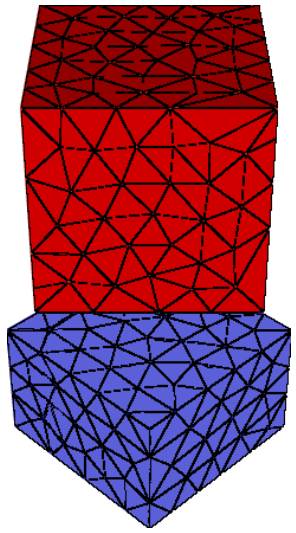

Figure B.8: The output of the `rotate3d.py` example.

```
("rotate",[0,1],45)
```

Here is the example of a rotation around the $z$-axis:

```
import nmesh

# rotation of the object is performed
# around the [0,0,1] axis (z-axis).
box = nmesh.box( [0,0,0],[2,1,1], transform=[("rotate",[0,1],0)])

bbox = [[-1,-1,-1],[3,3,3]]
mesh = nmesh.mesh(objects=[box],bounding_box=bbox, \
                  mesh_bounding_box=False,a0=0.5)

mesh.save('rotate.nmesh')

#create 3d-plot of surfaces and export eps
vis=nmesh.visual.show_bodies_mayavi(mesh)
nmesh.visual.export_visualisation(vis,"rotate.eps")
```

and Figure B.9 shows the corresponding mesh.

### B.3.4 Combining transformations (`transformations`)

Any number of transformations can be specified in a list, and are carried out in the order they are given in the list.

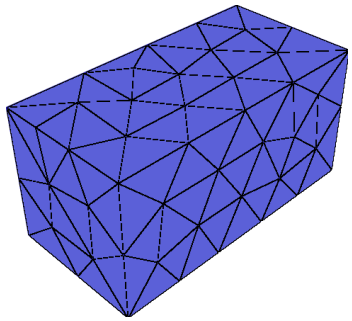

Figure B.9: The output of the `rotate.py` example.

Here is a more complex example

```
import nmesh

box = nmesh.box([0.0,0.0], [1.0,1.0],                    \
                transform=[("rotate2d",45),              \
                           ("shift",[-1.0,-2.0]),        \
                           ("scale",[1.5,1.5])])
# create ellipsoid
ell = nmesh.ellipsoid([1.0,2.0],                         \
                      transform=[("rotate2d",45),        \
                                 ("shift",[1.0,1.0]),])

rod= 0.5
bbox = [[-3.,-3.],[4.,4.]]

# create mesh
mesh = nmesh.mesh(objects = [box,ell], a0=rod, bounding_box=bbox)

# plot mesh
nmesh.visual.plot2d_ps(mesh,"transformations.ps")
```

and Figure B.10 shows the corresponding mesh.

## B.4 Combining objects

In most applications, we would like to mesh more complicated systems, consisting of more than one fundamental geometry type. We have a number of options how to combine these within `nmesh`.

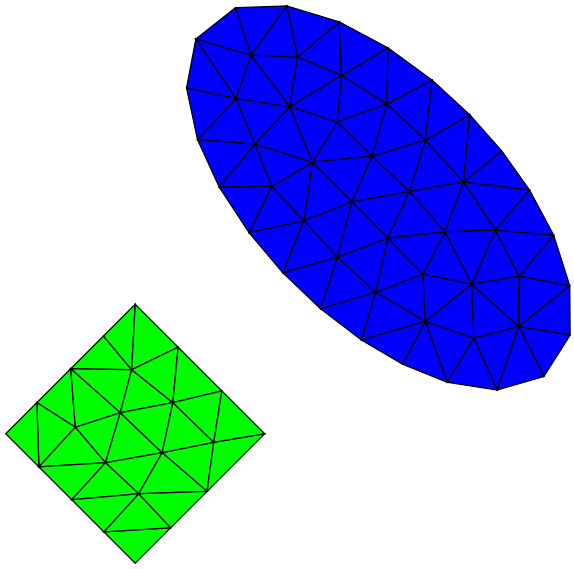

Figure B.10: The output of the `transformations.py` example.

### B.4.1 Plotting several objects (`multiobjects.py`)

We can simply create more objects and mesh these together by providing them in a list to `nmesh.mesh()`. Here is an example

```
import nmesh

# create a number of objects
one = nmesh.ellipsoid([3.0,3.0])
two = nmesh.ellipsoid([3.0,3.0],transform=[("shift",[7,0])])
three=nmesh.box( [-4.0,-6], [10,-4] )

bbox = [[-5.,-8.],[11.,5.]]

# create mesh of three objects and bounding box
mesh_ex = nmesh.mesh(objects = [one,two,three], bounding_box=bbox,
                     mesh_bounding_box=True, a0=0.7)

# plot mesh
nmesh.visual.plot2d_ps(mesh_ex,"multiobjects.ps")
```

and Figure B.6 shows the corresponding mesh.

### B.4.2 Union (`union.py`)

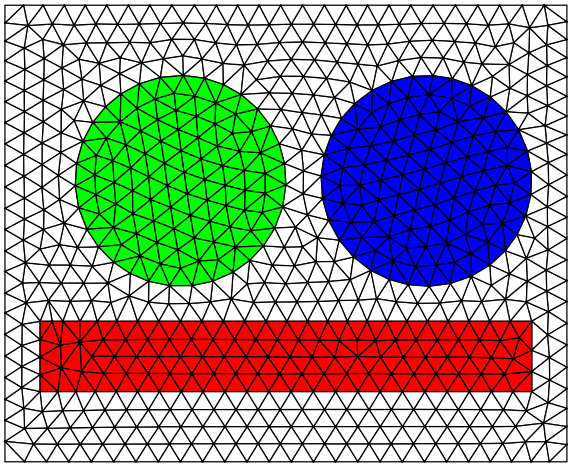

Figure B.11: The output of the `multiobjects.py` example.

```
union = nmesh.union([A,B,C,D])
```

The `nmesh.union()` function takes a list of objects (here A,B,C and D) and returns an object that is the union of the provided objects. The list of objects can be of any length.

This allows to "merge" several objects together. Here is an example:

```
import nmesh

box = nmesh.box( [-4,-2],[4,2] )
ellipsoid = nmesh.ellipsoid([3,3])

# create union
union = nmesh.union([box,ellipsoid])

bbox = [[-5,-4],[5,4]]
mesh = nmesh.mesh(objects = [union],bounding_box=bbox,a0=0.8)
mesh.save("union.nmesh")
nmesh.visual.plot2d_ps(mesh,"union.ps")
```

and Figure B.6 shows the corresponding mesh.

### B.4.3 Difference (`difference.py`)

To "subtract" one objects from another, one can use the `nmesh.difference()` function. Its syntax is:

```
diff = nmesh.difference(A,[B,C,D])
```

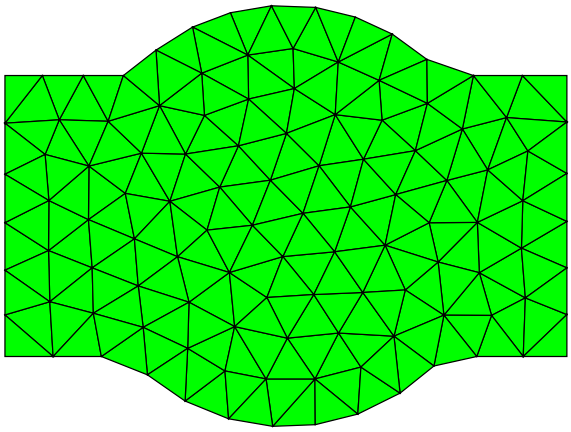

Figure B.12: The output of the `union.py` example. A circle and a rectangle are merged together.

This would subtract objects B,C and D from object A, and return the new difference object. Here is a complete example

```
import nmesh

big = nmesh.ellipsoid([4.0,3.0])     # create a big ellipsoid
small = nmesh.ellipsoid([3.0,2.0])   # small ellipsoid

diff = nmesh.difference(big,[small])# create difference of ellipsoids

bbox = [[-5.,-4.],[5.,4.]]
mesh_ex = nmesh.mesh(objects = [diff], a0=0.4, bounding_box=bbox)

# plot mesh
nmesh.visual.plot2d_ps(mesh_ex,"difference.ps")
```

and Figure B.6 shows the corresponding mesh.

### B.4.4 Intersection (`intersection.py`)

```
intersection = nmesh.intersection([A,B,C,D])
```

The `nmesh.intersection()` function takes a list of objects (here A,B,C and D) and returns an object that is the intersection of the provided objects. The list of objects can be of any length. Here is an example:

```
import nmesh
```

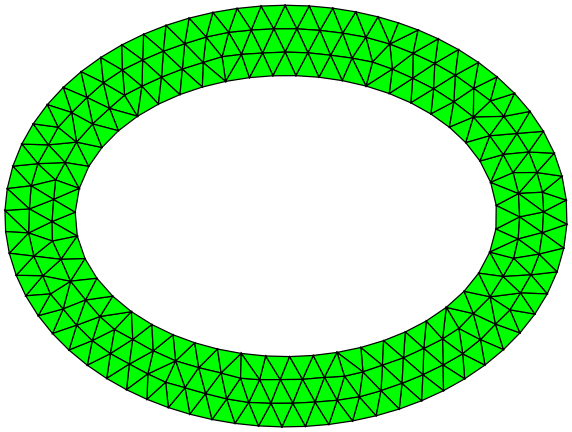

Figure B.13: The output of the `difference.py` example. A small ellipse is removed from a large ellipse, leaving an "elliptical ring".

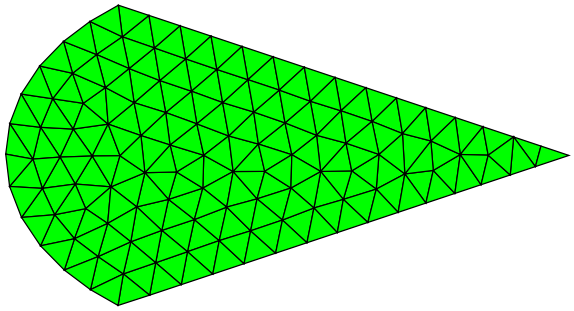

Figure B.14: The output of the `intersection.py` example showing the intersection of an ellipsoid and a cone.

```
ell = nmesh.ellipsoid([3,2])              # create ellipsoid
cone = nmesh.conic([-3,0],2,[3,0],0)      # create cone

inters = nmesh.intersect([ell, cone])     # create intersection of objects

bbox = [[-5.,-4.],[5.,4.]]
mesh_ex = nmesh.mesh(objects = [inters], a0=0.4, bounding_box=bbox)

nmesh.visual.plot2d_ps(mesh_ex,"intersection.ps")
```

and Figure B.14 shows the corresponding mesh.

## B.5 Providing a call back function (`callback.py`)

The mesher can be provided with a call back function that is called every $n$ iterations in the computation process of the mesh. This can be used to provide real time visualisation of the meshing process or to study for example the mesh quality is a function of iterations.

The basic idea is to call the mesher with a call back function `f` and a number $n$ in the following fashion:

```
mesh = nmesh.mesh(objects = [...] callback = (f,n))
```

Here is a complete example:

```
import nmesh

box1 = nmesh.box( [0.0,0.0],[3.0,3.0] )
box2 = nmesh.box( [-1.0,-1.0],[-3.0,-3.0] )
circle = nmesh.ellipsoid(length=[1.5,1.5],transform=[("shift",[-2.,2.])])

bbox = [[-4,-4],[4,4]]

#define call back function
def my_fun(piece_nr, iteration_nr, mesh_info):
    print "** In callback function: Piece %d, Step %d \n" % \
          (piece_nr, iteration_nr)

    print "Points = %d\nSimplices = %d\nSurface elements = %d\n" % \
          (len(mesh_info[0][2]),len(mesh_info[2][2]),len(mesh_info[4][2]))

#Call callback function every 5 iterations
mesh = nmesh.mesh(objects = [box1,box2,circle], bounding_box=bbox, \
                  a0=0.5, callback = (my_fun,5))

nmesh.visual.plot2d_ps(mesh,"callback.ps")
```

The call back function (`my_fun` in the above example) is given three arguments:

- The `piece_nr`. This is an integer labelling the different objects to be meshed. If the bounding box is meshed, it carries the piece number 0.
- The `iteration_nr`. This is the counter of the iterations within the mesher.
- The `mesh_info`. This is the same Python list given by the command `mesh.tolists()` in section B.6 for the mesh that is currently being computed.

## B.6 Access to the mesh from Python (`tolists.py`)

The data contained in a mesh object `mesh` can be extracted to a python list of lists with the command `mesh.tolists()` as shown in the following program

```
import nmesh

ellipsoid = nmesh.ellipsoid([0.75,1.25,1])

# create mesh
bbox = [[-0.75,-1.25,-1],[0.75,1.25,1]]

mesh = nmesh.mesh(objects = [ellipsoid], bounding_box=bbox,a0=0.5)

# extract the mesh data in a list of lists
mesh_info = mesh.tolists()
```

The resulting list contains these information:

- COORDS = Coordinates of points;
- LINKS = Connections within the mesh (pairs of point indices);
- SIMPLICES = Information on the simplices through points coordinates, circumcircle centre and radius, incircle centre and radius and region the simplices belong to;
- POINT-BODIES = Which bodies does the corresponding point belong to (body index list);
- SURFACES = Information on surface elements through points coordinates, circumcircle centre and radius, incircle centre and radius and region the elements belong to.

For more details refer to the complete Nmag manual.

# Bibliography


[1] M. Kläui et al. Vortex formation in narrow ferromagnetic rings. *J. Phys.: Condens. Matter*, 15:R985–R1023, 2003.

[2] Nmag - a micromagnetic simulation environment. `http://www.soton.ac.uk/~fangohr/nsim/nmag`.

[3] C. W. King. *The natural history, ancient and modern, of precious stones and gems, and of the precious metals*. London: Bell and Daldy, 1865.

[4] R. Elliott. The story of magnetism. *Physica A*, 384:44–52, 2007.

[5] M. McCaig. *Permanent magnets in theory and practice*. London: Pentech, 2nd edition, 1987.

[6] F. Bitter. Experiments on the nature of ferromagnetism. *Phys. Rev.*, 41:507–515, 1932.

[7] C. Kittel. *Introduction to solid state physics*. New York: Wiley, 1996.

[8] R. C. O'Handley. *Modern magnetic materials: principles and applications*. John Wiley and Sons, Inc., 1999.

[9] J. A. Livingstone. *Driving force: the natural magic of magnets*. Harvard University Press, 1997.

[10] C. Kittel. Physical theory of ferromagnetic domains. *Rev. Mod. Phys.*, 21(4):541–583, 2003.

[11] G. M. B. de Albuquerque. *Magnetisation precession in confined geometry: physical and numerical aspects*. PhD thesis, UFR Scientifique d'Orsay, Université Paris XI, 2002.

[12] A. Aharoni. *Introduction to the theory of ferromagnetism*. Oxford Science Publications, 2nd edition, 2000.

[13] W. F. Brown, Jr. *Micromagnetics*. Wiley Interscience, New York, 1963.

[14] C. L. Dennis et al. The defining length scales of mesomagnetism: a review. *J. Phys.: Condens. Matter*, 14(49):R1175–R1262, 2002.

[15] R. Schäfer A. Hubert. *Magnetic Domains: the analysis of magnetic microstructures*. Springer, 1998.

[16] R. Skomski. Topical review - nanomagnetics. *Journal of Physics: Condensed Matter*, 15:R841–R896, 2003.

[17] E. C. Stoner and E. P. Wohlfarth. A mechanism of magnetic hysteresis in heterogeneous alloys. *Philosophical Transactions of the Royal Society London*, A240:599–642, 1948.

[18] T. L. Gilbert. A Lagrangian formulation of gyromagnetic equation of the magnetization field. *Physical Review*, 100:1243, 1955.

[19] L. D. Landau and E. M. Lifshitz. On the theory of the dispersion of magnetic permeability in ferromagnetic bodies. *Physikalische Zeitschrift der Sowjetunion*, 8(2):153–169, 1935.

[20] D. H. Tarling. *Paleomagnetism: principles and applications in geology, geophysics and archaeology*. London: Chapman and Hall, 1983.

[21] B. Azzerboni et al., editor. *Magnetic nanostructures in modern technology*. NATO science for peace and security series. Springer, 2008.

[22] C. A. Ross et al. Patterned magnetic recording media. *Annu. Rev. Mater. Res.*, 31:203–235, 2001.

[23] A. Moser et al. Magnetic recording: advancing into the future. *J. Phys. D: App. Phys.*, 35:R157–R167, 2002.

[24] D. Weller and M. F. Doerner. Extremely high-density longitudinal magnetic recording media. *Annu. Rev. Mater. Sci.*, 30:611–644, 2000.

[25] B. Terris et al. Patterned media for future magnetic data storage. *Microsystem Technologies*, 13(2):189–196, 2007.

[26] MK3252GSX hard disk drive. Toshiba GST, 2007.

[27] C. Chappert et al. The emergence of spin electronics in data storage. *Nature Materials*, 6:813–823, 2007.

[28] J. S. Moodera et al. Large magnetoresistance at room temperature in ferromagnetic thin film tunnel junctions. *Phys. Rev. Lett.*, 74(16):3273–3276, 1995.

[29] Mram devices. Freescale, 2007.

[30] J. Slaughter. Mram technology: Status and future challenges. Cornell CNS Nanotechnology Symposium, 2004.

[31] K. Ju and O. C. Allegranza. Multi-bit cells design for toggle mram applications. *Magnetics Conference 2006. Intermag 2006. IEEE International*, page 399, 2006.

[32] M. A. B. W. Bolte et al. Simulation of micromagnetic phenomena. In *18th European Simulation Conference*, pages 407–412, 2004.

[33] D. J. Dunlop A. J. Newell, W. Williams. A generalization of the demagnetizing tensor for nonuniform magnetization. *J. Geophys. Res.*, 98(B6):9551–9555, 1993.

[34] William H. Press et al. *Numerical recipes: the art of scientific computing*. Cambridge University Press, Cambridge (UK) and New York, 2nd edition, 1992.

[35] M.J. Donahue and R.D. McMichael. Micromagnetics on curved geometries using rectangular cells: error correction and analysis. *IEEE Trans. Magn.*, 43:2878–2880, 2007.

[36] W. E C. J. García-Cervera, Z. Gimbutas. Accurate numerical methods for micromagnetics simulations with general geometries. *J. Comp. Phys.*, 184(1):37–52, 2003.

[37] J. Fidler and T. Schrefl. Micromagnetic modelling - the current state of the art. *J. Phys. D: App. Phys.*, 33:R135–R156, 2000.

[38] J. R. Shewchuk. What is a good linear element? Interpolation, conditioning, and quality measures. In *International Meshing Roundtable*, pages 115–126, 2002.

[39] P. L. DeVries. *A first course in Computational physics*. John Wiley & Sons Inc, New York, 1994.

[40] M.J. Fagan. *Finite element analysis - theory and practice*. Longmans, 1992.

[41] B. Yang and D. R. Fredkin. Dynamical micromagnetics by the finite element method. *IEEE Trans. Magn.*, 34:3842–3852, 1998.

[42] P. H. W. Ridley. *Finite element simulation of the micromagnetic behaviour of nanoelements*. PhD thesis, School of Informatics, University of Wales, Bangor, 2000.

[43] K. D. Mish et al. Finite element procedures in applied mechanics. U.C. Davis, Department of Civil and Environmental Engineering, 2000.

[44] J. D. Jackson. *Classical electrodynamics*. Wiley, 3 edition, 1999.

[45] D. R. Fredkin and T. R. Koehler. Hybrid method for computing demagnetizing fields. *IEEE Trans. Magn.*, 26:415–417, 1990.

[46] D. A. Lindholm. Three dimensional magnetostatic fields from point-matched integral equations with linearly varying scalar sources. *IEEE Trans. Magn.*, MAG-20:2025–2032, 1984.

[47] W. Hackbusch et al. Hlib package. `http://www.hlib.org/hlib.html`.

[48] G. M. B. de Albuquerque. *Scalable Parallel Micromagnetic Solvers for Magnetic Nanostructures*. PhD thesis, Vienna University of Technology, 2003.

[49] Netgen. `http://www.hpfem.jku.at/netgen/`.

[50] P.-O. Persson and G. Strang. A simple mesh generator in matlab. *SIAM Review*, 46(2):329–345, 2004.

[51] G. van Rossum. Python website, 2003. `http://www.python.org`.

[52] E. Chailloux et al. *Développement d'applications avec objective caml*. O'Reilly, 1st ed., 2000. On-line english version: `http://caml.inria.fr`.

[53] C. B. Barber et al. Qhull website, 2003. `http://www.qhull.org`.

[54] F. J. Bossen. Anisotropic mesh generation with particles. Technical Report CMU-CS-96-134, May 1996.

[55] D. A. Field. Qualitative measures for initial meshes. *Int. J. Numer. Meth. Engin.*, 47:887–906, 2000.

[56] Z. J. Cendes and D. N. Shenton. Adaptive mesh refinement in the finite element computation of magnetic fields. *IEEE Trans. Magn.*, 21(5):1811–1816, 1985.

[57] J.R. Shewchuk. Tetrahedral mesh generation by Delaunay refinement. In *Symposium on Computational Geometry*, pages 86–95, 1998.

[58] G. Strang and G. J. Fix. *An analysis of the finite element method*. Prentice-Hall: Englewood Cliffs, NJ, 1973.

[59] X. Li. *Sliver-free three dimensonal Delaunay mesh generation*. PhD thesis, University of Illinois at Urbana-Champaign, 2000.

[60] P. Krysl and M. Ortiz. Generation of tetrahedral finite element meshes: Variational Delaunay approach. In *International Meshing Roundtable*, pages 273–284, 1998.

[61] B. Joe. Construction of three-dimensional improved-quality triangulation using local transformations. *SIAM J. Sci. Comput.*, 16(6):1292–1307, 1995.

[62] L. A. Freitag and C. Ollivier-Gooch. Tetrahedral mesh improvement using swapping and smoothing. *International Journal for Numerical Methods in Engineering*, 40(21):3979–4002, 1998.

[63] S.-W. Cheng et al. Sliver exudation. *Journal of the ACM*, 47(5):883–904, 2000.

[64] G. Bordignon et al. A new approach to (quasi) periodic boundary conditions: the macro geometry. *J. Appl. Phys.*, submitted, 2008.

[65] A. Aharoni. Demagnetizing factors for rectangular ferromagnetic prisms. *J. Appl. Phys.*, 83(6):3432–3434, 1998.

[66] M. Donahue and D. Porter. Object Oriented Micro-Magnetic Framework (OOMMF). `http://math.nist.gov/oommf/`.

[67] M. E. Kiziroglou et al. Orientation and symmetry control of inverse sphere magnetic nanoarrays by guided self-assembly. *J. Appl. Phys.*, 100:113720.1–5, 2006.

[68] M. A. Ghanem et al. A double templated electrodeposition method for the fabrication of arrays of metal nanodots. *Electrochem. Commun.*, 6(5):447–453, 2004.

[69] Sundials: Suite of nonlinear and differential/algebraic equation solvers. `http://sundials.wikidot.com/start`.

[70] G. Bordignon et al. Numerical studies of demagnetizing effects in triangular ring arrays. *J. Appl. Phys.*, 103:07D932.1–3, 2008.

[71] S. Y. Chou. Patterned magnetic nanostructures and quantized magnetic disks. In *Proceedings of the IEEE*, pages 652–671, 1997.

[72] T. A. Savas et al. Properties of large-area nanomagnet arrays with 100 nm period made by interferometric lithography. *J. Appl. Phys.*, 85(8):6160–6162, 1999.

[73] C. A. F. Vaz et al. Mesoscopic fcc co ring magnets. *J. Magn. Magn. Mat.*, 249:208–213, 2002.

[74] P. Vavassori et al. Magnetization switching in permalloy square ring magnets. *J. Appl. Phys*, 93(10):7900–7902, 2003.

[75] M. Kläui et al. Multistep switching phase diagram of ferromagnetic ring structures. *J. Appl. Phys.*, 95(11):6639–6641, 2004.

[76] M. H. Park et. al. Vortex head-to-head domain walls and their formation in onion-state ring elements. *Phys. Rev. B*, 73:094424.1–5, 2006.

[77] M. Kläui et al. Domain wall pinning and controlled magnetic switching in narrow ferromagnetic ring structures with notches. *J. Appl. Phys.*, 93(10):7885–7890, 2003.

[78] A. S. Mani et al. Magnetic random access memory design using rings with controlled asymmetry. *Nanotechnology*, 15:S645–S648, 2004.

[79] A. Imre et al. Flux-closure magnetic states in triangular cobalt ring elements. *IEEE Trans. Magn.*, 11:3641–3644, 2006.

[80] F. J. Casta no et al. Magnetic configurations in 160-520-nm-diameter ferromagnetic rings. *Phys. Rev. B*, 69:144421.1–7, 2004.

[81] P. Vavassori et al. Chirality and stability of vortex state in permalloy triangular ring micromagnets. *J. Appl. Phys*, 101:023902.1–10, 2007.

[82] A. Westphalen et al. Magnetization reversal of thin fe triangular rings. *Superlatt. Microstruct.*, 41:98–103, 2007.

[83] J.J. Torres-Heredia et al. Micromagnetic simulations of 200-nm-diameter cobalt nanorings using a reuleaux triangular geometry. *J. Magn. Magn. Mat.*, 305(1):133–140, 2006.

[84] J. Wang et al. Magnetostatic interactions in mesoscopic $ni_{80}fe_{20}$ ring arrays. *Appl. Phys. Lett.*, 87:262508.1–3, 2005.

[85] M. Kläui et al. Domain wall coupling and collective switching in interacting mesoscopic ring magnet arrays. *Appl. Phys. Lett.*, 86:032504.1–3.

[86] R. Hertel et al. Micromagnetic simulations of magnetostatically coupled nickel nanowires. *J. Appl. Phys.*, 90(11):5752–5758, 2001.

[87] J. Jorzick et al. Magneto-dipole coupling in arrays of micron-size rectangular magnetic elements. *J. Magn. Magn. Mat.*, 226(2):1835–1837, 2001.

[88] G. Bordignon et al. Analysis of magnetoresistance in arrays of connected nano-rings. *IEEE Trans. Magn.*, 43(6):2881–2883, 2007.

[89] V. Metlushko et al. Arrays of nano-rings for magnetic storage applications. *Proc. 2nd IEEE Conf. Nanotech.*, Aug. 26-28:63–66, 2002.

[90] A. V. Goncharov et al. Anisotropy of magnetization reversal and magnetoresistance in square arrays of permalloy nano-rings. *IEEE Trans. Magn.*, 42(10):2948–2950, 2006.

[91] W. Thomson. On the electro-dynamic qualities of metals: effects of magnetisation on the electric conductivity of nickel and iron. *Proc. Roy. Soc.*, 8:546–550, 1857.

[92] N. F. Mott. The electrical conductivity of transition metals. *Proc. Roy. Soc. London*, A 153:699–726, 1936.

[93] J. Smit. Magnetoresistance of ferromagnetic metals and alloys at low temperatures. *Physica*, 17:612–627, 1951.

[94] T. R. McGuire and I. Potter. Anisotropic magnetoresistance in ferromagnetic 3d alloys. *IEEE Trans. Magn.*, 11(4):1018–1038, 1975.

[95] J. Guo and M. B. A. Jalil. Transport modelling of Py film with antidot array. *J. Appl. Phys.*, 93(10):7450–7452, 2003.

[96] M. B. A. Jalil et al. Magnetic properties of lateral "antidot" arrays. *IEEE Trans. Magn.*, 38(5):2556 – 2558, 2002.

[97] C. C. Wang et al. Magnetoresistance behavior of nanoscale antidot arrays. *Phys. Rev. B*, 72:174426.1–8, 2005.